Theoretical study of field-driven spin polarization and nonlinear Hall responses in two-dimensional systems

by

Akash Dey
(PHYS11202004001)

National Institute of Science Education and Research, Bhubaneswar

A thesis submitted to the
board of studies in Physical Sciences
in partial fulfillment of requirements
for the degree of

DOCTOR OF PHILOSOPHY

of

HOMI BHABHA NATIONAL INSTITUTE

April, 2026

Homi Bhabha National Institute[1]

Recommendations of the Viva Voce Board

As members of the Viva Voce Board, we certify that we have read the dissertation prepared by Akash Dey entitled **"Theoretical Study of Field-Driven Spin Polarization and Nonlinear Hall Responses in Two-Dimensional Systems."** and recommend that it may be accepted as fulfilling the thesis requirement for the award of Degree of Doctor of Philosophy.

S. N.	Composition	Name	Signature with date	In-Person/ Online
1.	Chairman	Dr. Pratap Kumar Sahoo	Pratap 08/06/2026	In-Person
2.	Guide/Convener	Dr. Kush Saha	KSaha 08/06/2026	In-Person
3.	Co-Guide (if any)			
4.	Examiner	Dr. Sota Kitamura	北村想太 2026 Jun 8	Online
5.	Member - 1	Dr. V Ravi Chandra	Vallemini. R. Chandra 06-06-2026	In-Person
6.	Member - 2	Dr. Ashis Kumar Nandy	Akandy 08/06/2026	In-Person
7.	Member - 3	Dr. Arijit Saha	Arijit Saha 08/06/2026	In-Person
8.	Technology Advisor (if any)			

Final approval and acceptance of this thesis is contingent upon the candidate's submission of the final copies of the thesis to HBNI.

I/We hereby certify that I/we have read this thesis prepared under my/our direction and recommend that it may be accepted as fulfilling the thesis requirement.

Date: 08/06/2026

Place: NISER

Signature
Co-guide (if any)

Signature
Guide

[1] This page is to be included only for final submission after successful completion of viva voce.

Statement by author

This dissertation has been submitted in partial fulfillment of requirements for an advanced degree at Homi Bhabha National Institute (HBNI) and is deposited in the Library to be made available to borrowers under rules of the HBNI.

Brief quotations from this dissertation are allowable without special permission, provided that accurate acknowledgement of source is made. Requests for permission for extended quotation from or reproduction of this manuscript in whole or in part may be granted by the Competent Authority of HBNI when in his or her judgment the proposed use of the material is in the interests of scholarship. In all other instances, however, permission must be obtained from the author.

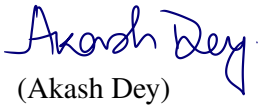

(Akash Dey)

Declaration

I, hereby declare that the investigation presented in the thesis has been carried out by me. The work is original and has not been submitted earlier as a whole or in part for a degree / diploma at this or any other Institution / University.

(Akash Dey)

Certification on Academic Integrity

Undertaking by the Student:

1. I Akash Dey, HBNI Enrolment No. PHYS11202004001 hereby undertake that the Thesis, titled "***Theoretical study of field-driven spin polarization and nonlinear Hall responses in two-dimensional systems***" is prepared by me and is the original work undertaken by me.

2. I also hereby undertake that this document has been duly checked through a plagiarism detection tool and the document is found to be plagiarism free as per the guidelines of the Institute/UGC.

3. I am aware and undertake that if plagiarism is detected in my thesis at any stage in the future, suitable penalty will be imposed as applicable as per the guidelines of the Institute/UGC.

Akash Dey.
(Akash Dey)

Endorsed by the Thesis Supervisor:

I certify that the thesis written by the Researcher is plagiarism free as mentioned above by the student.

Signature of the Thesis Supervisor with date K Saha 11/06/2026

Name : Dr. Kush Saha

Designation : Reader-F

Department/ Centre : School of Physical Sciences

Name of the CI/ OCC : National Institute of Science Education and Research

Academic Contributions

Publications/Preprints Related to this thesis

- **Akash Dey**, Ashis Kumar Nandy, Kush Saha *"Current-induced spin polarisation in Rashba-Dresselhaus systems under different point groups"*, New J. Phys. **27**,013024 (2025).
- **Akash Dey** *"Nonlinear Hall responses in tunable nodal Dirac semimetals"*, arXiv:2511.20214 (under review in journal).

Other Publications/Preprints not included in the thesis

- Debasmita Swain, **Akash Dey**, Anushree Roy, Kush Saha, Sitikantha D. Das. *"Nontrivial phonon dynamics and significant electron-phonon coupling of the high-frequency modes in a Dirac semimetal"*, Phys. Rev. B **111**, 035143 (2025).
- Neelanjan Chakraborty*, **Akash Dey***, Snehasish Nandy, Sudeep Kumar Ghosh, Kush Saha. *"Probing pure spin-rotation quantum geometry in persistent spin textures via nonlinear transport"*, arXiv:2603.04023 (under review in journal).
  (* These authors contributed equally)

Conferences/Schools

- 13th International Conference on Spectroscopic of Novel Superconductors (SNS 2022) December 12 - 16, 2022; Indian Institute of Science, Bangalore, India.

- Emerging trends in Quantum Condensed Matter Physics (EQCMP-2024)

  August 21 - 23, 2024; Institute of Physics, Bhubaneswar, India.

- 1st DAE Conclave 2024

  October 22 - 26, 2024; National Institute of Science Education and Research, Bhubaneswar, India.

- Physics of Quantum Matter School (PQMS)

  May 22 - June 02, 2023; National Institute of Science Education and Research, Bhubaneswar, India.

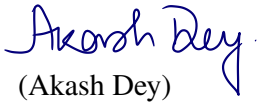

(Akash Dey)

This thesis is dedicated to my mother and sister,

Rikta Dey & Arpita Dey

For their endless love, support, and encouragement.

Acknowledgments

First and foremost, I extend my heartfelt gratitude to my PhD advisor, *Dr. Kush Saha*, for his support and guidance throughout the years. His invaluable insights and the many discussions we shared have profoundly shaped my development as a researcher. Beyond specific scientific ideas, I have gained invaluable insights from him, particularly in cultivating a clear thought process, approaching problems with depth and rigor, and developing effective scientific writing skills. He granted me the freedom to explore my own theoretical directions while consistently encouraging engagement with both theorists and experimentalists. I feel truly fortunate to have had the opportunity to work under his mentorship.

I am deeply thankful to the Council of Scientific and Industrial Research (CSIR) and the Department of Atomic Energy (DAE) for the financial support throughout my research tenure. I am also grateful to the Homi Bhabha National Institute and the National Institute of Science Education and Research for providing me with an excellent academic environment and the necessary resources to pursue my research endeavors. My heartfelt thanks go to the School of Physical Sciences for providing access to all essential facilities, which were instrumental in carrying out my studies.

I extend my sincere gratitude to the members of my doctoral committee, *Dr. Pratap Kumar Sahoo* (Chairman), *Dr. Kush Saha*, *Dr. V Ravi Chandra*, *Dr. Ashis Kumar Nandy*. *Dr. Arijit Saha* (External member, IOP Bhubaneswar). Their critical evaluations, insightful feedback, and constructive suggestions during annual reviews and the pre-synopsis significantly enriched the depth and quality of my research.

I would like to express my sincere appreciation to my collaborators *Dr. Ashis Kumar Nandy*, *Dr. Debasmita Swain*, *Dr. Sitikantha D. Das*, *Dr. Anushree Roy*, *Neelanjan Chakraborti*, *Dr.*

Snehasish Nandy, and *Dr. Sudeep Kumar Ghosh* for their invaluable contributions to my research. Their insightful discussion and constructive critique during the preparation of my manuscripts have played a great role in refining the quality of my work.

I extend my heartfelt gratitude to my seniors and postdoctoral researchers, *Dr. Arghya Mukherjee*, *Dr. Manasa Kalla*, and *Dr. Kallol Mondal* for their sincere support.

I am equally thankful to my group members, *Dr. Debamalya Dutta*, *Rahul Ghosh*, and *Ivan Dutta*, for their support and insightful discussions. I would also like to express my sincere appreciation to my colleagues and friends at RL-409 (PhD) — *Radha Madhab Chandra*, *Indrajit Paul*, *Sachin Kala*, *Sadaf Madni*, and *Dr. Anirban Dinda*, whose presence brought warmth and liveliness to the lab.

Furthermore, I am deeply grateful to all my seniors, friends, and juniors, both within and outside the department, for their support and companionship. Especially like to acknowledge *Dr. Charanpreet Singh*, *Dr. Sujit Garain*, *Dr. Tanim Firdoshi*, *Dr. Anupa Kumari*, *Dr. Prafulla Saha*, *Dr. Sourav Dey*, *Dr. Subhadip Pradhan*, *Dr. Prottay Das*, *Soham Banerjee*, *Sagnik Mishra*, *Manas Debnath*, *Md Tousif Alam*, *Sayan Banik*, *Amit Pal*, *Atanu Jana*, *Dr. Ankit Kumar Panda*, *Soumik Nandi*, *Md Habib Ahsan*, *Tanaya Haldar*, *Sankha Sathpati*, *Sudipta Das*, *Swati Saha*, *Ritwika Majumdar*, *Chinmoy Samanta*, *Arjun R*, *Biswajit*, *Arindam Mandal*, *Satyajyoti Achar*, and *Debajyoti Das* for their encouragement at various stages of my PhD.

My sincere thanks to my hostel mates, *Dr. Chandan Mahish*, *Dr. Ankit Abhinav*, and *Debashish Chakraborty*, for their companionship, and for making my time outside the lab equally memorable.

Special thanks to my friend *Dr. Shuvayu Roy* for introducing me to *Jalsha Ghor*, where I had the opportunity to play music, enjoy late-night jam sessions, and perform during the Nabobarsha programme experiences that brought great joy and balance to my PhD life.

I am thankful to the Bulldozer Cricket Team, the NISER football team (NISER FC), and NISER PhD FC for providing me with the opportunity to make bonds, play, and share memorable moments with many wonderful teammates. I am especially grateful to NISER FC for giving me the chance to represent the institute at IISM. It was a pleasure sharing the field with many wonderful teammates, including *Sidhdhu*, *Vairav*, *Sanu*, *Cyka*, *Rasheek*, *Dr. Sujit Garain*, *Dr. Siddharth Sankar Dutta*, *Dr. Avrajjal Ghosh*, and *Sayan Gupta*. I am deeply thankful to these teams and their players for their

unwavering camaraderie and encouragement, which helped me remain resilient through the many highs and lows of this journey.

I am sincerely grateful to my school friends, *Sk Izaz Ahmed*, *Sudipta Pal*, *Shubham Mondal*, and *Tanmay Mondal*, for their constant support, motivation, friendship, and guidance throughout my journey. I am also deeply grateful to all my school teachers, especially *Tapan Kumar Mandal*, *Sreepada Debnath*, *Tapas Kumar Gupta*, *Bishnu Prasad Giri*, and *Rajat Ray*, as well as my college teacher *Sanju Sir*, for their unwavering support and inspiration. They not only guided me in my academic pursuits but also played a significant role in shaping my values and character.

I would especially like to thank *Sk Izaz Ahmed*, *Sayan Gupta*, *Amit Haldar*, *Dr. Debopom Acharjee*, and *Tithi* for their unwavering support and for always standing by me through the many ups and downs of my journey.

I offer my heartfelt gratitude and pranam to my *Thakur* for his blessings and guidance throughout my life. I owe everything to my parents *Rikta Dey*, and *Asoke Dey*, whose boundless love, unwavering support, and constant encouragement have been the foundation of my journey. Their sacrifices, faith, and presence have been my greatest strength, guiding me through every step of life with courage and purpose. I am deeply grateful to my elder sister, *Arpita Dey*, and my brother-in-law, *Prasenjit Samanta*, for their endless support, care, and encouragement. Their belief in me has always given me the confidence to move forward. I also sincerely thank my other family members, including my brother *Arpan Dey* and my aunt *Ranjana Dey*, for their affection, patience, and understanding throughout this journey. I also wish to express my heartfelt love to my niece *Sreeja Samanta*, whose innocent joy and presence have been a constant source of happiness and warmth in my life.

With a heavy heart and profound love, I remember three cherished members of my family who are no longer with me but whose presence I feel in every moment — *Misti Kaka* (Late Aloke Dey), my grandfather *Banda* (Late Suresh Chandra Dey), and my grandmother *Mampi* (Late Namita Dey). Their love, blessings, and memories continue to guide and inspire me, and they remain forever in my heart.

I am also deeply thankful to my neighbours and my club *Nabin Sangha*, who stood beside my family during difficult times in my absence.

I would like to express my heartfelt gratitude to all those whom I may have inadvertently missed in this acknowledgment, yet who have played a role in helping me complete this work. While I may not mention each of you by name, please know that your contributions are deeply appreciated.

This thesis is not only a reflection of my academic journey but also a testament to the love, support, and encouragement I have received from all of you.

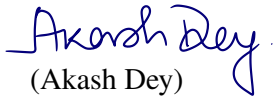

(Akash Dey)

Abstract

Low-dimensional quantum materials provide an excellent platform for studying a wide range of field-driven linear and nonlinear transport phenomena in the presence of spin-orbit coupling (SOC). Additionally, the geometric properties of electronic bands can strongly modify transport behavior in these systems and give rise to a plethora of anomalous linear and nonlinear responses. This thesis addresses various transport phenomena involving spin-orbit coupling and geometric properties of the electronic wavefunction. Specifically, we investigate electrically induced spin polarization and nonlinear Hall effects in nonmagnetic, time-reversal symmetric systems, with a particular focus on how crystal symmetry, momentum-dependent SOC, and band topology govern these transport phenomena.

In the first part, we study the current-induced spin polarization in noncentrosymmetric materials, where Rashba SOC gives rise to the Edelstein effect. We demonstrate that the nature of the induced spin polarization is strongly governed by the underlying point-group symmetries of the system, specifically C_n and C_{nv}. These symmetries restrict the allowed forms of SOC Hamiltonians, permitting both linear and higher-order (cubic-in-k) Rashba and Dresselhaus terms. We show that surfaces with C_n symmetry can host both orthogonal and non-orthogonal spin polarizations relative to an applied electric field. In contrast, systems with C_{nv} symmetry exhibit exclusively transverse spin polarization, independent of higher-order SOC contributions. Furthermore, we uncover qualitatively distinct energy-dependent spin-polarization behavior arising from cubic-in-k SOC compared to linear SOC, which can be tuned, for example, via chemical doping.

Interestingly, the Rashba–Dresselhaus system under C_n symmetry exhibits a symmetry-protected persistent spin texture (PST) at equal SOC strengths, resulting in the suppression of field-induced

spin polarization. In the second part, we therefore study the non-linear Hall response in this system. Exactly at the PST point, we find that both the linear and nonlinear Hall responses vanish. However, a small deviation from the PST regime leads to a pronounced enhancement of the nonlinear Hall response. This behavior originates from the evolution of the electronic structure, which develops a nearly degenerate band structure with a single node for the near PST point and strongly modifies geometric quantities such as the Berry curvature, Berry curvature dipole, and Berry connection polarizability. This interplay between nodal band geometry and the nonlinear Hall response extends beyond Rashba–Dresselhaus systems to a broader class of materials with tunable band crossings.

In the last part, we explore nonlinear Hall transport in tunable two-dimensional Dirac semimetals that preserve time-reversal symmetry and can host single-node, double-node, or nodal-ring band structures depending on model parameters. We analyze second and third-order Hall responses driven by the quantum geometry of the electronic wavefunction. The second-order Hall effect, governed by the Berry curvature dipole, is found to be strongly enhanced in the inversion symmetry broken single-node phase, while it vanishes in the nodal-ring phase where inversion symmetry is retained. In contrast, the third-order Hall response, arising from the Berry connection polarizability, is maximized in the nodal-ring phase, particularly when the Fermi energy is tuned close to the band edge. This contrasting behavior is attributed to the distinct momentum-space distributions of the underlying quantum-geometric quantities.

In summary, this thesis establishes crystal symmetry and band topology as central principles for understanding and controlling electrically driven spin polarization and higher-order transport phenomena in low-dimensional quantum materials, offering new routes for designing spintronic and nonlinear electronic properties.

Contents

List of Figures

List of acronyms

SOC	spin-orbit coupling
2DEG	two-dimensional electron gas
RSOC	Rashba spin-orbit coupling
DSOC	Dresselhaus spin–orbit coupling
REE	Rashba Edelstein effect
SIA	structure-inversion asymmetry
BIA	bulk-inversion asymmetry
PST	persistent spin texture
ST	spin texture
FC	Fermi contour
GMR	giant magnetoresistance
TRS	time-reversal symmetry
IS	inversion symmetry
BC	Berry curvature
BCD	Berry curvature dipole
BCP	Berry connection polarizability
BCQ	Berry curvature quadrupole
AHE	anomalous Hall effect

QAHE	quantum anomalous Hall effect
SOH	second-order Hall
TOH	third-order Hall
DSM	Dirac semimetal
NRSM	nodal-ring semimetal
WSM	Weyl semimetal
SN	single node
DN	double node
NR	nodal ring
BCQ	Berry curvature quadrupole
QMD	quantum metric dipole
QMQ	quantum metric quadrupole

Chapter 1

Introduction

Low-dimensional quantum materials exhibit rich physical properties, such as Edelstein effect, nonlinear Hall effect, spin Hall effect, Kondo effect, magnetoresistance, photogalvanic effect and many more. These properties continue to shape both fundamental research and technological innovation. Many of these properties emerge from subtle features of electronic structure, symmetry, and reduced dimensionality. Their understanding has become increasingly important for the development of modern electronic, magnetic, and spin-based technologies. Probing such properties requires experimental and theoretical tools. Techniques such as spectroscopic techniques, scanning probe methods, optical measurements, and transport studies provide sensitive means to capture how a system responds to external perturbations. Among these techniques, transport measurements constitute one of the most powerful probes, as they directly connect microscopic properties of a material to experimentally observable quantities and offer deep insight into their underlying physical mechanisms [3–5]. Transport phenomena describe how charge, spin, heat, and energy flow through a material when it is driven out of equilibrium by external fields or temperature gradients. Charge transport describes how electrical carriers move through a material and reflects the underlying electronic band structure, scattering processes, and crystal symmetry, which collectively determine transport properties such as electrical conductivity [6, 7], anomalous Hall conductivity [8, 9], and thermoelectric coefficients (e.g., the Seebeck and Nernst effects) [10–12]. Spin transport describes the flow of spin angular momentum in a material and is influenced by the interplay between crystal symmetry and spin–orbit

interaction, which together lead to spin-dependent transport phenomena such as the spin Hall effect and current-induced spin polarization under nonequilibrium conditions [13, 14]. Heat and energy transport offer complementary insight, especially in systems where electronic, phononic, and magnetic degrees of freedom are strongly coupled, leading to phenomena such as the magnon Hall effect, phonon Hall effect, and spin Seebeck effect.

Among these different transport channels, spin transport continues to emerge as a particularly important direction, both from a fundamental perspective and for technological applications. Modern electronic devices based on semiconductors primarily operate by controlling the flow of electric charge. While this approach has enabled remarkable technological progress, further improvements in device speed and efficiency are increasingly limited by power consumption and signal processing constraints. These challenges have motivated the search for alternative ways to process information. A potential direction is to utilize the intrinsic spin of electrons, in addition to their charge, giving rise to the field known as spintronics [15, 16]. Spintronic devices make use of spin-polarized currents in metals and semiconductors, offering new opportunities for faster and more energy-efficient devices beyond conventional charge-based electronics. An important development in spintronics is the giant magnetoresistance (GMR) effect, discovered by Albert Fert and Peter Grünberg in 1988 [17, 18]. This is widely regarded as the foundation of spin-based electronic technologies and was recognized with the Nobel Prize in Physics in 2007. The GMR effect arises in layered systems consisting of alternating ferromagnetic and nonmagnetic materials, where the electrical resistance changes significantly depending on how the magnetizations of neighboring magnetic layers are aligned. When the magnetization is aligned parallel, electrons experience less scattering, thereby reducing the resistance. In contrast, an antiparallel alignment leads to enhanced spin-dependent scattering, resulting in a significant increase in resistance. This strong dependence of resistance on spin configuration enables efficient detection and manipulation of spin states, forming the basis for modern magnetic sensors and high-density data storage technologies like hard disk drives [19].

In spintronics, the main goal is to utilize spin and spin-polarized currents alongside conventional charge currents. This requires efficient methods for generating and controlling spin polarization and spin currents. Ferromagnetic materials naturally produce spin-polarized currents due to the

exchange interaction, which induces a preferred alignment of electron spins. However, transferring these spin-polarized carriers from ferromagnets into nonmagnetic semiconductors is often inefficient and experimentally challenging [20, 21]. As a result, considerable effort has been directed toward generating spin polarization and spin currents directly in nonmagnetic materials, offering a more practical route for integrating spintronic concepts into semiconductor-based technologies.

A prominent mechanism for generating spin polarization in nonmagnetic materials is the Edelstein effect, independently proposed by Aronov and Lyanda-Geller [22] in 1989 and by Edelstein [23] in 1990. This phenomenon originates from spin-orbit coupling (SOC) in systems with broken inversion symmetry and enables the conversion of charge currents into spin polarization. As shown schematically in Fig. 1.1, applying a current can induce a finite spin accumulation at the surface of a nonmagnetic material in the presence of strong SOC. In the commonly studied two-dimensional Rashba model, the induced spin polarization remains in-plane and is oriented transverse to the direction of the applied electric field. The electrically generated spin accumulation can exert a spin–orbit torque on a neighboring ferromagnetic layer, potentially leading to domain-wall motion or magnetization switching [24, 25]. These features have made the Edelstein effect a promising approach for electrically controlling magnetization in spintronic devices.

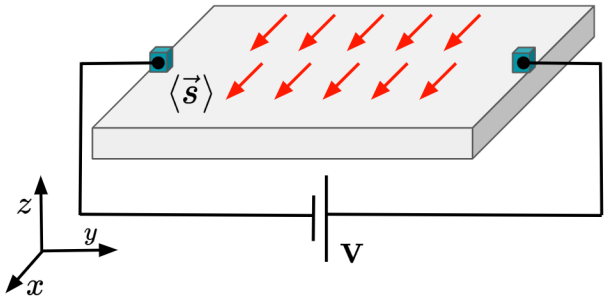

Figure 1.1: Schematic diagram of the Edelstein effect at a surface in a spin-orbit coupled nonmagnetic system. Here $\langle \vec{S} \rangle$ presents the finite spin magnetisation.

In addition to spin transport, charge transport also exhibits rich nonequilibrium phenomena that extend beyond the conventional linear response regime. In particular, recent studies have revealed that quantum geometric properties of electronic bands can give rise to novel nonlinear Hall effects, establishing an important emerging direction in condensed matter physics, which we discuss briefly in the following.

To understand the origin and significance of these nonlinear responses, it is useful to first recall

the conventional Hall effect, a fundamental charge transport phenomenon discovered by Edwin Hall in 1879 [26]. When an electric current flows through a conductor in the presence of an external magnetic field, the Lorentz force deflects charge carriers, leading to a transverse voltage perpendicular to both the current and the magnetic field. Beyond its fundamental importance, the Hall effect has found widespread applications in modern electronics, such as in magnetic field sensing and current detection [27, 28].

Subsequent studies revealed that ferromagnetic materials can exhibit a transverse voltage even without applying an external magnetic field [29]. This phenomenon is known as the anomalous Hall effect (AHE). Unlike the ordinary Hall effect, the AHE could not be explained within the classical Lorentz force framework and lacked a comprehensive theoretical understanding for several decades. A key reason is that the AHE is connected to geometric and topological concepts, which were developed and understood in more recent years. The first microscopic explanation of the AHE was proposed by Karplus and Luttinger in 1954 [30]. They demonstrated that the application of an external electric field to a ferromagnetic system leads to an extra contribution to the electron group velocity, known as the anomalous velocity. This anomalous velocity is a geometric effect arising from the Berry curvature of Bloch states. This geometric interpretation became clear in 1984 when Michael Berry introduced the concept of the Berry phase [31]. In crystalline solids, quantum states acquire an extra phase that depends on the geometry of their path in momentum space. The corresponding geometric quantity, the Berry curvature, acts as an effective magnetic field in momentum space and modifies the semiclassical motion of electrons, giving rise to an anomalous velocity [8, 32].

In addition to the intrinsic Berry curvature contribution, the AHE can also arise from extrinsic skew scattering and side-jump mechanisms in disordered systems [8].

In insulating systems, extrinsic scattering mechanisms are suppressed, and the Hall response is determined entirely by the Berry curvature of the occupied bands. In such cases, the Hall conductance becomes quantized and is characterized by an integer topological invariant known as the Chern number [33]. This quantized Hall response is referred to as the quantum anomalous Hall effect (QAHE) [34]. In a QAH state, the bulk of the material is insulating, while dissipationless

chiral edge states carry the Hall current. This effect was first realized experimentally in topological insulators [35] and has more recently been observed in 2D ferromagnets and moiré materials [36–38].

The transverse Hall current discussed above appears at linear order in the applied fields and requires breaking of the time-reversal symmetry (TRS), either through an external magnetic field or intrinsic magnetization. However, it is possible to generate a transverse nonlinear Hall response even in the presence of TRS. The corresponding schematic diagram is shown in Fig. 1.2. In 2015, Sodemann and Fu showed that a transverse Hall current can emerge at second order in the applied electric field even in systems that preserve TRS, provided inversion symmetry (IS) is broken [39]. They explained that this nonlinear Hall effect arises from the first-order moment of the Berry curvature in momentum space, called the Berry curvature dipole (BCD). In subsequent years, this effect was observed experimentally in layered transition metal dichalcogenides such as bilayer WTe_2 [40] and WSe_2 [41], confirming the role of the BCD in generating the nonlinear Hall response. It can also serve as a useful probe of valley-Chern type topological phase transitions [42, 43].

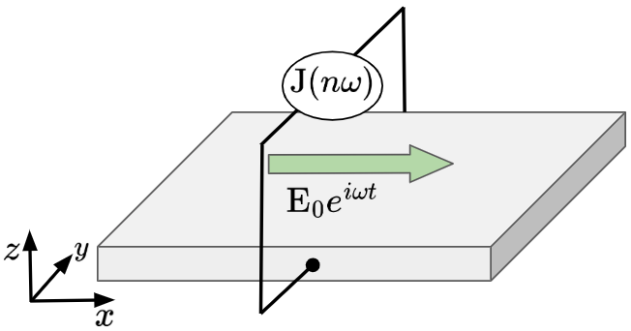

Figure 1.2: Schematic diagram of the nonlinear Hall effect in a time-reversal symmetric system. A time-dependent electric field $E_0 e^{i\omega t}$ is applied along the sample with frequency ω. This drives a nonlinear transverse Hall current $J(n\omega)$, where the integer n represents the order of the response to the electric field.

However, in systems where both TRS and IS are present, the Berry curvature vanishes in the Brillouin zone because the combined symmetries force it to cancel exactly. As a result, both the linear AHE and the BCD induced second-order Hall effect are absent. Interestingly, it has been demonstrated by H. Liu *et al.* that a higher-order transverse response can arise even in such symmetric systems [44]. In particular, a third-order Hall effect can arise from another geometric quantity called the Berry connection polarizability (BCP). This quantity originates from the electric field-induced first-order correction of the Berry connection. Although the Berry connection itself is gauge dependent, the derivative of its first-order correction with respect to the electric field,

referred to as the BCP is gauge invariant. In analogy with electric polarizability in classical electrodynamics, the BCP describes how Bloch electrons experience a field-induced positional shift in momentum space [45]. In recent times, the third-order Hall effect has been theoretically studied in two-dimensional Dirac models [44] and the hexagonally warped surface states of topological insulators [46, 47] and has been experimentally observed in the Weyl semimetal $TaIrTe_4$ [48] and bulk T_d-$MoTe_2$ [49].

In light of the above developments, it is essential to develop a unified understanding of how symmetry, spin–orbit coupling, and the quantum geometric properties of electronic bands collectively govern nonequilibrium transport phenomena in realistic systems. While linear SOC has been extensively studied in the context of current-induced spin polarization, such as the Edelstein effect, the role of more general symmetry-allowed SOC terms, particularly those involving higher-order momentum dependence, remains comparatively unexplored. Such terms can modify the current-induced spin polarisation in nontrivial ways, leading to qualitatively distinct behavior that is strongly dependent on the underlying symmetries of the system, making their systematic understanding an emerging challenge in the field of spintronics.

At the same time, modifications of the band structure induced by SOC are not merely quantitative, but can also reshape the underlying geometric properties of Bloch states in momentum space, thereby influencing the corresponding nonlinear responses.

Motivated by these considerations, the first part of this thesis investigates how linear and cubic momentum-dependent SOC terms affect current-induced spin polarization. We identify a special symmetry-protected regime in Rashba–Dresselhaus systems, known as the persistent spin texture (PST) [50], where both field-induced spin polarization and charge transport, including Hall responses, are strongly suppressed. Interestingly, small deviations from this regime give rise to a qualitatively different response, with a strong enhancement of nonlinear Hall effects. This behavior is associated with the evolution of the electronic structure, which develops a characteristic nodal band geometry near the PST point and consequently modifies the geometric properties of Bloch electrons, such as the Berry curvature, BCD, and BCP. Importantly, this connection between nodal band geometry and nonlinear Hall response is not limited to Rashba–Dresselhaus systems, but ex-

tends more broadly to other classes of systems exhibiting tunable band crossings. In this context, the final part of this thesis investigates nonlinear Hall effects in a nodal Dirac semimetal, where tuning the parameters of the underlying Hamiltonian enables a systematic realization and control of different nodal band structures. This provides a unified perspective on how tunable nodal features govern quantum geometric quantities and, consequently, the resulting nonlinear Hall responses across different physical platforms.

1.1 Outline of the thesis

We have organized this thesis into two parts: the first part of the thesis (chapter 2 to 3) is focused on current-induced spin polarization in SOC systems, while the second part (chapter 4 to 6) is devoted to nonlinear Hall effects in SOC and tunable nodal Dirac systems.

In chapter 2, we present the theoretical framework for spin–orbit–driven phenomena by introducing electron dynamics in electromagnetic fields, deriving spin–orbit coupling, and discussing the spin–orbit field that determines spin textures. We further introduce the two-dimensional electron gas as a prototypical system and discuss Rashba and Dresselhaus spin–orbit interactions. Finally, the mechanism of generating current-induced spin polarization is described within the framework of linear response theory.

Building on this foundation, chapter 3 investigates current-induced spin polarization in Rashba-Dresselhaus systems, including both linear and higher-order SOC terms, and demonstrates how crystal symmetry influences the nature of the induced spin response, including its direction and magnitude.

While the first part of the thesis focuses on spin responses induced by electric fields in time-reversal symmetric systems, such systems can also exhibit nonlinear Hall effects that originate from the quantum geometry of their electronic bands. In chapter 4, a theoretical framework for understanding these effects is developed through the introduction of the key quantum geometric quantities involved.

Based on this framework, chapter 5 investigates nonlinear Hall effects in Rashba–Dresselhaus

systems, emphasizing the PST regime. In the vicinity of PST, the electronic structure develops characteristic nodal features, which play a crucial role in enhancing nonlinear Hall responses. To further elucidate the role of nodal band geometry, chapter 6 examines nonlinear Hall responses in a tunable nodal Dirac semimetal with distinct nodal phases, demonstrating how different nodal band structures influence the underlying quantum geometric quantities and lead to distinct higher-order Hall responses.

Finally, in chapter 7, we summarize the main findings of the thesis and discuss their broader implications.

Chapter 2

Theoretical framework for spin–orbit driven phenomena

In solids, spin-orbit coupling (SOC) plays a central role in shaping the electronic band structure and gives rise to a variety of spin-dependent phenomena. Arising from relativistic corrections, SOC links the electron's spin to its orbital motion and constitutes the fundamental mechanism behind the Edelstein effect. Furthermore, SOC is essential for phenomena such as the spin Hall effect [51, 52], where a longitudinal charge current generates a transverse spin current due to spin-dependent deflection of carriers. Motivated by these considerations, we now develop the theoretical framework for understanding spin–orbit–driven spin polarization in the following sections. We begin by describing the dynamics of electrons in external electromagnetic fields, which establishes how electric and magnetic fields couple to electronic motion through minimal coupling. With this understanding, we derive spin–orbit coupling as a relativistic correction to electron dynamics and show how it can be incorporated into an effective nonrelativistic Hamiltonian. Next, we introduce the concept of the spin–orbit field, which provides an intuitive description of how spin–orbit coupling lifts spin degeneracy and generates momentum-dependent spin textures in solids.

To illustrate these concepts, we focus on the two-dimensional electron gas as a simple and widely used platform, and examine the Rashba and Dresselhaus mechanisms of spin splitting that arise from different types of inversion asymmetry. Subsequently, we discuss the physical mechanism of how

an external electric field can generate a finite spin polarization in these systems. Finally, we present the Kubo linear response formalism, which provides a microscopic and quantitative framework for calculating the electrically induced spin polarization discussed in this thesis.

2.1 Dynamics of electrons in external electromagnetic fields

External electromagnetic fields affect the motion of electrons through the Lorentz force. For an electron with charge $-e$, the equation of motion is

$$m\ddot{\mathbf{r}} = -e\Big[\mathbf{E}(\mathbf{r},t) + \dot{\mathbf{r}} \times \mathbf{B}(\mathbf{r},t)\Big], \tag{2.1}$$

where m is the electron mass, $\mathbf{r}$ denotes the electron position vector; $\mathbf{E}(\mathbf{r},t)$ and $\mathbf{B}(\mathbf{r},t)$ represent the electric and magnetic fields, respectively. The electric and magnetic fields are related by Maxwell's equations and can be conveniently expressed in terms of scalar ($\Phi(\mathbf{r},t)$) and vector ($\mathbf{A}(\mathbf{r},t)$) potentials. In particular, Gauss's law for magnetism, $\nabla \cdot \mathbf{B} = 0$, ensures that the magnetic field can be written as $\mathbf{B} = \nabla \times \mathbf{A}(\mathbf{r},t)$. Using this relation in Faraday's law, $\nabla \times \mathbf{E} = -(\partial\mathbf{B}/\partial t)$, leads to $\nabla \times \left(\mathbf{E} + \frac{\partial \mathbf{A}}{\partial t}\right) = 0$, which implies that the quantity in brackets is a gradient field. Introducing the scalar potential $\Phi(\mathbf{r},t)$, the electric field become

$$\mathbf{E} = -\nabla_r \Phi(\mathbf{r},t) - \frac{\partial \mathbf{A}(\mathbf{r},t)}{\partial t}. \tag{2.2}$$

To describe electron dynamics, we construct a Lagrangian whose Euler-Lagrange equations reproduce the Lorentz force. In the absence of electromagnetic fields, the electron is described by the free-particle Lagrangian $L_0 = \frac{1}{2}m\dot{\mathbf{r}}^2$. When fields are present, the resulting Lagrangian is

$$L = \frac{1}{2}m\dot{\mathbf{r}}^2 + e\,\dot{\mathbf{r}} \cdot \mathbf{A}(\mathbf{r},t) - e\,\Phi(\mathbf{r},t). \tag{2.3}$$

Substituting this expression into the Euler-Lagrange equations,

$$\frac{d}{dt}\frac{\partial L}{\partial \dot{\mathbf{r}}} - \frac{\partial L}{\partial \mathbf{r}} = 0, \tag{2.4}$$

we can directly recover the Lorentz force, confirming that this Lagrangian correctly describes an electron in electromagnetic fields. The canonical momentum conjugate to $\mathbf{r}$ follows from the Lagrangian as

$$\mathbf{p} = \frac{\partial L}{\partial \dot{\mathbf{r}}} = m\dot{\mathbf{r}} + e\mathbf{A}(\mathbf{r}, t). \tag{2.5}$$

This shows that the canonical momentum differs from the physical momentum by the vector potential. The Hamiltonian is obtained through the Legendre transformation, which yields

$$H = \frac{1}{2m}\left[\mathbf{p} - e\mathbf{A}(\mathbf{r}, t)\right]^2 + e\Phi(\mathbf{r}, t). \tag{2.6}$$

To describe the system quantum mechanically, the classical momentum and position are replaced by their operator counterparts as, $\mathbf{p} \rightarrow \hat{\mathbf{p}} = -i\hbar\nabla$, and $\mathbf{r} \rightarrow \hat{\mathbf{r}}$. The quantum dynamics is governed by the time-dependent Schrödinger equation,

$$i\hbar\frac{\partial}{\partial t}\psi(\mathbf{r}, t) = \hat{H}\,\psi(\mathbf{r}, t), \tag{2.7}$$

where $\psi(\mathbf{r}, t)$ denotes the electron wave function at position $\mathbf{r}$ and time t. The Hamiltonian operator is given by

$$\hat{H} = \frac{1}{2m}\left[\hat{\mathbf{p}} - e\mathbf{A}(\mathbf{r}, t)\right]^2 + e\Phi(\mathbf{r}, t). \tag{2.8}$$

More generally, if the field-free system is described by a Hamiltonian $\hat{H}_0(\hat{\mathbf{p}})$, coupling to external electromagnetic fields is introduced through the replacement

$$\hat{\mathbf{p}} \rightarrow \hat{\mathbf{p}} + e\mathbf{A}(\mathbf{r}, t), \tag{2.9}$$

together with the scalar potential term, leading to

$$\hat{H} = \hat{H}_0\big(\hat{\mathbf{p}} + e\mathbf{A}(\mathbf{r},t)\big) - e\Phi(\mathbf{r},t). \tag{2.10}$$

This prescription is known as the Peierls or minimal-coupling substitution [53, 54]. It reflects that electromagnetic fields modify quantum electron dynamics by shifting the canonical momentum and adding the electrostatic energy, providing the fundamental starting point for transport and response theories in condensed-matter systems.

When the system is driven solely by a spatially uniform electric field, it is convenient to choose a gauge in which the scalar potential vanishes, $\Phi(\boldsymbol{r},t) = 0$, and the electric field is incorporated entirely through a time-dependent vector potential, $\boldsymbol{A}(\boldsymbol{r},t) = -\boldsymbol{E}\,t$. In this case, the Hamiltonian remains translationally invariant and takes the form

$$\hat{H}(t) = \hat{H}_0\big(\hat{\mathbf{p}} + e\mathbf{A}(t)\big). \tag{2.11}$$

Having established the quantum description of electrons in electromagnetic fields, we now derive spin–orbit coupling as a relativistic correction in the following section.

2.2 Spin-orbit coupling

Spin–orbit coupling arises from relativistic corrections to electron dynamics and provides a microscopic link between the spin and orbital degrees of freedom. It can be incorporated into a non-relativistic Hamiltonian as an effective correction term.

In the non-relativistic regime, free electron dynamics is described by the time-dependent Schrödinger equation as described in Eq. 2.7 with $\hat{H} = \hat{\mathbf{p}}^2/2m$. However, the Schrödinger equation does not treat time and space on equal footing. It involves a first-order derivative in time and second-order derivatives in spatial coordinates, for which it is not Lorentz invariant. A relativistically consistent description is provided by the Dirac equation [55],

$$i\hbar\frac{\partial}{\partial t}\Psi(\mathbf{r},t) = \left[c\,\hat{\alpha}\cdot\hat{\mathbf{p}} + mc^2\hat{\beta}\right]\Psi(\mathbf{r},t), \tag{2.12}$$

where Ψ is a four-component spinor, c is the speed of light. $\hat{\alpha}$, and $\hat{\beta}$ are Dirac matrices, which are given by

$$\hat{\alpha}_i = \hat{\sigma}_x \otimes \hat{\sigma}_i, \qquad \hat{\beta}_i = \hat{\sigma}_z \otimes \hat{\sigma}_0. \tag{2.13}$$

Here $\hat{\sigma}_i$ are Pauli matrices with $(i = x, y, z)$ and $\hat{\sigma}_0$ is the 2×2 unity matrix. The above Dirac equation yields the relativistic energy–momentum relation $\epsilon^2 = c^2p^2 + m^2c^4$. Following the Peierls substitution in Eq. 2.10, the Dirac equation in the presence of electromagnetic fields takes the form

$$i\hbar\frac{\partial}{\partial t}\Psi(\mathbf{r},t) = \left[c\,\hat{\boldsymbol{\alpha}}\cdot(\hat{\mathbf{p}} + e\mathbf{A}) + mc^2\hat{\beta} - e\Phi\right]\Psi(\mathbf{r},t). \tag{2.14}$$

We now analyze this Dirac equation in the non-relativistic limit, assuming a time-independent electric field and vanishing magnetic field. The spinor is expressed using the ansatz

$$\Psi(\mathbf{r},t) = e^{-i\epsilon t/\hbar}\begin{pmatrix}\psi_1(\mathbf{r},t)\\ \psi_2(\mathbf{r},t)\end{pmatrix}, \tag{2.15}$$

where ψ_1 and ψ_2 are two-component spinors. Substituting this form into the Dirac equation in Eq. 2.14 yields two coupled equations,

$$\begin{aligned}(\epsilon + e\Phi - mc^2)\psi_1 &= c\,(\boldsymbol{\sigma}\cdot\hat{\mathbf{p}})\,\psi_2,\\ (\epsilon + e\Phi + mc^2)\psi_2 &= c\,(\boldsymbol{\sigma}\cdot\hat{\mathbf{p}})\,\psi_1.\end{aligned} \tag{2.16}$$

For positive-energy solutions corresponding to electrons, ψ_2 is much smaller than ψ_1. Therefore, one may approximate

$$\psi_2 \approx \frac{\boldsymbol{\sigma}\cdot\hat{\mathbf{p}}}{mc}\psi_1. \tag{2.17}$$

Substituting this expression for ψ_2 back into the first coupled equation yields an effective equation for the large component ψ_1. Expanding systematically in powers of $1/c$ and retaining terms up

to order $1/c^2$, the resulting equation can be interpreted as a Schrödinger equation with relativistic corrections

$$i\hbar\frac{\partial\psi_1}{\partial t} = \hat{H}_{\text{eff}}\,\psi_1. \tag{2.18}$$

The effective Hamiltonian becomes

$$\hat{H}_{\text{eff}} = \frac{\hat{\mathbf{p}}^2}{2m} + V - \frac{\hat{\mathbf{p}}^4}{8m^3c^2} + \frac{\hbar}{4m^2c^2}(\nabla V \times \hat{\mathbf{p}})\cdot\boldsymbol{\sigma} + \frac{\hbar^2}{8m^2c^2}\nabla^2 V, \tag{2.19}$$

where $V = -e\Phi$. The third term represents the relativistic correction to kinetic energy, the last term is the Darwin term, and the fourth term corresponds to spin–orbit coupling [56],

$$\hat{H}_{\text{SOC}} = \frac{\hbar}{4m^2c^2}(\nabla V \times \hat{\mathbf{p}})\cdot\boldsymbol{\sigma}. \tag{2.20}$$

It explicitly couples the electron spin, described by the Pauli matrices $\boldsymbol{\sigma}$, to its orbital motion through the gradient of the electric potential. For a spherically symmetric potential $V(r)$, the gradient simplifies to $\nabla V = \frac{dV}{dr}\hat{\mathbf{r}}$. Using this expression, the SOC Hamiltonian reduces to the familiar form

$$\hat{H}_{\text{SOC}} = \frac{1}{2m^2c^2r}\frac{dV}{dr}\hat{\mathbf{L}}\cdot\hat{\mathbf{S}}, \tag{2.21}$$

where $\hat{\mathbf{L}} = \mathbf{r}\times\hat{\mathbf{p}}$ is the orbital angular momentum and $\hat{\mathbf{S}} = \frac{\hbar}{2}\boldsymbol{\sigma}$ is the spin operator.

Although SOC originates from relativistic physics, it can therefore be incorporated into a non-relativistic framework through the derived effective Hamiltonian. In crystalline solids, the presence of electric field gradients arising from the lattice potential and, in particular, from broken inversion symmetry, leads to modified forms of spin–orbit interaction. Notable examples include Rashba and Dresselhaus spin–orbit couplings, which play a central role in current-induced spin polarization phenomena.

2.3 Spin-orbit field

While SOC originates from relativistic corrections to single-particle dynamics, the effects of this in crystalline solids can be understood using the concept of spin–orbit fields. This picture illustrates how SOC lifts band degeneracies and gives rise to characteristic spin textures in momentum space. Moreover, inspecting the structure of this field at an early stage already provides intuitive insight into current-induced spin polarization, even before detailed calculations are carried out, which we have discussed in detail in Sec. 3.2 of chapter 3.

Starting from the general SOC Hamiltonian derived above in Eq. 2.20, one may rewrite it in the compact form

$$\hat{H}_{\mathrm{SOC}} = \boldsymbol{B}_{\mathrm{eff}}.\boldsymbol{\sigma}, \tag{2.22}$$

where $\boldsymbol{B}_{\mathrm{eff}}$ is a momentum-dependent vector that plays the role of an effective magnetic field in spin space, commonly referred to as the *spin-orbit field*.

In the presence of SOC, the minimal description of an electronic system involves two bands, reflecting the two spin degrees of freedom represented by the Pauli matrices. In a translationally invariant crystal, electronic states are labeled by the crystal momentum $\mathbf{k}$, and the generic two-band Hamiltonian can be written in the Pauli-matrix basis as

$$\hat{H}(\boldsymbol{k}) = d_0(\boldsymbol{k}) + \boldsymbol{d}(\boldsymbol{k}).\boldsymbol{\sigma}, \tag{2.23}$$

where $d_0(\boldsymbol{k})$ describes the spin-independent dispersion and $\boldsymbol{d}(\boldsymbol{k}) = (d_x, d_y, d_z)$ contains all spin-dependent contributions. Comparing this expression with the SOC Hamiltonian introduced in Eq.2.22, $\boldsymbol{d}(\boldsymbol{k})$ can be identified as the spin-orbit field. The corresponding energy eigenvalues are

$$\varepsilon_{\pm}(\boldsymbol{k}) = d_0(\boldsymbol{k}) \pm |\boldsymbol{d}(\boldsymbol{k})|, \tag{2.24}$$

showing that SOC lifts the spin degeneracy and splits the spectrum into two branches separated by

an energy $2|\boldsymbol{d}(\boldsymbol{k})|$. The corresponding normalized eigenstates become

$$|\psi^{\pm}(\boldsymbol{k})\rangle = \sqrt{\frac{|\boldsymbol{d}(\boldsymbol{k})| \mp d_z(\boldsymbol{k})}{2|\boldsymbol{d}(\boldsymbol{k})|}} \begin{pmatrix} \pm \dfrac{(d_x(\mathbf{k}) - i d_y(\mathbf{k}))}{|\boldsymbol{d}(\boldsymbol{k})| \mp d_z(\mathbf{k})} \\ 1 \end{pmatrix}. \tag{2.25}$$

Using these expressions, the spin expectation values can be evaluated as

$$\langle \sigma(\mathbf{k}) \rangle^{\pm} = \langle \psi^{\pm} | \, \sigma \, | \psi^{\pm} \rangle = \pm \frac{\mathbf{d}(\mathbf{k})}{|\mathbf{d}(\mathbf{k})|}, \tag{2.26}$$

indicating that electron spins align parallel or antiparallel to the spin–orbit field. Consequently, the direction of $\mathbf{d}(\mathbf{k})$ defines the spin texture in momentum space, while its magnitude controls the energy splitting between the two bands. In Chapter 3, we have explicitly studied band splittings and spin textures for different SOC terms under different point group symmetries by using the spin-orbit field.

In the following sections, we apply this general framework to concrete realizations of SOC in crystalline systems. In particular, we discuss the Rashba and Dresselhaus effects, which arise from different types of inversion asymmetry and represent two fundamental mechanisms of spin splitting in solids. Both interactions are most commonly realized in quantum-well structures, where electronic motion is confined, and a two-dimensional electron gas is formed. We therefore begin by introducing the two-dimensional electron gas as a prototypical platform for studying inversion-asymmetry-driven spin splitting. This approach makes it easier to understand how the spin–orbit field depends on momentum, giving rise to spin-split bands and electrically induced spin polarization.

2.4 Two-dimensional electron gas

A two-dimensional electron gas (2DEG) is generally formed at the interface between two semiconductor materials with different band gaps [3]. For instance, we have shown for GaAs/AlGaAs heterostructure in Fig. 2.1. When such materials are brought together, their conduction bands and valence bands do not align to each other, and the Fermi energy E_F is also not same (see Fig. 2.1 (a)).

Therefore, electrons move toward the side with lower energy and accumulate near the interface.

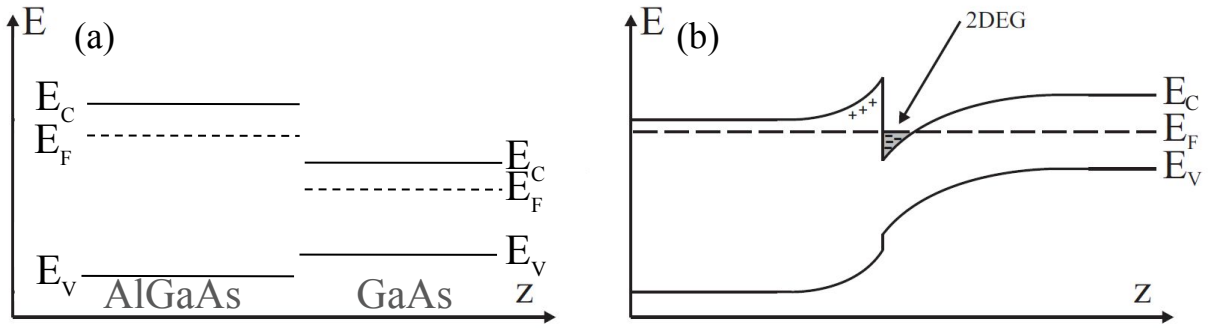

Figure 2.1: Schematic band alignment of an AlGaAs/GaAs heterojunction [1]. (a) Before contact, the conduction-band (E_C) and valence-band (E_V) edges are shown separately for AlGaAs and GaAs. (b) Band bending at an AlGaAs/GaAs interface leading to the formation of a two-dimensional electron gas.

This accumulation of electrons creates a local charge imbalance, which generates an internal electric field. As a result, the conduction band near the interface bends downward in energy. This spatial variation of the band edge produces a confining potential along the growth direction (taken as the z-axis), often referred to as band bending. The resulting potential has the form of a narrow well that traps electrons close to the interface, as shown in Fig. 2.1 (b). While electrons remain free to move parallel to the interface, their motion perpendicular to the plane is restricted by this confining potential. Because of this confinement, the allowed energies along the z-direction become discrete. In contrast, motion in the plane remains continuous. The system therefore behaves as an effectively two-dimensional electronic gas.

An important characteristic of these heterostructures is the built-in electric field perpendicular to the interface, originating from the band bending that forms the confining potential. While spin–orbit coupling is fundamentally a relativistic effect arising from electric field gradients, the breaking of inversion symmetry due to this built-in field lifts spin degeneracy and leads to momentum-dependent spin splitting. This provides the microscopic origin of the Rashba effect discussed in the following section.

2.5 Rashba effect

An important manifestation of SOC in low-dimensional systems is the Rashba effect, which arises from structural inversion asymmetry and leads to momentum-dependent spin splitting of electronic bands. This phenomenon is named after Emmanuel Rashba, who first identified it in 1959 [57], and was later formulated for two-dimensional systems by Rashba in collaboration with Yurii A. Bychkov in 1984 [58]. At a crystal surface or at the interface of heterostructures, inversion symmetry is broken because the two sides of the surface or interface are inequivalent. This structural asymmetry gives rise to an electric potential gradient along the direction normal to the surface, denoted by $\partial V/\partial \hat{\boldsymbol{n}}$, where $\hat{\boldsymbol{n}}$ is the unit vector normal to the surface. Electrons moving in this field experience an effective magnetic field in their rest frame, which gives rise to SOC. Following Eq. 2.22, this leads to the SOC Hamiltonian

$$H_{\mathrm{R}}^{\mathrm{SOC}} = \frac{\alpha_{\mathrm{R}}}{\hbar}(\hat{\mathbf{n}} \times \mathbf{k}).\boldsymbol{\sigma}, \tag{2.27}$$

known as Rashba spin–orbit coupling (RSOC). The Rashba parameter α_{R} determines the strength of SOC and depends on the electric potential gradient at the interface as follows [59]

$$\alpha_R = \frac{\hbar^2}{4m^2c^2}\int d^3r|\Phi(\hat{\boldsymbol{n}})|\frac{\partial V}{\partial \hat{\boldsymbol{n}}}, \tag{2.28}$$

where $\Phi(\hat{\boldsymbol{n}})$ is the wavefunction component varying along surface normal $\hat{\boldsymbol{n}}$. This parameter is material specific and generally ranges from 0.01 to 4 eV.Å [60, 61]. At surfaces and interfaces of materials such as Au(111) [62], Bi/Ag(111) [63], and $\mathrm{Bi_xPb_{1-x}/Ag(111)}$ [64], electronic states can be effectively described by a two-dimensional free-electron model with RSOC. The corresponding Hamiltonian for a 2DEG in the presence of RSOC is given by

$$H = \frac{\hbar^2 k^2}{2m} + \alpha_{\mathrm{R}}(k_x\sigma_y - k_y\sigma_x). \tag{2.29}$$

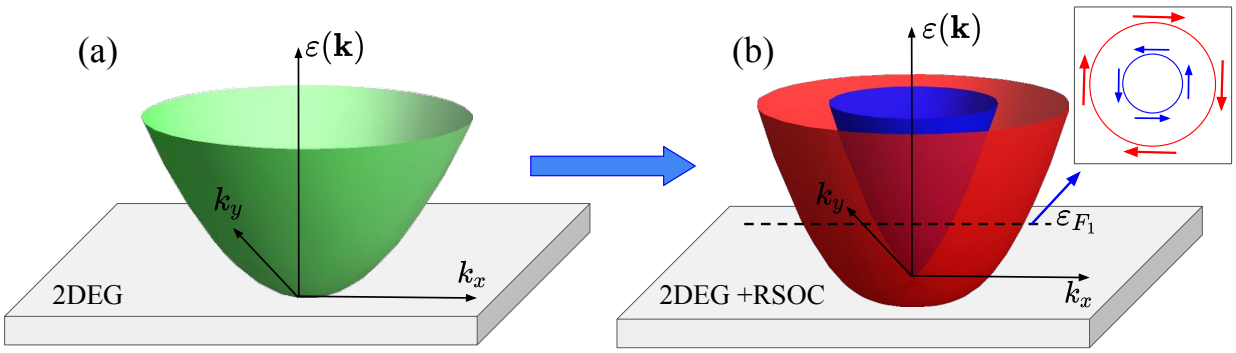

Figure 2.2: Schematic illustration of band splitting in a 2DEG in the presence of Rashba spin–orbit coupling. (a) Parabolic band dispersion of a 2DEG without RSOC. (b) Band splitting induced by RSOC, resulting in two spin-split bands. The inset shows the corresponding Fermi contours at a constant energy ε_{F_1}, along with the associated spin textures (arrows). Blue (red) denotes the inner (outer) band.

Here we consider the surface normal $\hat{\boldsymbol{n}}$ is along the z direction. The corresponding energy dispersion becomes

$$\varepsilon(\mathbf{k}) = \frac{\hbar^2 k^2}{2m} \pm \alpha_{\mathrm{R}} |\mathbf{k}|. \tag{2.30}$$

Figures 2.2 (a) and (b) illustrate the band structure of a 2DEG in the absence and presence of RSOC, respectively. In the absence of RSOC, the electronic bands are spin-degenerate, whereas its inclusion lifts this degeneracy, resulting in two spin-split branches, as shown in Fig. 2.2 (b). The resulting energy splitting depends linearly on the Rashba parameter and is given by $E_R = 2\alpha_{\mathrm{R}}|\mathbf{k}|$. In addition to band splitting, the electron spins form two oppositely oriented textures, as illustrated in the inset of Fig. 2.2 (b). In a Rashba system, electrons experience an effective spin–orbit field

$$\boldsymbol{B}_{\mathrm{eff}} = \alpha_R(-k_y, k_x), \tag{2.31}$$

which constrains the spin to align perpendicular to the electron momentum. Consequently, the spin direction becomes locked to the particle's motion, giving rise to a characteristic helical spin texture in momentum space. This phenomenon is known as *spin–momentum locking* and has been discussed explicity for different SOC terms in chapter 3.

Although Rashba spin–orbit coupling is often attributed to the electric field associated with structural inversion asymmetry, the large Rashba splitting observed in realistic materials primarily

originates from atomic spin–orbit coupling near the nuclei. Inversion symmetry breaking modifies the orbital character of Bloch states and generates a momentum-dependent orbital angular momentum through orbital hybridization. The atomic spin–orbit interaction couples this orbital angular momentum to the electron spin, leading to the Rashba spin splitting [65]. Therefore, the Rashba coupling strength depends on the interplay between atomic spin–orbit coupling, orbital hybridization, and inversion asymmetry.

2.6 Dresselhaus effect

Another important manifestation of SOC in low-dimensional systems is the Dresselhaus effect, first proposed by G. Dresselhaus [66]. In contrast to the Rashba effect, the Dresselhaus effect arises from bulk-inversion asymmetry (BIA) inherent to certain crystal lattices, most notably zinc-blende semiconductors such as GaAs and InAs. In these materials, the lack of inversion symmetry in the bulk crystal potential gives rise to an effective momentum-dependent magnetic field or the spin-orbit field that couples to the electron spin.Microscopically, Dresselhaus spin splitting originates from the combined effect of atomic spin–orbit coupling and bulk inversion asymmetry. Within multiband $k \cdot p$ theory, interband coupling between the s-like conduction band and p-like valence bands, together with remote-band contributions, generates an effective momentum-dependent spin splitting of the conduction-band states. Consequently, the Dresselhaus coupling strength is governed by band-structure parameters such as the band gap, spin–orbit splitting, and interband coupling strengths [67]. For three-dimensional bulk systems, this interaction leads to a Dresselhaus spin–orbit coupling (DSOC) Hamiltonian that is cubic in momentum and can be written as

$$H_{\mathrm{D}}^{\mathrm{SOC}} = \gamma_{\mathrm{D}} \left[k_x (k_y^2 - k_z^2)\sigma_x + k_y (k_z^2 - k_x^2)\sigma_y + k_z (k_x^2 - k_y^2)\sigma_z \right], \tag{2.32}$$

where γ_{D} denotes the bulk Dresselhaus coupling parameter. This parameter is also material-specific, and for GaAs, it generally ranges from 6.5 to 30 eV.Å [68]. When a two-dimensional electronic system is formed at a surface or interface, the bulk Dresselhaus interaction is effectively projected onto

the corresponding confinement plane. This dimensional reduction suppresses the cubic momentum terms and yields a dominant linear contribution whose explicit form depends on the crystallographic orientation of the surface (such as [001], [110], or [111]) [67]. For a 2DEG confined along the z direction, corresponding to a [001] growth axis, the effective DSOC Hamiltonian reduces to

$$H^{\mathrm{SOC}}_{\mathrm{D}(-)} = \beta(k_x\sigma_x - k_y\sigma_y), \tag{2.33}$$

where β represents the effective linear Dresselhaus coupling strength. We referred to this term as $H_{\mathrm{D}(-)}$ (DSOC(-)) beacuse depending on the choice of in-plane coordinate axes, this linear Dresselhaus Hamiltonian may also be written in another equivalent form,

$$H^{\mathrm{SOC}}_{\mathrm{D}(+)} = \beta(k_x\sigma_x + k_y\sigma_y), \tag{2.34}$$

which can be obtained from the standard [001] expression through a rotation of the coordinate system and denoted as $H_{\mathrm{D}(+)}$ (DSOC(+)). Both terms arise from the same BIA and lead to an identical

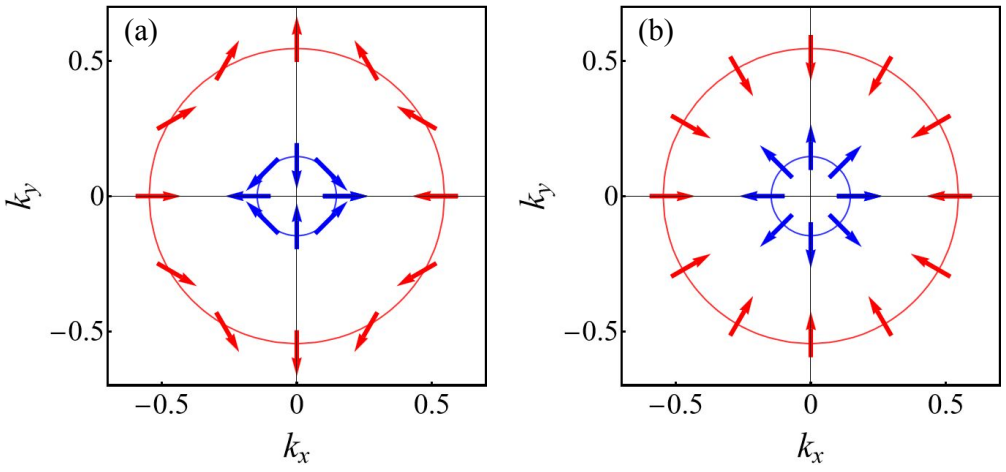

Figure 2.3: Spin textures of a 2DEG with Dresselhaus spin–orbit coupling: (a) and (b) correspond to the two forms of Dresselhaus coupling, DSOC(−) and DSOC(+), respectively. The arrows denote the spin orientation, revealing contrasting spin arrangements in the two cases, while the inner (blue) and outer (red) contours represent the spin-split bands.

energy dispersion in a 2DEG,

$$\varepsilon_{\pm}(\mathbf{k}) = \frac{\hbar^2 k^2}{2m} \pm \beta|\mathbf{k}|, \tag{2.35}$$

demonstrating that both Hamiltonians lead to the same band splitting structure with an energy separation $E_D = 2\beta|\mathbf{k}|$. However, the corresponding effective spin–orbit fields differ. For the conventional Dresselhaus (DSOC(-)) Hamiltonian,

$$\boldsymbol{B}_{\text{eff}}^{(-)} = \beta(k_x, -k_y), \tag{2.36}$$

whereas for the rotated form (DSOC(+)), the effective field becomes

$$\boldsymbol{B}_{\text{eff}}^{(+)} = \beta(k_x, k_y). \tag{2.37}$$

As a consequence, (DSOC(-)) and (DSOC(+)) Hamiltonians produce different spin textures and spin–momentum locking patterns in momentum space, as we have shown in Fig. 2.3 (a) and (b), respectively. In the first case, the spin orientation changes sign between the k_x and k_y directions, while in the second case, the spins align parallel or antiparallel to the in-plane momentum.

At surfaces and interfaces, Rashba and Dresselhaus SOC often coexist. Their interplay gives rise to complex spin textures and strongly influences current-induced spin polarization, as discussed in Sec. 3.3.1 of Chapter 3. This interaction also affects spin relaxation and can lead to the emergence of a PST, which we have analysed in detail in Sec. 5.2 of chapter 5.

2.7 Generation of spin polarization

In this section, we discuss how an applied electric field induces spin polarization in a 2DEG in the presence of SOC. To illustrate this mechanism, we consider a 2DEG with Rashba SOC. In equilibrium, the electronic structure consists of two spin-split bands with opposite spin orientations. For every electronic state with momentum $\mathbf{k}$, there is a corresponding time-reversed state at $-\mathbf{k}$ with the opposite spin direction, as we have already seen in Sec. 2.5. Because of this symmetry, the spin distribution in momentum space is perfectly balanced, and the total spin polarization become zero. This is illustrated in Fig. 2.4 (a), where two concentric Fermi contours appear, with spins winding in opposite directions on the inner and outer bands, leading to complete cancellation ($\langle \boldsymbol{S} \rangle = 0$).

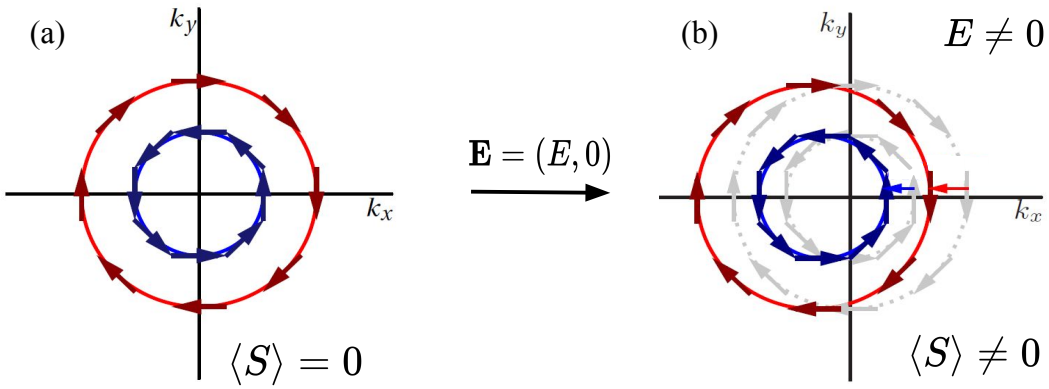

Figure 2.4: Spin distribution of a 2DEG with Rashba SOC [2]. (a) In equilibrium, the spin distribution on the two Fermi contours is balanced and oppositely oriented, leading to zero net spin polarization ($\langle \boldsymbol{S} \rangle = 0$). (b) Under an applied electric field $\mathbf{E} = (E, 0)$, the Fermi contours shift in momentum space, breaking this balance and giving rise to a finite spin polarization ($\langle \boldsymbol{S} \rangle \neq 0$).

When an external electric field $\mathbf{E}$ is applied , the system is driven out of equilibrium. The field shifts the Fermi contours in momentum space in the direction opposite to $\mathbf{E}$. However, the outer contour experiences a slightly larger shift than the inner one, because electrons in the outer band acquire a higher drift velocity. Since spins are locked to momentum in a Rashba system, this shift immediately produces an imbalance in the spin distribution. States that were previously canceled by their time-reversed partners are no longer equally occupied. Consequently, spins pointing in one direction become slightly more populated than those pointing in the other direction. This imbalance gives rise to a finite net spin polarization ($\langle \boldsymbol{S} \rangle \neq 0$), which we have shown in Fig. 2.4(b).

To place the above physical picture on a quantitative footing, a microscopic theoretical description of electric-field-induced spin polarization is required. Several approaches have been developed for this purpose, including Boltzmann transport theory [2, 69], Landau–Zener theory [70], and Kubo linear response theory [71]. In this work, we adopt the Kubo formalism to provide a comprehensive description of current-induced spin polarization. In the next section, we discuss the formulation of the Kubo formula for calculating spin polarization.

2.8 Kubo linear response theory

This theoretical approach provides a systematic framework to determine how a quantum system responds to a weak time-dependent perturbation by relating the induced change in an observable to equilibrium correlation functions of the unperturbed system. Although our primary interest is in electrically induced spin polarization, here we present the derivation in a general form for an arbitrary operator Q. We will later apply the result of this general framework to obtain the spin polarization in chapter 1.

We consider a system described by a time-dependent Hamiltonian

$$H(t) = H_0 + H'(t), \tag{2.38}$$

where H_0 is the equilibrium Hamiltonian and $H'(t)$ represents a weak external perturbation switched on at time t_0. Within linear response theory, the deviation of the expectation value of an arbitrary operator Q from its equilibrium value can be written as [72, 73]

$$\delta\langle Q(t)\rangle = \langle Q(t)\rangle - \langle Q\rangle_0 = \int_{t_0}^{\infty} dt' C^R_{QH'}(t,t'), \tag{2.39}$$

where $\langle..\rangle_0$ denotes the equilibrium thermal average taken with respect to the unperturbed Hamiltonian H_0. The retarded (R) correlation function is defined as

$$C^R_{QH'}(t,t') = C^R_{QH'}(t-t') = -i\theta(t-t')\langle[Q(t), H'(t')]\rangle_0, \tag{2.40}$$

where the Heaviside function $\theta(t-t')$ ensures causality, i.e., the system responds only after the perturbation is applied. For a time-dependent perturbation, it is convenient to work in the frequency (ω) domain. The Fourier transform of the retarded correlation function is given by

$$\delta\langle Q_\omega\rangle = C^R_{QH'}(\omega) = \int_{-\infty}^{\infty} dt\ e^{i\omega t}\ e^{-\eta t} C_{QH'}(t), \tag{2.41}$$

where η is a positive infinitesimal or the broadening parameter introduced to ensure convergence.

Here, we have applied an external electric field $\mathbf{E}(\mathbf{r}, t)$ as a perturbation, which can be written in terms of a vector ($\mathbf{A}(\mathbf{r}, t)$) and scalar ($\Phi(\mathbf{r}, t)$) potential (see Eq. 2.2). For a spatially uniform electric field, we only consider the vector potential, as discussed in Sec. 2.1 and it can be expressed in the frequency domain as

$$\begin{aligned}\mathbf{A}(\omega) &= \int_{-\infty}^{\infty} dt\ \mathbf{A}(t)\ e^{i\omega t} = \frac{1}{i\omega}\int_{-\infty}^{\infty} de^{i\omega t}\mathbf{A}(t) = -\frac{1}{i\omega}\int_{-\infty}^{\infty} d\mathbf{A}(t)e^{i\omega t} = -\frac{1}{i\omega}\int_{-\infty}^{\infty} dt\ \partial_t\mathbf{A}(t)e^{i\omega t} \\ &= \frac{\mathbf{E}(\omega)}{i\omega}.\end{aligned} \tag{2.42}$$

In the presence of this vector field, the wave vector becomes $\mathbf{k} \rightarrow \mathbf{k} - e\mathbf{A}/\hbar$ by Peierls substitution from Sec. 2.1. Therefore to the first order of the electric field, the perturbation Hamiltonian $H'(t)$ can be written as,

$$H'(t) = -e\mathbf{A}(t) \cdot v, \tag{2.43}$$

where the velocity operator v reads

$$v = \frac{1}{\hbar}\nabla_{\mathbf{k}} H_0. \tag{2.44}$$

To evaluate $\delta\langle Q\rangle$, we compute the retarded correlation function (Eq. 2.40) between the operator Q and the perturbation H'. Direct evaluation of the real-time correlation function at finite temperature is technically complicated. Therefore, it is convenient to first calculate the corresponding correlation function in imaginary time using the Matsubara Green's function formalism, and then obtain the physical response by analytic continuation.

We define the Matsubara correlation function as [Eq. (11.20) in the Ref. [72]]

$$C_{QH'}(\tau - \tau') = -\left\langle T_\tau\left[Q(\tau)H'(\tau')\right]\right\rangle, \tag{2.45}$$

where T_τ is the imaginary-time ordering operator. This formulation is particularly useful because thermal expectation values can be evaluated systematically using Green's function techniques.

To evaluate the Matsubara correlation function explicitly, we express the operators in second-quantized form. For a translationally invariant system, an arbitrary one-body operator can be written

as

$$Q = \sum_{\mathbf{k},\alpha,\beta} c^{\dagger}_{\mathbf{k}\alpha} Q_{\alpha\beta} c_{\mathbf{k}\beta},$$
$$H' = \sum_{\mathbf{k},\alpha,\beta} c^{\dagger}_{\mathbf{k}\alpha} H'_{\alpha\beta} c_{\mathbf{k}\beta}, \tag{2.46}$$

where $c^{\dagger}_{\mathbf{k}\alpha}$ and $c_{\mathbf{k}\alpha}$ are fermionic creation and annihilation operators, and α, β label internal degrees of freedom such as spin, orbital, etc. Substituting these expressions into the imaginary-time correlation function in Eq. 2.45 leads to a thermal expectation value involving four fermionic operators. Using Wick's theorem, this four-operator term can be decomposed into products of two Green's functions. Keeping only the lowest-order contribution shown in Fig. 2.5, we obtain

$$C_{QH'}(\tau - \tau') = \sum_{\mathbf{k}} \sum_{\alpha\beta\gamma\delta} Q_{\alpha\beta}(\tau) G_{\mathbf{k},\beta\gamma}(\tau - \tau') H'_{\gamma\delta}(\tau') G_{\mathbf{k},\delta\alpha}(\tau' - \tau), \tag{2.47}$$

where

$$G_{\mathbf{k},\alpha\beta}(\tau - \tau') = -\left\langle T_\tau c_{\mathbf{k}\alpha}(\tau) c^{\dagger}_{\mathbf{k}\beta}(\tau') \right\rangle \tag{2.48}$$

is the Matsubara Green's function. The above expression can be written compactly using matrix notation as

$$C_{QH'}(\tau - \tau') = \sum_{\mathbf{k}} \mathrm{Tr}\left[Q(\tau) G_{\mathbf{k}}(\tau - \tau') H'(\tau') G_{\mathbf{k}}(\tau' - \tau) \right], \tag{2.49}$$

where the trace is taken over the internal indices. Because the correlation function depends only on the time difference $\theta = \tau - \tau'$, therefore, we introduce the Fourier transformation as

$$C_{QH'}(i\omega_m) = \int_0^{\beta} d\theta \, e^{i\omega_m \theta} C_{QH'}(\theta), \tag{2.50}$$

where $\omega_m = 2m\pi/\beta$ are the discrete frequencies compatible with the periodicity of the correlation function in imaginary time. Here $\beta = 1/K_B T$ with K_B the Boltzmann constant and T the temperature. To evaluate this Fourier transformation, the Green's functions appearing in $C_{QH'}(\theta)$ must also be expressed in frequency space. The single-particle Green's function satisfies the antiperiodic

boundary condition $G_{\mathbf{k}}(\theta+\beta) = -G_{\mathbf{k}}(\theta)$, and therefore admits the expansion

$$G_{\mathbf{k}}(\theta) = \frac{1}{\beta}\sum_{n} e^{-i\varepsilon_n\theta} G_{\mathbf{k}}(i\varepsilon_n), \tag{2.51}$$

where $\varepsilon_n = (2n+1)\pi/\beta$ are the corresponding discrete frequencies. Substituting this expansion for both Green's functions in Eq. 2.49 and performing the integration over θ, we finally obtain

$$C_{QH'}(i\omega_m) = \frac{1}{\beta}\sum_{\mathbf{k},n} \mathrm{Tr}\left[QG_{\mathbf{k}}(i\varepsilon_n + i\omega_m)H'(i\omega_m)G_{\mathbf{k}}(i\varepsilon_n)\right]. \tag{2.52}$$

This correlation can be rewritten as

$$C_{QH'}(i\omega_m) = \frac{1}{\beta}\sum_{\mathbf{k},n} \mathrm{Tr}\left[H'(i\omega_m)G_{\mathbf{k}}(i\varepsilon_n)QG_{\mathbf{k}}(i\varepsilon_n + i\omega_m)\right]. \tag{2.53}$$

The expression inside the summation contains a product of two single-particle Green's functions, which can be evaluated using the standard contour integration method. This procedure converts the discrete Matsubara sum into an integral over real energy weighted by the Fermi distribution function $n_F(\varepsilon)$. After performing the summation and analytic continuation according to $i\omega_m \to \omega + i\eta$, the correlation function can be rewritten using retarded and advanced Green's functions defined on the real-frequency axis. We obtain from Eq. 2.53

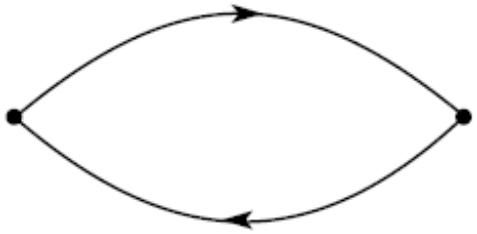

Figure 2.5: Lowest order Feynman diagram of Eq. 2.45

$$\begin{aligned} C_{QH'}(\omega+i\eta) = -\int_{-\infty}^{\infty}\frac{d\varepsilon}{2\pi i} n_F(\varepsilon)\sum_{k}\mathrm{Tr}\Big[H'(\omega+i\eta)G_k^A(\varepsilon-\hbar\omega)Q\Big(G_k^R(\varepsilon)-G_k^A(\varepsilon)\Big) \\ + H'(\omega+i\eta)\Big(G_k^R(\varepsilon)-G_k^A(\varepsilon)\Big)QG_k^R(\varepsilon+\hbar\omega)\Big]. \end{aligned} \tag{2.54}$$

If the applied electric field is along the spatial direction j, the explicit form of the perturbation from

Eq. 2.42 and 2.43 can be written as

$$H'(\omega) = -e\frac{E_j}{i\omega}v_j. \tag{2.55}$$

Using this relation, the final expression of the correlation or the $\delta\langle Q(\omega)\rangle$ reads

$$\begin{aligned}\delta\langle Q(\omega)\rangle = -\frac{eE_j}{\omega}\int_{-\infty}^{\infty}\frac{d\varepsilon}{2\pi}n_F(\varepsilon)\sum_k \mathrm{Tr}\Big[v_j G_k^A(\varepsilon-\hbar\omega)Q\Big(G_k^R(\varepsilon)-G_k^A(\varepsilon)\Big)\\ + v_j\Big(G_k^R(\varepsilon)-G_k^A(\varepsilon)\Big)QG_k^R(\varepsilon+\hbar\omega)\Big].\end{aligned} \tag{2.56}$$

Finally, the expression for the spin polarization will be as follows [71]:

$$\begin{aligned}\langle S_i(\omega)\rangle = -\frac{eE_j}{\omega}\int_{-\infty}^{\infty}\frac{d\varepsilon}{2\pi}n_F(\varepsilon)\sum_k \mathrm{Tr}\Big[v_j G_k^A(\varepsilon-\hbar\omega)S_i\Big(G_k^R(\varepsilon)-G_k^A(\varepsilon)\Big)\\ + v_j\Big(G_k^R(\varepsilon)-G_k^A(\varepsilon)\Big)S_iG_k^R(\varepsilon+\hbar\omega)\Big].\end{aligned} \tag{2.57}$$

Chapter 3

Current-induced spin polarization in Rashba–Dresselhaus systems

In the previous chapter, we have seen how spin–orbit coupling enables the generation of spin polarization in response to an external electric field. We now turn to its realization in specific low-dimensional systems where the underlying symmetry and the structure of spin–orbit interaction play a crucial role in determining the resulting behavior. In this chapter, we demonstrate that electrically induced spin polarization in non-magnetic materials can be significantly influenced by the system's point-group symmetries, such as C_n and C_{nv}, particularly in low-dimensional systems such as quantum-well structures. These symmetries allow various linear and higher-order momentum, $\mathbf{k}-$varying SOC Hamiltonian. Specifically, we show that surfaces having C_n point-group symmetry, which permits specific linear and cubic Rashba and Dresselhaus SOC terms, can lead to both orthogonal and non-orthogonal spin polarizations with respect to the applied field. In contrast, surfaces with C_{nv} symmetry exhibit only transverse spin polarization, regardless of the linear and cubic SOC terms. We further find that the spin polarization of cubic-in-k SOC contrasts with that of linear-in-k SOC as the energy is varied, for example, through doping. Additionally, we show that the surfaces with C_n symmetry may exhibit persistent spin current, depending on the relative strength between different momentum-dependent SOC terms. Our findings emphasize the significance of crystal symmetry in understanding and manipulating induced spin polarization in

noncentrosymmetric materials, especially in surface/interface systems.

3.1 Introduction

Creating dissipationless transport is a central goal in modern quantum transport phenomena, particularly in generating and tunneling of pure spins using electrical currents within quantum devices [74–76]. The key quantity that controls such spin generation and/or transport in materials with broken inversion symmetry is the spin-orbit coupling [58], which has been introduced earlier in Sec. 2.2. This SOC term that linearly depends on momentum in the presence of structure-inversion asymmetry (SIA) gives rise to an isotropic splitting of electronic bands—the linear Rashba effect [57, 77–80](see Sec. 2.5). The splitting of these bands can range from giant to colossal, depending on the intricate band structure, which involves orbital mixing and the interplay between spin-orbit coupling energy and inversion-breaking crystal field energy[65, 81]. Additionally, orthogonal orbital interactions in certain material systems are shown to induce colossal Rashba coupling [82]. An analogous band splitting in the presence of bulk-inversion asymmetry (BIA) also occurs due to the Dresselhaus spin-orbit coupling (DSOC) [66], which we have earlier discussed in Sec. 2.6. The utilization of such SOC terms in non-centrosymmetric materials has led to numerous nontrivial quantum states, transport phenomena, and interaction effects, promising for potential applications in devices [83–86]. The Rashba Edelstein effect (REE) is one of such phenomena where a non-equilibrium spin polarization is induced by an electrical current due to the presence of Rashba spin-orbit coupling (RSOC) [22, 23, 70, 87–89] whose underlying physical mechanism has been discussed in Sec. 2.7 of previous chapter. Since its first prediction, a great volume of work has focused on studying the REE in semiconductors, metallic surfaces, and later extending it to the topological materials [81, 90–97]. Similarly, a related phenomenon, namely orbital Edelstein effect as predicted in bulk antiferromagnets [98] has attracted considerable interest in recent times. Nonetheless, the REE can also lead to spin-orbit torques, which emerge as a promising candidate for the electrical manipulation of magnetic order [99, 100].

In non-centrosymmetric systems, the RSOC for degenerate atomic orbitals such as p, d, and

f orbitals induces a momentum-dependent spin splitting. This splitting can extend beyond the linear regime, giving rise to more complex physical phenomena. Often, these systems exhibit a cubic dependence of band splitting on momentum (k) [101–106]. Unlike the linear-in-k SOC that induces uniform splitting in Rashba bands, the cubic counterpart creates a directionally dependent energy separation that varies with momentum. Moreover, due to the presence of specific cubic terms allowed by the crystalline symmetry, materials with C_{3v} or C_{4v} point group symmetry exhibit anisotropic spin splitting [107–112]. Various electron and hole systems have been experimentally found to exhibit spin-splitting anisotropic in k [113–115]. For example, $SrTiO_3$ surface [102], $SrTiO_3$-based asymmetric oxide heterostructures [116], Ge/SiGe quantum well [104], antiferromagnet $TbRh_2Si_2$ [117] are known to show non-linear spin splitting in their surface/interface electronic structures. Additionally, recent research in bulk insulators has revealed materials exhibiting purely nonlinear RSOC where various ST govern controlled manipulation of dissipationless transport. In Ref. [2], current-induced spin polarization has been studied in C_{2v} surface with only mass anisotropy and in C_{3v} surfaces with out-of-plane cubic term in addition to the in-plane RSOC. Similar cubic RSOC has been used in Ref. [118] and in Ref. [119] to discuss spin polarization and conductivity. Despite the intriguing physics observed in higher-order momentum terms under various point group symmetries, a comprehensive understanding of their influence on induced spin in the presence of electric fields remains elusive. Notably, a systematic investigation is lacking that explores this effect across both symmetry-preserved and symmetry-broken materials. This is expected to be of relevance for the interpretation of possible spin-polarization measurements detecting the Rashba spin splitting beyond the linear limit.

In view of the above, we provide a detailed and comprehensive study of current-induced spin polarization in a two-dimensional electron gas (2DEG) under different point group symmetries, particularly $C_{3/3v}$ and $C_{4/4v}$ symmetries. We note that semiconductor quantum well structures and two-dimensional nanostructures with carefully chosen growth geometries can host 2DEG with such symmetries. By employing the Kubo formalism, we show that under C_3 or C_4 symmetry, a combination of standard RSOC and a symmetry-allowed linear term (dubbed as DSOC(+)) leads to isotropic spin polarization, independent of their relative strengths. This is in contrast to the

case where both Rashba and standard DSOC, namely DSOC(−), together lead to anisotropic spin polarizations [50, 120–123]. We further supplement these findings by solving the time-dependent Schrödinger equation, particularly showcasing the evolution of spin polarization under the influence of an in-plane electric field applied in any direction. Remarkably, we find that the components of spin-polarization switches sign along the orthogonal directions of the applied field for DSOC(+) in contrast to the DSOC(−) where no such sign change is found (Sec. 3.3.1). Moreover, we find a special situation where the collinear alignment of Rashba and DSOC(−) leads to the persistent spin texture (PST). This, in turn, gives rise to zero spin polarization in the presence of the applied field.

Similar to the linear term, purely cubic RSOC and DSOC terms together under C_3 or C_4 point group symmetry can host both orthogonal and non-orthogonal spin polarization in the presence of an electric field. However, the magnitude of the spin polarization increases with the Fermi energy as opposed to the linear case where it reduces with the Fermi energy due to the partial compensation of spin polarization from carriers of opposite chirality (Sec. 3.3.2). Interestingly, in symmetry-enriched electronic systems characterized by C_{3v} or C_{4v} symmetries, we find only transverse polarization even in the presence of cubic RSOC. However, the magnitude of spin polarization under C_{4v} surfaces substantially differ from that of systems with C_{3v} symmetry (Sec. 3.3.2.1). Specifically, we find that the anisotropy of the FC overall reduces the magnitude of spin polarization in C_{4v} and it strongly depends on the orientation of the applied field. Additionally, the C_{4v} symmetry allowed mixed cubic RSOC leading to net zero polarization due to the deformed nature of the FCs (Sec. 3.3.2.2), regardless of the direction of the applied field. This effect is also manifested in the total spin polarization as we vary the Fermi energy. We finally conclude with a discussion on how the spin polarization as a function of the direction of the electric field can assist in identifying the symmetry properties of the materials.

3.2 Theoretical background

We begin by reviewing the REE within a 2DEG model system [57]. The corresponding Hamiltonian with the linear-in-k RSOC term is

$$H_0 = \frac{\hbar^2 \mathbf{k}^2}{2m} + \alpha(k_x\sigma_y - k_y\sigma_x), \tag{3.1}$$

where $\mathbf{k} \in (k_x, k_y)$ represents the 2D crystal momentum, $\boldsymbol{\sigma}$ denotes the Pauli matrices, and α corresponds to the linear Rashba coupling parameter. This linear coupling induces a spin-splitting in the energy bands that scales linearly with the crystal momentum as shown in Fig. 3.1(a). This is typically termed as the linear Rashba splitting. In standard Rashba Hamiltonian, α is given by the ratio $\alpha = 2E_\mathrm{R}/k_\mathrm{R}$ between the spin splitting energy E_R and the momentum offset k_R [124, 125]. Insets of Fig. 3.1(a) shows the spin helicities on the inner and outer FCs at zero field at two different energies $\varepsilon > \varepsilon_0$ (left) and $\varepsilon < \varepsilon_0$ (right), where $\varepsilon_0 = 0$ refers to the band crossing point at zero momentum. Clearly, the spins are perpendicular to the motion of electrons, indicating the spin-momentum locking of the system. Moreover, for $\varepsilon > \varepsilon_0$, spins in the inner and outer FCs are found to align antiparallel to each other as opposed to the case for $\varepsilon < \varepsilon_0$. We note that the magnitudes of spins in each FC depend on ε_F, which in turn modify the induced $\langle S^{in}\rangle$ and $\langle S^{out}\rangle$ in the presence of electric field as will be discussed shortly. Using the Kubo formalism, we first compute the spin polarization in the presence of an external static electric field $\mathbf{E}$. Following Eq. 2.57, the spin polarization in the frequency domain and linear response regime, can be expressed as [71–73],

$$\begin{aligned}\langle S_i(\omega)\rangle = -\frac{eE_j}{\omega}\int \frac{d\varepsilon}{2\pi} f(\varepsilon) \sum_k \mathrm{Tr}\big[\hat{v}_j G_A(\varepsilon - \hbar\omega, \mathbf{k})\hat{S}_i \\ [G_R(\varepsilon, \mathbf{k}) - G_A(\varepsilon, \mathbf{k})] + \hat{v}_j[G_R(\varepsilon, \mathbf{k}) - G_A(\varepsilon, \mathbf{k})] \\ \hat{S}_i G_R(\varepsilon + \hbar\omega, \mathbf{k})\big],\end{aligned} \tag{3.2}$$

where $(i, j) \in (x, y, z)$, e is the electron's charge and $f(\varepsilon)$ is the Fermi distribution function. $\hat{v}$ and $\hat{S}$ are the velocity operator and the spin operator, respectively. G_R and G_A are the retarded and

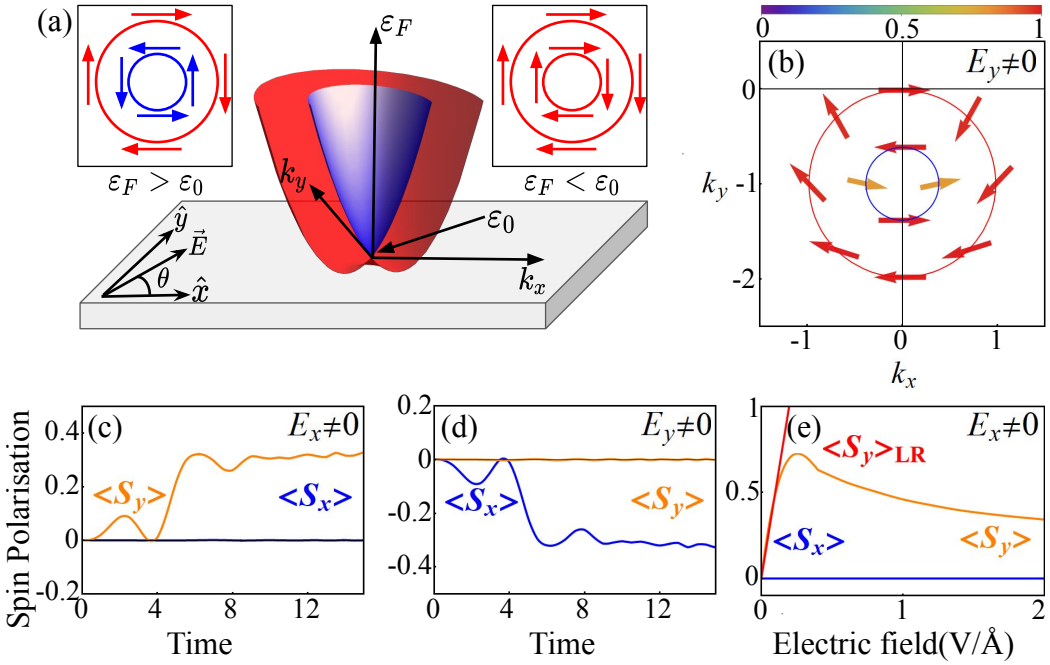

Figure 3.1: (a) The schematic of a 2DEG setup under a static electric field **E**. With the linear RSOC, a free electron state splits into two subbands with opposite spin textures (red and blue) that intersect at the band crossing point. The corresponding energy is defined as $\varepsilon_0 = 0$. The left inset shows spin orientation along FCs for $\varepsilon > \varepsilon_0$, and the right inset shows the same for $\varepsilon < \varepsilon_0$ at zero electric field. (b) Snapshot of spin polarization at a particular instant of time ($t = 2.6$ fs) for the electric field along y, obtained by solving the time-dependent Schrödinger equation. Evidently, the FCs move in the opposite to the applied field. (c-d) Time evolution of momentum-averaged (over both the FCs at $\varepsilon_F = 0.63$ eV) spin polarization $\langle S_x \rangle$ and $\langle S_y \rangle$ per unit area for the field along x and y, respectively. (e) Time and momentum-averaged spin polarization as a function applied field along x. For weak fields, it varies linearly and exhibits the same symmetry-allowed spin-polarization direction as the Kubo result ($\langle S_y \rangle_{\rm LR}$) for the outer FC. Thus, the real-time calculation serves as a complementary dynamical study of the Kubo result. Here, we take $\alpha = 1$ eV.Å. Also, throughout the text, we use $\hbar^2/2m$ =1.66 eV.Å^2, E =0.25 V/Å, the unit of time is 0.66 fs, and k_x and k_y in units of Å^{-1}; the color bar shows the magnitude of each spin polarization.

advanced Green functions, respectively. $G_R^{-1}(\omega, \mathbf{k})_{nn'}$ ($G_A^{-1}(\omega, \mathbf{k})_{nn'}$) is defined as $(\hbar\omega - H + i\eta)$ $((\hbar\omega - H - i\eta))$, where the broadening parameter η represents the inverse of the relaxation time τ and takes into account the finite lifetime of electron states with n, n' as their band indices. At zero temperature, ith of component of the induced spin polarization can be written as (restricting to the linear expansion in ω of the Green's function)

$$\langle S_i(\omega) \rangle = \frac{eE_j}{2\pi} \sum_k \mathrm{Tr}[\hat{v}_j G_A(\omega) \hat{S}_i G_R(\omega)]. \tag{3.3}$$

In case of an applied electric field along x, *i.e.* $\mathbf{E} = (E_x, 0, 0)$, a straightforward calculation (Appendix A) leads to

$$\langle S_y \rangle \approx \frac{eE_x\varepsilon_F}{32\pi\alpha\eta}, \langle S_x \rangle = \langle S_z \rangle = 0, \tag{3.4}$$

where ε_F is the Fermi energy. Thus, we obtain $\mathbf{S} = (0, S_y, 0)$, indicating a transverse spin polarization, and we recover the conventional REE. This can also be understood from Eq. (3.1) itself, where one can rewrite the Rashba term as $H_R = \mathbf{B}_{\text{eff}} \cdot \boldsymbol{\sigma}$ with $\mathbf{B}_{\text{eff}} = \alpha(-k_y, k_x)$. The static electric field along $\hat{x}$ couples to the y component of $\mathbf{B}_{\text{eff}}$ via Peierls substitution $k_x \rightarrow k_x + A_x$, A_x being the x-component of the gauge potential due to the field. This, in turn, leads to the spin polarization along $\hat{y}$.

This outcome can be further validated by studying the temporal evolution of the induced spin polarization under the applied electric field $\mathbf{E}(t)$. This involves solving the time-dependent Schrödinger equation $i\partial_t H|\psi\rangle = \varepsilon|\psi\rangle$ with the gauge potential $\partial_t A(t) = -e\mathbf{E}(t) \cdot \hat{\boldsymbol{r}}$, where $\hat{\boldsymbol{r}}$ is the position operator. Notably, the gauge potential is introduced in the Hamiltonian through the momentum term by means of momentum translation, *e.g.*, $k_y \rightarrow k_y + A_y(t)$ for a static field along $\hat{y}$. This led us to find evolved wave functions, which are used to compute expectations of different spin operators at an instant of time and for a finite ε_F. Figures 3.1(b) depict the shifts of FCs under the applied static field along y, while the snapshots of spins at an instant of time capture the spin polarization on the contours. It is evident that the FCs move oppositely away from the direction of the applied field. Furthermore, in comparison to the *spin-momentum locking* in Fig. 3.1(a)(inset), the time-dependent spins (*i.e.*, $\langle\psi|\,\boldsymbol{\sigma}\,|\psi\rangle_k$) in the k_x-k_y plane on both the FCs orient at arbitrary directions during the short-time evolution. Consequently, the magnitudes of resultant induced polarization involving both inner and outer FCs, $\langle S_{x(y)} \rangle = \langle S_{x(y)} \rangle_{\text{in}} + \langle S_{x(y)} \rangle_{\text{out}}$, oscillate initially and then gradually saturates (reaches to a nearly constant value) over time. The converged final value is smaller than the actual value of the outer FC since the spin polarizations of the inner FC are opposite and smaller in magnitude. Figures 3.1(c) and (d) illustrate these features, showing the variation of saturated spin polarization $\langle S_{y(x)} \rangle$ as a function of time for the field applied along $x(y)$. In this approach, it is evident that the magnitudes of both the spin components, $\langle S_x \rangle$ and $\langle S_y \rangle$ eventually saturate in the

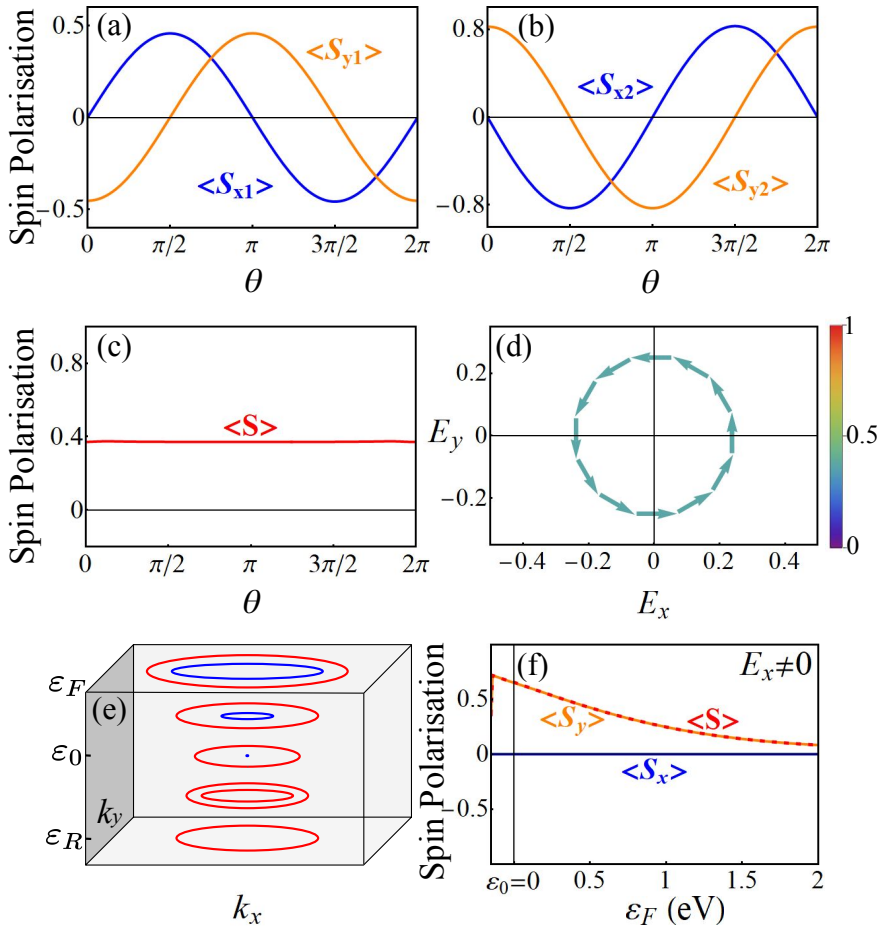

Figure 3.2: (a-b) x and y components of spin polarization per unit area as a function of the direction of the applied field for inner (1) and outer (2) FCs at $\varepsilon_F = 0.63$ eV, (c) Total time-averaged and momentum averaged (over both the FCs at ε_F) spin polarization as a function of the direction of the applied field, (d) Resultant time and momentum averaged spin polarization as a function of electric field in the E_x-E_y plane. (f) Fermi energy dependence of different spin components and total spin polarization for the electric field along x. The vertical line represents $\varepsilon_F = \varepsilon_0$. (e) illustrates FCs as a function of energy and the color code refers to the relative orientation of the spin in both the FCs.

long-time limit. In Fig. 3.1 (f), we have computed the time-averaged saturation value of $\langle S_y \rangle$ as a function of the applied field, $\mathbf{E} = (E_x, 0, 0)$. Note that the spin polarization is linear in the weak field limitand exhibits the same symmetry-allowed response predicted by the Kubo formalism in Eq. (3.4). However, its field-dependent behavior exhibits a maximum at a certain field, undergoing significant changes for stronger fields. For simplicity and without loss of generality, we restrict to the linear regime (Fig. 3.1 (f)) for the rest of this article. Since the real-time evolution does not include relaxation processes, the Fermi contour continues to drift under the applied electric field,

and the dynamics need not remain within the strict linear-response regime. Therefore, the real-time calculations should be viewed as a complementary dynamical analysis rather than a direct verification of the Kubo-response results. A more direct comparison with the Kubo formalism would require approaches that incorporate finite relaxation processes, such as Boltzmann transport theory [2], whereas the real-time dynamics may alternatively be interpreted in terms of Landau–Zener tunneling [70].

The concentric isotropic FCs, characteristic of the linear Rashba effect, are then manipulated by an applied electric field $\mathbf{E} = (E\cos\theta, E\sin\theta, 0)$, confining within the plane of a 2DEG. Here, θ denotes the angle of the static field defined with respect to the 2DEG coordinates, as indicated schematically in Fig. 3.1(a). We note that similar concentric FCs had also been demonstrated at the surface of $SrTiO_3$ [126]. Figures 3.2 (a) and (b) demonstrate the saturated polarization of $\langle S_x\rangle$ and $\langle S_y\rangle$ as a function of θ for the inner (1) and outer (2) FCs, respectively. The magnitude of both $\langle S_x\rangle$ and $\langle S_y\rangle$ for both the FCs oscillates with θ. However, the total spin polarization, defined as $\langle S\rangle = \sqrt{(\langle S_x^{in}\rangle + \langle S_x^{out}\rangle)^2 + \langle S_y^{in}\rangle + \langle S_y^{out}\rangle)^2}$, remains constant, independent of θ. Here *in* and *out* refer to the inner and outer FCs, respectively. The corresponding plot is shown in Fig. 3.2(c). In Fig. 3.2(d), we illustrate the direction of spin polarization with $\mathbf{E}$ in the E_x-E_y plane. The polarization turns out to be transverse to the direction of the applied field, corroborating the results of standard linear REE. For a field along any arbitrary θ value, both the spin components may exist; however, the total induced spin polarization remains constant in magnitude. Unless explicitly mentioned otherwise, the induced spin polarizations are discussed at their saturation values (long-time limit) in the remaining sections of the article.

An important characteristic of the RSOC is its controllability through an external gate voltage applied to the 2DEG [14, 127]. The Rashba parameter is directly influenced by the surface/interfacial potential drop, and adjusting the electron occupation can be achieved by applying a gate voltage [128], light [126] *etc*. It is also evident from the Fig. 3.2(e), the size of these two concentric FCs can be controlled by varying the energy through doping. The energy at the zero-momentum point, where the two Rashba bands intersect, is set to $\varepsilon_0 = 0$. The point is represented as the band crossing point. We, therefore, focus on exploring how spin polarization varies with ε_F for a given electric field along

$\hat{x}$. At $\varepsilon_F = \varepsilon_0$, the induced polarization originates exclusively from the outermost FC since there is no inner FC. This closely resembles the FC on the surface state of topological insulators above the Dirac point, such as the elemental topological insulator α-Sn [129]. The resulting spin polarization $\langle S \rangle$ as a function of ε_F is shown in Fig. 3.2(f). Unlike a topological insulator, as ε_F increases (> 0) away from the band crossing point, the spin polarization $\langle S \rangle$ gradually diminishes to zero. This reduction is attributed to the partial compensation of spin polarization from carriers with opposite spin chirality in the inner and outer FCs above the band crossing point. Conversely, a decrease in $\varepsilon_F (< 0)$ for carriers with energy below the band crossing point leads to an enhancement of $\langle S \rangle$ due to the cooperative contributions of the identical spin helicities from the outer bands.

3.3 Spin polarization in surfaces with linear and non-linear terms under different symmetries

The splitting of energy bands induced by SOC and the associated spin-momentum locking, originating from the effective magnetic field within a Rashba Hamiltonian (cf. Eq. 3.1), often deviate in systems with bulk-inversion asymmetry. In a typical linear SOC limit with BIA, DSOC emerges, and the interplay between these two SOC contributions is observed in a wide class of noncentrosymmetric materials [130–132]. This leads to anisotropic FCs where the spin-momentum locking may no longer remain orthogonal [133, 134]. Moving into the nonlinear k-dependent spin splitting, notable examples such as semiconductor quantum wells [104, 135], oxide surfaces, and interfaces [136, 137] exhibit the presence of cubic Rashba terms, which manifest in various forms within the Hamiltonian. Remarkably, the effective momentum-dependent magnetic field discussed before takes a distinct form in the presence of cubic SOC terms than its linear counterpart. This enables the **k**-dependent *pseudospin* in those systems to undergo faster rotation around the FCs and the *pseudospin* vector is no longer orthogonal to **k** everywhere [117, 136, 138]. The presence of these terms in the Hamiltonian can result in diverse and unconventional field-induced spin polarizations. Surprisingly, despite their potential applications in spintronics and valleytronics, the comprehensive understanding of how the various linear and non-linear-in-k SOC, including DSOC, determine the spin polarization pattern

has been largely overlooked. Therefore, in the next, we focus on the theoretical investigations of the Hamiltonian in Eq. 3.1 in the presence of linear-in-k dependent DSOC terms allowed by various symmetries such as C_3, C_4, C_{3v} and C_{4v} symmetries [101]. Thereafter, we investigate Eq. 3.1 in the presence of higher-order SOC terms, particularly the symmetry-allowed cubic RSOC and DSOC terms. We note that these SOC terms in the Hamiltonian are primarily adopted from Ref. [101].

3.3.1 Interplay between RSOC and DSOC within generalized linear regime

We now construct quantum well models in the presence of SIA, BIA, or a combination of both, aiming to investigate current-induced spin polarization in 2DEG. The model is built upon a symmetry-adapted linear-in-k approximation for the SOC effect. The simultaneous presence of SIA and BIA occurs in lower point-group symmetries, allowing linear terms such as $\beta(k_x\sigma_x + k_y\sigma_y)$, $\beta(k_x\sigma_x - k_y\sigma_y)$, etc. [101] in the Hamiltonian. The first term is referred to as DSOC(+), while the second is labeled DSOC(−) and is commonly known as the standard Dresselhaus term. Note that each of the individual linear terms considered (without RSOC) exhibits distinct ST on the FCs (see Sec. 2.6), and subsequently, they show longitudinal spin polarization feature with respect to the applied field with an opposite sign (see Appendix A). This occurs because, even though the eigenvalues of both Hamiltonians are identical, the wavefunctions differ only by phase. Consequently, we observe distinct behavior in the spin polarization phenomena in the linear regime due to the interplay between the RSOC parameter α and DSOC parameter β.

3.3.1.1 RSOC + DSOC(+)

We first focus on the DSOC(+) without and with the RSOC term within the linear-in-k SOC limit. The full Hamiltonian reads of

$$H = \frac{\hbar^2 k^2}{2m} + \alpha(k_x\sigma_y - k_y\sigma_x) + \beta(k_x\sigma_x + k_y\sigma_y). \tag{3.5}$$

The Hamiltonian in Eq. 3.5 characterizes a 2DEG without mirror symmetry under point group C_3 or C_4 [101]. For simplicity, we relate the coefficients α and β by defining an angle $\Phi = \tan^{-1}(\beta/\alpha)$,

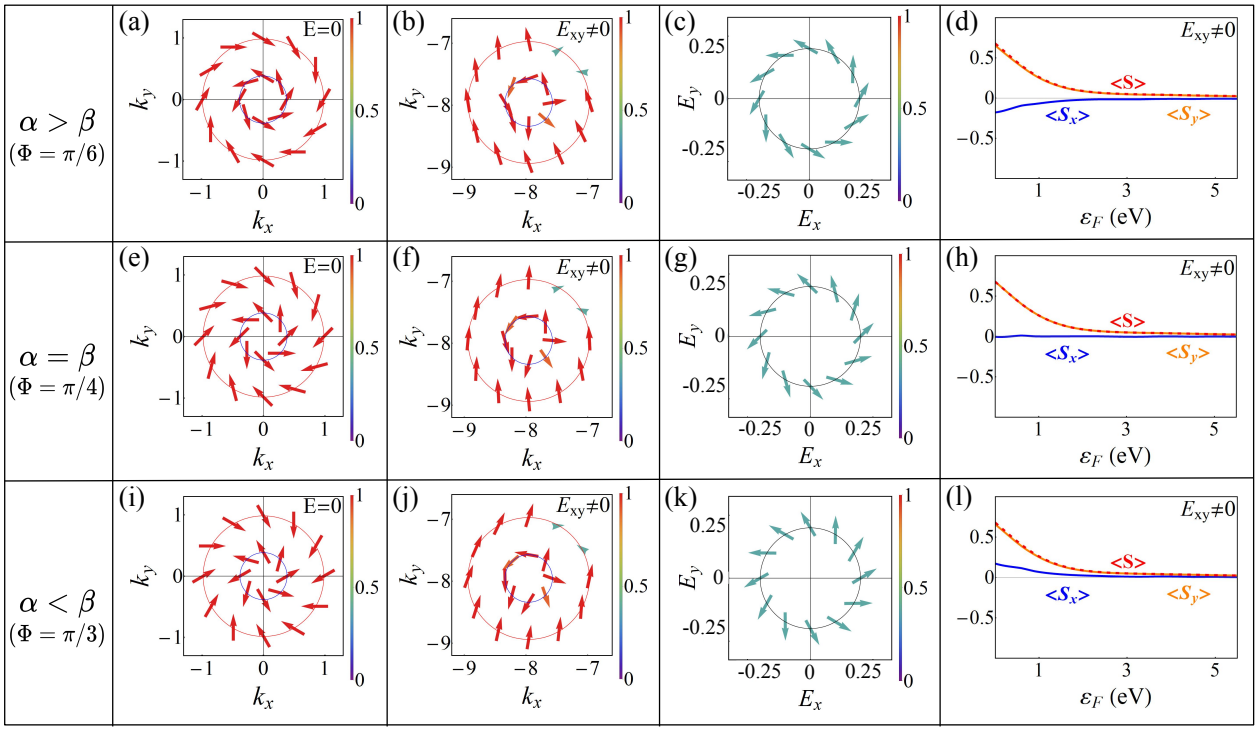

Figure 3.3: Spin orientations of the 2DEG together with RSOC and DSOC(+) for their different relative strengths $\alpha > \beta$, $\alpha = \beta$, and $\alpha < \beta$, respectively (considering $\alpha^2 + \beta^2 = 1$). (a, e, i) Plot of zero field STs. The variation of STs from Rashba-like to radial Weyl-like is evident. (b, f, j) Snapshot of spin orientation for the field along xy at constant energy surface $\varepsilon_F = 0.63$ eV and at a particular instant of time ($t = 29.7$ fs). (c,g,k) The resultant time and momentum averaged spin polarization in the $E_x - E_y$ plane for both FCs at $\varepsilon_F = 0.63$ eV. (d,h,l) Variation of spin polarization per unit area with the Fermi energy.

while maintaining $\alpha^2 + \beta^2 = 1$. In standard Rashba-Dresselhaus systems, the STs varies depending on the value of Φ; $\Phi = 0$ and $\pi/2$ represent pure Rashba and Dresselhaus systems, respectively. For the later case, diagonalizing only the DSOC(+) term yields radial STs, where the spin is always aligned parallel to the wave vector $\mathbf{k} = (k_x, k_y, 0)$, historically referred to as the *Weyl*-type STs [123, 139–141]. This type of ST has recently been realized in chiral bulk crystals, where both mirror and inversion symmetries are absent [142, 143]. When subjected to an applied electric field, this term generates spin polarization parallel to the direction of the electric field, contrasting sharply with the pure Rashba systems (associated with C_{3v} or C_{4v} point group), where the induced spin polarization is perpendicular to the field. The ability to tune the α and β parameters is therefore expected to manifest in a controlled ST within the FCs, thereby influencing the spin polarization induced by an electric field. As before, using the Kubo formalism, the induced spin polarization

components for $\mathbf{E} = (0, E_y, 0)$ are found to be (see Appendix A for detailed derivation)

$$\begin{aligned}\langle S_x \rangle &\approx -\frac{eE_y \alpha \varepsilon_F}{32\pi\eta(\alpha^2+\beta^2)};\\ \langle S_y \rangle &\approx \frac{eE_y \beta \varepsilon_F}{32\pi\eta(\alpha^2+\beta^2)};\\ \langle S_z \rangle &= 0.\end{aligned} \tag{3.6}$$

Clearly, upon looking at each spin polarization component, it is evident that the transverse component $\langle S_x \rangle$ varies with α, while the longitudinal component $\langle S_y \rangle$ varies with β but with an opposite sign. In contrast, for the field $\mathbf{E} = (E_x, 0, 0)$, we find that both $\langle S_x \rangle$ and $\langle S_y \rangle$ have the same sign, as expressed by:

$$\begin{aligned}\langle S_x \rangle &\approx \frac{eE_x \beta \varepsilon_F}{32\pi\eta(\alpha^2+\beta^2)};\\ \langle S_y \rangle &\approx \frac{eE_x \alpha \varepsilon_F}{32\pi\eta(\alpha^2+\beta^2)};\\ \langle S_z \rangle &= 0.\end{aligned} \tag{3.7}$$

Such contrasting behavior of $\langle S_x \rangle$ and $\langle S_y \rangle$ for the fields along $\hat{x}$ and $\hat{y}$ directions can be understood by the effective momentum-dependent magnetic field $\mathbf{B}_{\text{eff}}(\mathbf{k}) = (\beta k_x - \alpha k_y, \alpha k_x + \beta k_y)$ acting on spin $\boldsymbol{\sigma}$. The sign of k_y in the x and y components of $\mathbf{B}_{\text{eff}}$ differs. Accordingly, the external field along $\hat{y}$ couples to both k_y via Peierls substitution, resulting in spin polarization along $\hat{x}$ and $\hat{y}$ directions with a different sign. However, the field along $\hat{x}$ produces the same sign of $\langle S_x \rangle$ and $\langle S_y \rangle$ since the sign of k_x is the same in both the components of $\mathbf{B}_{\text{eff}}$. Note that this is one of the *crucial* results which has been overlooked in the existing literature [121, 144]. The orientation of spins around the FCs is influenced by the sign change in $\langle S_x \rangle$ and $\langle S_y \rangle$, as will be detailed shortly.

To corroborate the result of Kubo formalism, we solve the time-dependent Schrödinger equation using the Hamiltonian in Eq. (3.5) and subsequently, we compute the spin polarization after the time evolution. The STs for different values of Φ ($= \pi/6$, $\pi/4$, and $\pi/3$) is shown in Fig. 3.3(a),(e) and (i) at zero electric field. The FCs remain isotropic and circular regardless of the values of α and β.

However, it is evident that the ST around both FCs varies, ranging from the conventional tangential Rashba STs ($\beta = 0$ case) to radial Weyl-type STs ($\alpha = 0$ case). This interplay, which governs controlled STs, could provide a productive foundation for designing compounds with specific target STs, consequently allowing precise control over the induced spin polarization vector. For example, both the spin polarization $\langle S_x \rangle$ and $\langle S_y \rangle$ are finite for finite α and β, regardless of the direction of the applied field. Accordingly, in response to an electric field perturbation ($e.g.$, $\mathbf{E}_{xy} \neq 0$), the orientation of spins in the ST starts to adjust, deviating from their initial direction as observed in the k_x-k_y plane, see FCs in Figs. 3.3(b), (f) and (j). After a sufficiently long time, the momentum-dependent pseudospins lead to an induced moment, and the orientation of its vector varies with the change in the direction of the applied electric field. This is illustrated in Figs. 3.3(c), (g), and (k), which show the induced in-plane spin moment vector $\mathbf{S} = \langle S_x \rangle \hat{x} + \langle S_y \rangle \hat{y}$ as a function of the direction of an in-plane $\mathbf{E}$. We observe orthogonal Rashba-like and radial Weyl-like ST in the induced polarization concerning the direction of $\mathbf{E}$, corresponding to Φ values of 0 and $\pi/2$, respectively (not shown here). The orientation of the spin moment, given by ($\langle S_x \rangle$, $\langle S_y \rangle$, 0), varies with the direction of $\mathbf{E}$ in the xy-plane, aligns with the analytical predictions derived from the Kubo formula. Regardless of the direction of the field, we consistently observe the rotation of induced moment while its magnitude remains constant, as indicated by different Φ values. This directly demonstrates that the electrically induced polarization depends on the underlying spin texture itself. In Fig 3.3(d),(h),(l), we illustrate how the induced polarization changes as the Fermi level varies. As discussed earlier, the magnitude of the spin polarization gradually diminishes.

3.3.1.2 RSOC + DSOC(−)

In the linear-in-k SOC Hamiltonian (see Eq. 3.5), it is worth noting that the Dresselhaus term does not have a unique expression. The derivation of k-dependent SOC terms typically arises from zone-center solutions of the $\mathbf{k}.\mathbf{p}$ theory [145]. The Hamiltonian incorporating the standard Dresselhaus term is expressed as:

$$H = \frac{\hbar^2 k^2}{2m} + \alpha(k_x\sigma_y - k_y\sigma_x) + \beta(k_x\sigma_x - k_y\sigma_y). \tag{3.8}$$

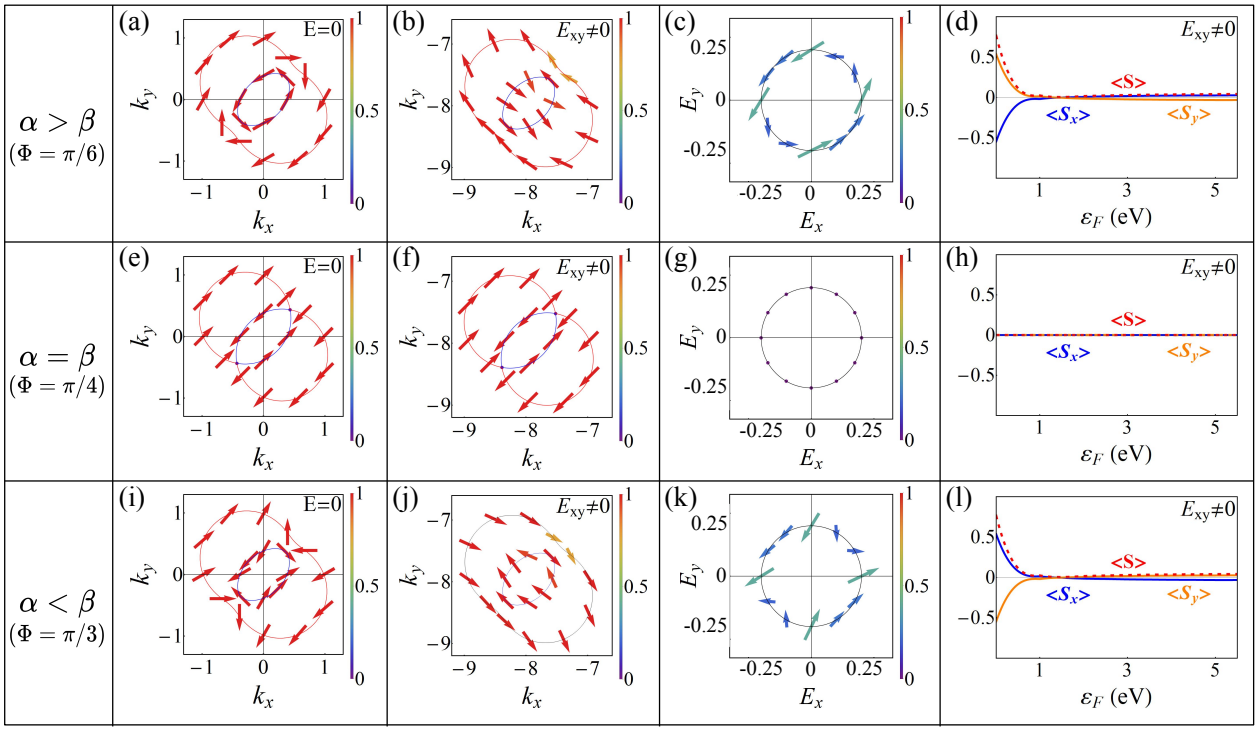

Figure 3.4: Same as Fig. 3.3 for the 2DEG together with RSOC and DSOC(−). Note that the spin polarization here differs significantly from the DSOC(+) case, as elaborated in the main text. Additionally, the $\alpha = \beta$ case is even more interesting as it shows persistent ST. Consequently, the net-induced spin polarization becomes zero.

Such a Hamiltonian can describe the interfacial SOC effect in III-V semiconductor quantum wells [146]. Diagonalizing standard Dresselhaus term, denoted as DSOC(−), we obtain *tangential-radial* spin orientation on FCs, commonly known as the Dresselhaus STs. Surprisingly, the findings outlined in the preceding section exhibit substantial distinctions from the outcomes obtained by analyzing the electric field response for the Hamiltonian in Eq. 3.8. Results are summarized in Fig. 3.4. Such contrasting results, even within the linear-in-k SOC limit, arise from the specific design of the 2DEG interface systems. In this scenario, the FC no longer remain circular; instead, there is a lateral shift along the diagonal of k_x-k_y plane. We note here that the anisotropic spectrum in the ST complicates the derivation of simple expressions for $\langle S_x \rangle$ and $\langle S_y \rangle$. However, the sign of $\langle S_x \rangle$ and $\langle S_y \rangle$ can be determined using the effective magnetic field $\mathbf{B}_{\text{eff}} = (\beta k_x - \alpha k_y, \alpha k_x - \beta k_y)$. Since both the components of $\mathbf{B}_{\text{eff}}$ are having a similar sign with k_x and k_y, the sign of $\langle S_x \rangle$ and $\langle S_y \rangle$ are expected to be same.

The induced spin polarization shown in Fig. 3.4 for $\Phi = \pi/6$ and $\pi/3$, respectively (Fig. 3.4

c and k), varies in magnitude depending on the direction of the electric field. Evidently, the ST on the FCs differs substantially from those discussed in the previous DSOC(+) case. Additionally, the asymmetric nature of the FCs leads to a more rapid decay of spin polarization to zero with increasing ε_F shift compared to the DSOC(+) case (see Fig. 3.4(d) and (l)). In the present case, a special situation arises when the Rashba and Dresselhaus parameters in the Hamiltonian are of equal magnitude at $\Phi = \frac{\pi}{4}$ ($\alpha = \beta$). The ST remains invariant with momentum as the effective magnetic field $\mathbf{B}_{\text{eff}} = (\alpha(k_x - k_y), \alpha(k_x - k_y))$ becomes a constant vector, leading to a persistent spin texture with unidirectional spin alignment [147]. This is evident from the time evolution of pseudospins on FCs, compare STs in Figs. 3.4(e) and (f). Consequently, the system does not respond to the applied field, resulting in zero spin polarization as shown in 3.4(h).

An earlier study demonstrated anisotropic transport in semiconductor quantum wells that confine electron gas under the influence of both the RSOC and DSOC(−) term. This anisotropy is determined by the interplay between the α and β parameters [144]. We highlight that the spin polarization obtained within the REE framework, considering the presence of RSOC and standard DSOC(−), exhibits anisotropy in induced polarization. The contrasting behavior of the DSOC(+) and DSOC(−) terms in response to an electric field is illustrated in Fig. 3.5, as a function of Φ. For a given applied field along $\theta = 0$ and $\pi/2$, the magnitude of induced polarization ($|\mathbf{S}|$) remains almost constant with Φ in the case of DSOC(+), while it gradually decreases to zero for DSOC(−) at $\Phi = \pi/4$, i. e., at the regime of PST. Although the PST has been acknowledged for its vital role in establishing an infinite spin lifetime [122], it is worth noting that the induced spin polarization vanishes in the presence of the electric field.

3.3.2 Non-linear regime: the symmetry allowed cubic order effect

The orientation of spins with momentum in a more complex ST, governed by higher-order SOC terms, enables the emergence of exotic current responses in non-centrosymmetric materials. For example, cubic-in-k^3 Rashba terms can substantially change the spin polarization in heavy hole quantum well than the linear-in-k Rashba SOC [104, 148]. Although the cubic term, in general, accompanies the linear-in-k term, some experiments reported *purely* cubic-in-k Rashba SOC in sur-

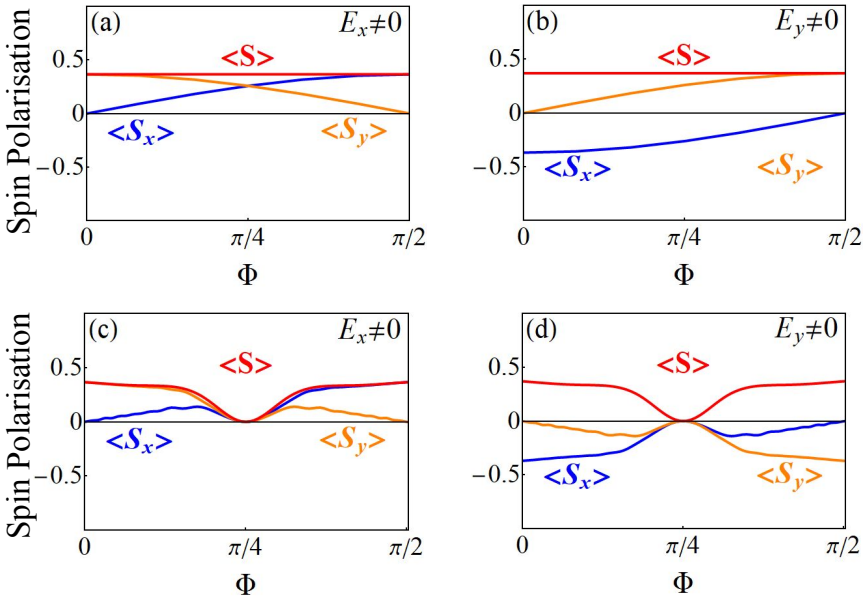

Figure 3.5: Induced spin polarization (at $\varepsilon_F = 0.63$ eV) as a function of $\Phi = \tan^{-1}(\beta/\alpha)$. (a,b) and (c,d) illustrate the interplay between the relative strengths of the DSOC(+) and DSOC(−) terms with respect to the RSOC term, respectively.

faces/interfaces of materials such as the surface of $SrTiO_3(001)$ [148], Ge/SiGe quantum well [104], asymmetric oxide heterostructures like $LaAlO_3/SrTiO_3/LaAlO_3$ [116], and surfaces of antiferromagnet $TbRh_2Si_2$ [117]. Bulk materials, particularly with $\bar{6}$ and $\bar{6}m2$ point groups [149], are also found to exhibit purely cubic SOC term. The cubic spin–orbit coupling terms considered in this section are adopted from Ref. [101], where symmetry-allowed spin–orbit terms up to third order in momentum were systematically identified using $k \cdot p$ perturbation theory and group-theoretical analysis. Since our primary focus is on their influence on current-induced spin polarization, we do not reproduce the symmetry-based derivation here and refer the reader to Ref. [101] for details.

3.3.2.1 Cubic terms associated with C_{3v} and C_3 symmetries

The two-band Hamiltonian with cubic Rashba terms associated with C_{3v} point group symmetry [101] is given by

$$H = \frac{\hbar^2 k^2}{2m} + \zeta_1((k_x^3 + k_x k_y^2)\sigma_y - (k_x^2 k_y + k_y^3)\sigma_x), \tag{3.9}$$

where ζ_1 is the strength of the cubic SOC. This higher-order RSOC usually manifests in [111]-oriented diamond and zinc-blende quantum wells, as well as in their surface states [145]. The eigenvalues of Eq. (3.9) can be easily obtained as $E_{\pm}=\hbar^2k^2/2m \pm \zeta_1 k^3$ and they are plotted in Fig. 3.6(a) over the range of $\pm|\mathbf{k}|$ in the (k_x, k_y) plane. To explore the Edelstein phenomena in this 2DEG setup, we ensure that the kinetic energy consistently dominates over the energy associated with the SOC term. Considering the concepts of the effective magnetic field discussed before, the presence of field $\mathbf{E} = (E_x, 0, 0)$ is expected to induce polarization in both the transverse and longitudinal directions of the applied field as both the Pauli matrices involves k_x and k_y in the Hamiltonian. Remarkably, Fig. 3.6(b) shows that the pure cubic RSOC results in transverse polarization, akin to the behavior exhibited by linear RSOC coupling in Fig. 3.2(d). This is because the effective magnetic field can be expressed as $\mathbf{B}_{\text{eff}}(\mathbf{k}) = \zeta_1 k^3(-\sin\delta,\ \cos\delta)$ which resembles the effective magnetic field for the linear-in-k case, $\mathbf{B}_{\text{eff}}(\mathbf{k}) = \alpha k(-\sin\delta,\ \cos\delta)$, where δ is the polar angle. The associated spin splitting turns out to be proportional to k^3 and isotropic (independent of δ), yielding concentric rings in the constant energy cut. The STs shown in the inset of Fig. 3.6(a) for energy $\varepsilon \neq 0$ also closely resembles that of the linear-in-k SOC Hamiltonian. In Figure 3.6(d), we depict the dependence of the net spin polarization $\langle S\rangle$ alongside its in-plane components, $\langle S_x\rangle$ and $\langle S_y\rangle$, with respect to the tunable Fermi energy, ε_{F}. Contrary to the behavior in the case of linear-in-k Rashba SOC (see Fig. 3.2(f)), the magnitude of spin polarization $\langle S\rangle$ increases with the increase in ε_{F}. This is attributed to the chiral spin texture in a single FC for $\varepsilon_{\text{F}} > 0.68$ eV (Fig. 3.6(c)). This strikingly resembles the phenomena arising from a single chiral surface state loop in a topological insulator [150]. Thus, in a more general context, the higher-order term acts as a tool to counteract the cancellation of current-induced spin density observed in standard linear REE. When mirror symmetry is broken, such as in the C_3 point group, a cubic-in-k Dresselhaus term, $\zeta_2((k_x^3 + k_x k_y^2)\sigma_x + (k_x^2 k_y + k_y^3)\sigma_y)$, combines with the Hamiltonian in Eq. 3.9. Then the current induced spin phenomena is found to depend on the relative values of ζ_1 and ζ_2. Consequently, the orientation of the induced spin polarization rotates for a specific applied field direction, similar to the case of the linear-in-k Rashba-Dresselhaus Hamiltonian. The orientation of the induced spin polarization vector is illustrated in Fig. 3.6(e) for a constant electric field direction $\mathbf{E} = (E_x, 0, 0)$.

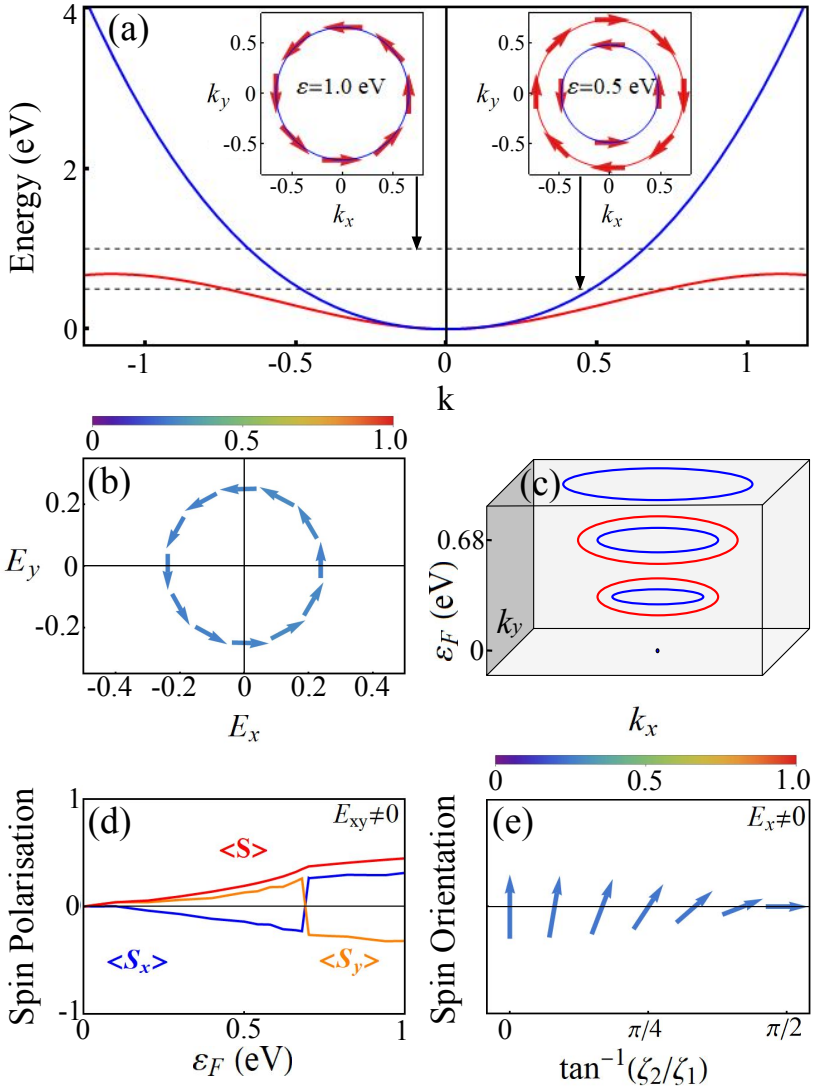

Figure 3.6: (a) Low-energy band spectrum of Eq. (3.9). The insets show spin orientations along the FCs at two different energies $\epsilon_F = 1.0$ eV and 0.5 eV, respectively. (b) Spin polarization per unit area in the E_x-E_y plane. Clearly, it is transverse to the applied field similar to standard REE. (c) and (d) Variation in the shape of FCs and spin polarization with ε_F, respectively. Evidently, the polarization enhances with the Fermi energy as opposed to standard RSOC term. (e) The orientation of induced spin polarization as a function of relative strength between cubic RSOC and cubic DSOC under C_3 symmetry.

It varies depending on their relative strengths defined by $\tan^{-1}(\zeta_2/\zeta_1)$. The induced polarization vector continues to rotate from Rashba-type ($\perp$ **E**) to Dresselhaus-type ($||$ **E**), reflecting the interplay between RSOC and DSOC.

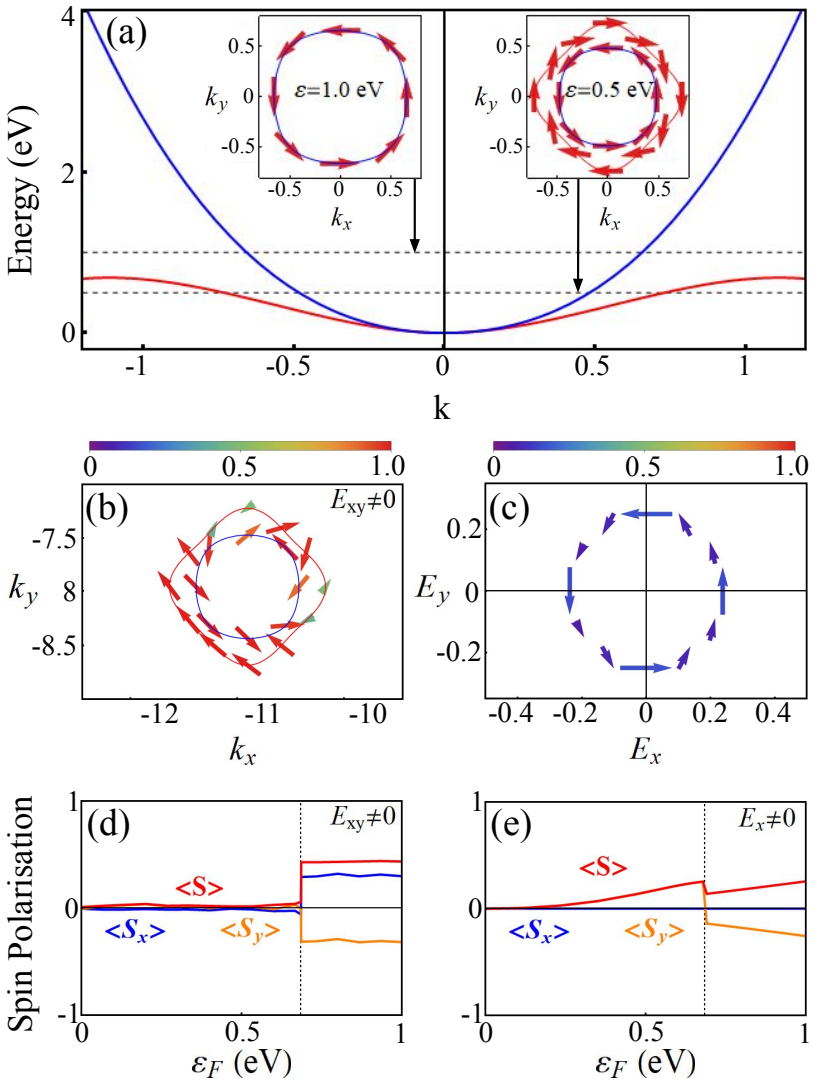

Figure 3.7: (a) The energy dispersion and spin orientations along the FCs of constant energy $\varepsilon_F = 0.5$ and 1.0 eV, respectively (in the inset) for pure-k^3 RSOC term under C_{4v} symmetry. (b) Snapshot of orientations of spins when electric field applied along xy-direction. (c) Resultant time and momentum averaged spin polarization as a function of electric field in the E_x-E_y plane for both the FCs at $\varepsilon_F = 0.5$ eV. (d, e) Spin polarization as a function of ε_F for the electric field along xy- and x-direction, respectively. The vertical line refers to the ($\varepsilon_F = 0.685$ eV) at which we see two FCs to a single FC transition.

3.3.2.2 Cubic terms associated with C_{4v} and C_4 symmetries

We next move to another class of point groups, *i.e.*, C_{4v} and C_4, considering a quantum well geometry of 2DEG. For C_{4v}, only the Rashba splitting is expected, with the allowed cubic-in-k RSOC terms being $\lambda_1(k_x^3\sigma_y - k_y^3\sigma_x)$ and $\gamma_1(k_x^2 k_y\sigma_x - k_x k_y^2\sigma_y)$, representing pure-$k^3$ and mixed-k^3 terms, respectively [101]. This higher-order RSOC often characterizes the Hamiltonian of surface

states in diamond and zinc-blende quantum wells oriented along the [001] direction [145]. The eigenvalues corresponding to the pure-k^3 and mixed-k^3 SOC are given by $E_{\pm}=\frac{\hbar^2k^2}{2m} \pm \lambda_1\sqrt{k_x^6+k_y^6}$ and $E_{\pm}=\frac{\hbar^2k^2}{2m}\pm\gamma_1 k k_x k_y$, respectively. Fig. 3.7(a) and Fig. 3.8(a) show the respective energy dispersion and k-dependent pseudospins on FCs (in the insets) at zero electric fields. The fourfold warping of FCs at low energy is evident in both cases. As before, the non-linear SOC terms involving λ_1 and γ_1 result in in-plane effective magnetic fields $\mathbf{B}_{\text{eff}}$ given by $\lambda_1(k^3/4)(-3\sin\delta+\sin 3\delta,\ 3\cos\delta+\cos 3\delta)$ and $\gamma_1(k^3/4)(\sin\delta+\sin 3\delta, -\cos\delta+\cos 3\delta)$, respectively. Concomitantly, the spin splittings exhibit a dependence on δ, resulting in anisotropic spin orientation along the FCs as evident from the insets of Fig. 3.7(a) and Fig. 3.8(a). This is in contrast to the C_{3v} case. Accordingly, the response to the electric field in a 2DEG with C_{4v} symmetry shows contrasting effects. Fig. 3.7(c) depicts the induced spin polarization which exhibits anisotropic behavior, with the maximum value occurring along the longitudinal direction of the applied field. In Fig. 3.7(d), for the in-plane electric field along xy direction, we observe that the polarization appears to be zero below $\varepsilon \approx 0.685$ eV due to cancellation from contributions of the two constant energy cuts. Above that energy value, a single FC exists, and it governs a finite net polarization as shown on the right side of the vertical dashed line in Fig. 3.7(d). For an electric field along x, the polarization gradually increases until $\varepsilon \approx 0.685$ eV, and a sudden jump in its magnitude at this point can be attributed to the single FC. Following the increase in ε_{F}, the polarization magnitude grows gradually. The difference in direction-dependent induced spin polarization behavior is the consequence of the deformed nature of the FCs; accordingly, the spins oriented perpendicular to the applied field are more responsive than the spins aligned in any other direction. Interestingly, the mixed-k^3 term does not exhibit any generation of spin polarization even with varying ε_{F} (see Fig. 3.8(d) and (e)). This absence of induced polarization retains regardless of the direction of the applied electric field (Fig. 3.8(c)).

The DSOC terms for C_4 point group, $\lambda_2(k_x^3\sigma_x+k_y^3\sigma_y)$ and $\gamma_2(k_xk_y^2\sigma_x+k_x^2k_y\sigma_y)$ [101], maintain the warping effect, while the ST changes based on the relative strengths of the λ_2 and γ_2 parameters. The induced spin polarization in these cases also rotates depending on the direction of the applied field, which is influenced by the ratio between the RSOC and DSOC parameters. Particularly, these terms correspond to DSOC(+), and similarly, one can identify associated DSOC(−) terms,

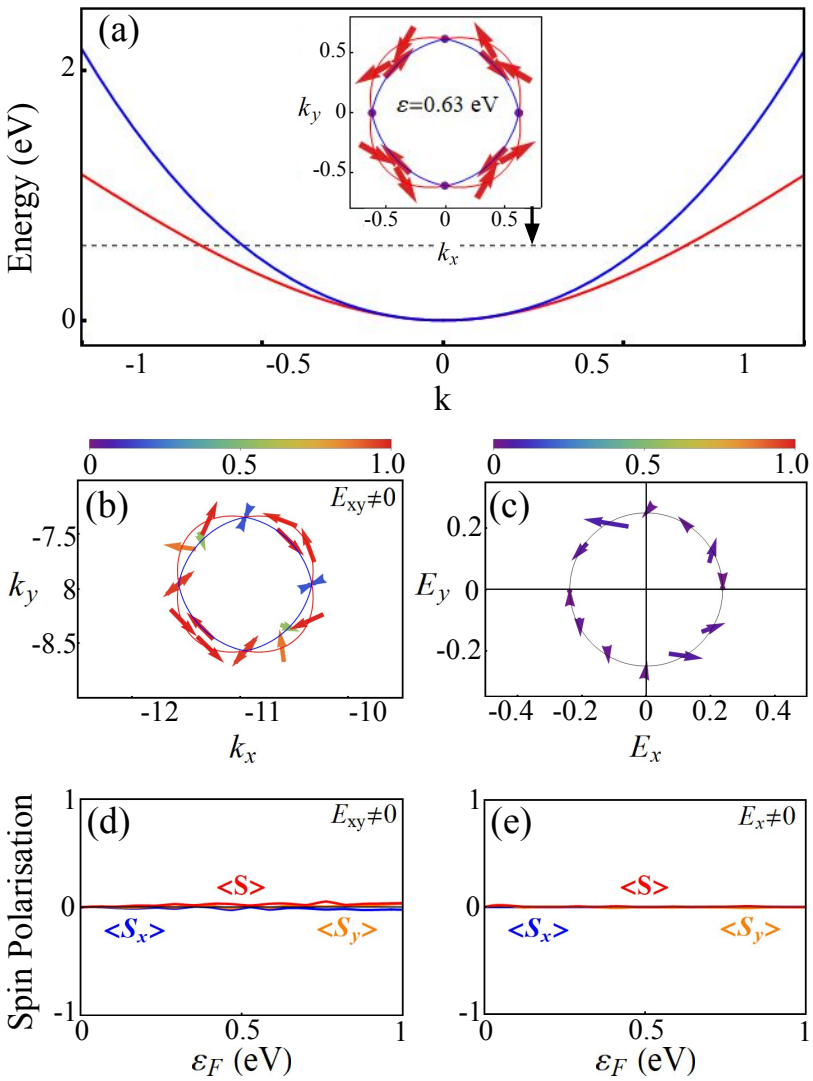

Figure 3.8: (a) The energy dispersion and spin orientations along the FCs of constant energy $\varepsilon_F = 0.6$ eV (inset) for the allowed mixed-k^3 RSOC term, $\gamma_1(k_x^2 k_y \sigma_x - k_x k_y^2 \sigma_y)$, under C_{4v} symmetry. b) The snapshot of the spin polarization in the k_x-k_y plane when the electric field is applied diagonally, the xy-direction. c) The electric field direction dependency of the spin polarization in E_x-E_y plane (at constant energy $\varepsilon_F = 0.63$ eV). (d, e) Spin polarization with ε_F for the field applied diagonally along xy- and x-direction, respectively.

analogous to the linear-in-k scenario. It is worth noting that in the pure cubic case, equal strengths of RSOC and DSOC(−) indeed result in PST generation. This is attributed to the wavefunctions becoming independent of momentum, leading to the pseudospin orientations in STs no longer being dependent on the momentum vector. Therefore, this PST phenomenon is once again observed to be unaffected by the applied field in the time-dependent dynamics, resulting in a net zero-induced spin magnetization. Moreover, similar to the Hamiltonian in Eq. 3.8, the precise tuning of RSOC and

DSOC(−) parameters dictates the overall magnitude of the spin polarization.

3.4 Summary and outlook

We have investigated current-induced spin polarization, namely the REE effect in 2DEG setup of quantum well geometry, considering all possible linear and nonlinear k-dependent Rashba and Dresselhaus SOC terms under various point group symmetries: C_3, C_{3v}, C_4, C_{4v}. Possible practical realization can be obtained in non-magnetic noncentrosymmetric bulk and surface/interface materials. Our findings can be summarised as follows: (i) While linear RSOC under C_{3v} or C_{4v} leads to standard REE, the presence of additional linear DSOC due to BIA under C_3 or C_4 symmetry leads to distinct features in spin polarization. In particular, we identify that two symmetry-allowed linear DSOC terms, DSOC(+) and DSOC(−), have adverse effects on the ST of FCs due to the phase difference in their wavefunctions. These features of STs are manifested in the spin polarization in the presence of an external field when they are considered individually with the linear RSOC. While RSOC and DSOC(+) lead to finite spin polarization irrespective of the relative strengths between them, the spin polarization for RSOC and DSOC(−) together vanishes when they are equal in strength, leading to persistent spin texture. Additionally, for DSOC(+) together with RSOC, the spin polarization remains constant, irrespective of the field direction. In contrast, for the case of DSOC(−), the magnitude of spin polarization varies with the field direction. In all these cases, we find the spin polarization to reduce as we increase ε_F. (ii) For nonlinear case, both C_{3v} and C_{4v} allows purely cubic RSOC. Accordingly, we obtain transverse spin polarization similar to standard REE. However, the magnitude of spin polarization turns out to vary with the direction of the applied field for C_{4v} in contrast to the C_{3v} case. This fact can be used as a diagnostic measure of the underlying symmetry of metallic surfaces of 2DEG. Additionally, we find that the C_{4v} allows mixed-cubic RSOC, but the spin polarization, in this case, turns out to be negligibly small due to the deformed FCs. (iii) We further find notable distinctions between linear and cubic RSOC in their spin polarization. While the spin polarization reduces as we increase ε_F for linear RSOC, the cubic RSOC does the opposite due to the presence of a single FC at higher energies. We note that many of these

interesting current-induced spin polarization phenomena between linear and nonlinear RSOC and DSOC have been previously overlooked. Our detailed analyses highlight the intricate and tunable nature of spin polarization in systems with combined RSOC and DSOC, offering new insights into spintronic applications.

The idea developed here can be useful for current-induced orbital polarization, namely the orbital Edelstein effect. Generally, orbital polarization is subdominant than the spin polarization [151]. However, different Rashba and Dresselhaus parameters can enhance orbital polarization. In particular, for mixed-k^3 Rashba, the system may exhibit only orbital polarization as the spin polarization is negligibly small. Further, the interplay between Rashba and Dresselhaus is expected to behave differently depending on the orbital coupling.

Chapter 4

Theoretical aspects of nonlinear Hall effects

In the previous chapters, we have focused on electrically driven spin responses, particularly the current-induced spin polarization in nonmagnetic systems with spin–orbit coupling. Beyond spin transport, electrically driven charge transport in such time-reversal symmetric systems also exhibits rich nonequilibrium phenomena that extend beyond the conventional linear response regime. In this context, recent developments have highlighted the important role of quantum geometric properties of electronic bands in governing nonlinear transport phenomena. Among these, nonlinear Hall effects have emerged as an important direction in which a transverse current arises at higher orders in the applied electric field.

In the linear response regime, the transverse Hall response is governed by the Berry curvature, which contributes an anomalous velocity to the semiclassical dynamics of electrons. However, in time-reversal symmetric systems, the net Berry curvature vanishes, thereby suppressing the linear anomalous Hall response. In such cases, a Hall response can still arise at higher orders in the applied electric field, originating from higher-order moments and field-induced corrections of geometric quantities, providing a fundamentally new mechanism for charge transport.

Motivated by these considerations, in this chapter, we develop a systematic theoretical framework to describe such quantum-geometric quantities and their associated nonlinear Hall responses. We begin by introducing the concept of adiabatic evolution and the Berry phase, emphasizing its geometric origin in parameter space. Building on this, we define the Berry curvature and discuss its

role in modifying the semiclassical dynamics of Bloch electrons, leading to the notion of anomalous velocity and the intrinsic anomalous Hall effect (AHE).

Next, we extend the discussion beyond linear response and introduce the nonlinear Hall effect within the semiclassical Boltzmann transport framework. In this context, we show how the second-order Hall response arises from the Berry curvature dipole (BCD), defined as the first-order moment of the Berry curvature in momentum space in systems with broken inversion symmetry. Furthermore, we discuss how even in systems preserving both time-reversal and inversion symmetries, higher-order responses can arise through another quantum geometric quantity known as the Berry connection polarizability (BCP), giving rise to a third-order Hall effect.

Through this framework, we establish a unified theoretical description that connects symmetry and quantum geometry to nonlinear charge transport. This provides the essential foundation for analyzing the nonlinear Hall responses in various systems discussed in the subsequent chapters of this thesis.

4.0.1 Adiabatic evolution and Berry phase

In a cyclic adiabatic evolution, the Hamiltonian depends on slowly varying parameters, and the system returns to its initial state if there is no energy degeneracy. However, the wavefunction acquires a phase during this evolution. One part of this phase is the dynamical phase, which depends on the time integral of the energy, and another part is known as the Berry phase. The Berry phase is also known as the geometric phase, as it arises from the geometry of the parameter space [31, 32, 152].

To elucidate the origin of the Berry phase, we consider a quantum system characterized by a Hamiltonian $H(\mathbf{R})$ that depends on a set of external parameters $\boldsymbol{R} = (R_1, R_2, \ldots)$. We consider the adiabatic evolution of the system in which the parameters $\mathbf{R}(t)$ vary slowly and follow a path C in the parameter space. To describe this evolution at each point along this path, it is convenient to use the instantaneous eigenstates of the Hamiltonian $H(\mathbf{R})$, which form an orthonormal basis and satisfy

$$H(\boldsymbol{R})\,|n(\boldsymbol{R})\rangle = \varepsilon_n(\boldsymbol{R})\,|n(\boldsymbol{R})\rangle\,. \tag{4.1}$$

Assume that the system is initially in a state $|n(\boldsymbol{R}(0))\rangle$. According to the adiabatic theorem, if the parameters change slowly enough, the system remains in the corresponding instantaneous eigenstate during the evolution. However, the wavefunction can acquire a phase factor. Therefore, the state of the system can be written as

$$|\psi(t)\rangle = e^{-i\theta(t)} |n(\boldsymbol{R}(t))\rangle . \tag{4.2}$$

The phase $\theta(t)$ can be determined from the time-dependent Schrödinger equation

$$H(\boldsymbol{R}(t)) |\psi(t)\rangle = i\hbar \frac{d}{dt} |\psi(t)\rangle . \tag{4.3}$$

Substituting Eq. 4.2 in the above expression and solving it, the total phase accumulated during the evolution is obtained as

$$\theta(t) = \frac{1}{\hbar} \int_0^t \varepsilon_n(\boldsymbol{R}(t'))dt' - i \int_0^t \langle n(\boldsymbol{R}(t'))| \frac{d}{dt'} |n(\boldsymbol{R}(t'))\rangle \, dt'. \tag{4.4}$$

Here the first term represents the dynamical phase, which depends on the energy. The second term corresponds to the *Berry phase*

$$\gamma_n = i \int_0^t \langle n(\boldsymbol{R}(t'))| \frac{d}{dt'} |n(\boldsymbol{R}(t'))\rangle \, dt'. \tag{4.5}$$

This phase appears because the eigenstates at time t and t+dt are not identical. It is often convenient to express the Berry phase in terms of the parameters $\mathbf{R}$ and can be rewritten as

$$\gamma_n = \oint_C d\boldsymbol{R} \cdot \boldsymbol{A}_n(\boldsymbol{R}), \tag{4.6}$$

where the *Berry connection* $\boldsymbol{A}_n(\boldsymbol{R})$ is defined as

$$\boldsymbol{A}_n(\boldsymbol{R}) = i \langle n(\boldsymbol{R})| \boldsymbol{\nabla}_{\boldsymbol{R}} |n(\boldsymbol{R})\rangle . \tag{4.7}$$

Note that the Berry phase γ_n is gauge independent and a real phase, even though it has an imaginary

sign in front of it, because $\langle n(\boldsymbol{R})|\, \boldsymbol{\nabla}_{\boldsymbol{R}}\, |n(\boldsymbol{R})\rangle$ is itself imaginary. The Berry connection $\boldsymbol{A}_n(\boldsymbol{R})$ is gauge-dependent quantity. Under a gauge transformation,

$$|n(\boldsymbol{R})\rangle \rightarrow e^{i\zeta(\boldsymbol{R})}\, |n(\boldsymbol{R})\rangle\,, \tag{4.8}$$

where $\zeta(\boldsymbol{R})$ is a smooth and single-valued function, the Berry connection transforms as,

$$\boldsymbol{A}_n(\boldsymbol{R}) \rightarrow \boldsymbol{A}_n(\boldsymbol{R}) - \frac{\partial}{\partial \boldsymbol{R}}\zeta(\boldsymbol{R}). \tag{4.9}$$

Then the Berry phase γ_n will be changed by,

$$-\oint_C \frac{\partial}{\partial \boldsymbol{R}}\zeta(\boldsymbol{R}).d\boldsymbol{R} = \zeta(\boldsymbol{R}(0)) - \zeta(\boldsymbol{R}(T)) \tag{4.10}$$

where T is the time after which the path C has been completed. For a closed path in parameter space, the system returns to the same physical configuration, i.e., $\boldsymbol{R}(0) = \boldsymbol{R}(T)$. Since the eigenstate must remain single-valued, when we return to the original parameter configuration, the state must be the same: $|n(\boldsymbol{R}(T))\rangle = |n(\boldsymbol{R}(0))\rangle$. Hence, the Berry phase can change only by

$$\zeta(\boldsymbol{R}(T)) - \zeta(\boldsymbol{R}(0)) = 2\pi \times integer. \tag{4.11}$$

Therefore, the Berry phase depends only on the geometry of the path in parameter space and cannot be removed completely. Hence, it is called a geometric phase.

4.0.2 Berry curvature

The Berry phase introduced in the previous section is defined for a closed path in parameter space. However, it is often useful to describe this geometric phase in terms of a local quantity defined at each point of the parameter space. This quantity is known as the *Berry curvature*.

Starting from the expression of the Berry phase in Eq. 4.6 accumulated along a closed loop C in parameter space, Stokes' theorem allows the line integral to be rewritten as a surface integral over a

surface $\mathcal{S}$ bounded by C,

$$\begin{aligned}\gamma_n &= \oint_C d\boldsymbol{R} \cdot \mathbf{A}_n(\mathbf{R}) \\ &= \int_{\mathcal{S}} d\boldsymbol{S} \cdot (\boldsymbol{\nabla}_{\boldsymbol{R}} \times \mathbf{A}_n(\mathbf{R})) \\ &= i \int_{\mathcal{S}} d\boldsymbol{S} \cdot (\langle \boldsymbol{\nabla} n(\boldsymbol{R})| \times |\boldsymbol{\nabla} n(\boldsymbol{R})\rangle) \,. \end{aligned} \tag{4.12}$$

The quantity inside the surface integral defines the *Berry curvature*,

$$\boldsymbol{\Omega}_n(\boldsymbol{R}) = \boldsymbol{\nabla}_{\boldsymbol{R}} \times \mathbf{A}_n(\mathbf{R}) = i \, \langle \boldsymbol{\nabla}_{\boldsymbol{R}} n(\boldsymbol{R})| \times |\boldsymbol{\nabla}_{\boldsymbol{R}} n(\boldsymbol{R})\rangle \,. \tag{4.13}$$

Thus, the Berry phase can be interpreted as the flux of the Berry curvature through the surface $\mathcal{S}$,

$$\gamma_n = \int_{\mathcal{S}} d\boldsymbol{S} \cdot \boldsymbol{\Omega}_n(\boldsymbol{R}). \tag{4.14}$$

In analogy with electrodynamics, it can be written as a gauge field tensor as,

$$\begin{aligned}\Omega^n_{\mu\nu}(\boldsymbol{R}) &= \frac{\partial A^n_\nu(\boldsymbol{R})}{\partial R^\mu} - \frac{\partial A^n_\mu(\boldsymbol{R})}{\partial R^\nu} \\ &= i\Big[\langle \frac{\partial n(\boldsymbol{R})}{\partial R^\mu} | \frac{\partial n(\boldsymbol{R})}{\partial R^\nu} \rangle - (\nu \longleftrightarrow \mu)\Big] \end{aligned} \tag{4.15}$$

which is an antisymmetric tensor under the exchange of the indices μ and ν. To obtain a more practical expression for the Berry curvature, we use the completeness relation of the eigenstates, $\sum_m |m\rangle\langle m| = 1$. This allows the Berry curvature to be written as

$$\Omega^n_{jk} = i \sum_{m \neq n} \epsilon_{ijk} \langle \nabla_j n|m\rangle\langle m|\nabla_k n\rangle. \tag{4.16}$$

The derivatives acting on the eigenstates can be further eliminated by differentiating the eigenvalue equation $H|n\rangle = \varepsilon_n|n\rangle$. Taking the gradient and projecting onto another eigenstate $\langle m|$ gives

$$(\varepsilon_n - \varepsilon_m)\langle m|\nabla n\rangle = \langle m|(\nabla H)|n\rangle. \tag{4.17}$$

Since $\langle m|n\rangle = 0$ for $m \neq n$, we obtain

$$\langle m|\nabla n\rangle = \frac{\langle m|(\nabla H)|n\rangle}{\varepsilon_n - \varepsilon_m}. \tag{4.18}$$

Substituting this relation into the previous expression 4.16 yields a useful formula for the Berry curvature,

$$\boldsymbol{\Omega}_n(\boldsymbol{R}) = i \sum_{m\neq n} \frac{\langle n|\boldsymbol{\nabla}_{\boldsymbol{R}} H|m\rangle \times \langle m|\boldsymbol{\nabla}_{\boldsymbol{R}} H|n\rangle}{(\varepsilon_n - \varepsilon_m)^2}. \tag{4.19}$$

This representation is particularly convenient because it does not involve derivatives of the wave functions explicitly and is therefore independent of the gauge choice of the eigenstates. This form shows that the Berry curvature arises from coupling between different energy bands and provides a local description of the geometric properties of the parameter space.

In the above discussion, we have discussed the basic concepts of the Berry phase and Berry curvature in a general system described by a parameter-dependent Hamiltonian $H(\mathbf{R})$. In crystalline solids, the parameters are replaced by the crystal momentum $\mathbf{k}$. The eigenstates of the Hamiltonian become Bloch states $|u_n(\mathbf{k})\rangle$, which depend on the momentum in the Brillouin zone. Therefore, the Berry connection for the nth band in momentum space is given by

$$\boldsymbol{A}_n(\boldsymbol{k}) = i \langle u_n(\boldsymbol{k})| \boldsymbol{\nabla}_{\boldsymbol{k}} |u_n(\boldsymbol{k})\rangle , \tag{4.20}$$

and the corresponding Berry curvature is

$$\boldsymbol{\Omega}_n(\boldsymbol{k}) = \boldsymbol{\nabla}_{\boldsymbol{k}} \times \mathbf{A}_n(\mathbf{k}). \tag{4.21}$$

4.0.3 Semiclassical dynamics of Bloch electrons and anomalous velocity

The Berry curvature discussed in the previous section has important consequences for the semiclassical motion of electrons in crystals. To understand its physical implications, it is necessary to examine how the Bloch states and the corresponding group velocity of electrons are influenced during an adiabatic evolution. We consider a Bloch electron subjected to a slowly varying perturbation, which

makes the Hamiltonian time dependent $H(\mathbf{k}, t)$. In this adiabatic limit, the first-order correction to the instantaneous eigenstate become

$$|u_m(\mathbf{k}, t)\rangle = |u_m(\mathbf{k})\rangle - i\hbar \sum_{n \neq m} \frac{|u_n(\mathbf{k})\rangle\langle u_n(\mathbf{k})|\partial_t u_m(\mathbf{k}, t)\rangle}{\varepsilon_m - \varepsilon_n}, \tag{4.22}$$

where $|u_m(\mathbf{k})\rangle = |u_m(\mathbf{k}, 0)\rangle$ and (m, n) are band indices. With this corrected eigenstate, we can now determine how the electron velocity is modified during the adiabatic evolution. Taking the expectation value of the velocity operator $v(\mathbf{k}) = \partial H/\partial(\hbar k)$ with this eigenstate, leads to a modified expression for the electron velocity (see the appendix B for detailed calculation) as

$$\mathbf{v}_m(\mathbf{k}) = \frac{1}{\hbar}\nabla_{\mathbf{k}}\varepsilon_m(\mathbf{k}) - i\left[\langle\nabla_{\mathbf{k}} u_m|\partial_t u_m\rangle - \langle\partial_t u_m|\nabla_{\mathbf{k}} u_m\rangle\right]. \tag{4.23}$$

The first term corresponds to the usual band velocity obtained from the dispersion relation, while the second term originates from the geometric structure of the Bloch wave functions. The second term can be identified as the Berry curvature component defined (following Eq. 4.15) in an extended parameter space consisting of the momentum and time variables. Therefore, the Eq. 4.23 can be written as

$$\mathbf{v}_m(\mathbf{k}) = \frac{1}{\hbar}\nabla_{\mathbf{k}}\varepsilon_m(\mathbf{k}) - \mathbf{\Omega}^m_{\mathbf{k}t}. \tag{4.24}$$

This result shows that the semiclassical dynamics of electrons are influenced not only by the band energy but also by the Berry curvature associated with the Bloch states.

To determine the explicit form of this correction in the presence of an weak electric field, it is convenient to introduce a time-dependent vector potential $\mathbf{A}(t)$ such that the electric field $\mathbf{E}(t) = -\partial\mathbf{A}(t)/\partial t$. Using the minimal coupling prescription described in Eq. 2.9, the crystal momentum is shifted as $\mathbf{k} \longrightarrow \mathbf{k} + \frac{e}{\hbar}\mathbf{A}(t)$. Taking the time derivative of this relation gives

$$\dot{\mathbf{k}} = -\frac{e}{\hbar}\mathbf{E}. \tag{4.25}$$

Substituting this relation into $\partial/\partial t = \dot{\mathbf{k}}_\alpha \partial/\partial k_\alpha = -(\frac{e}{\hbar})E_\alpha(\partial/\partial k_\alpha)$, the velocity expression in

Eq. 4.24 becomes

$$\mathbf{v}_m(\mathbf{k}) = \frac{1}{\hbar}\nabla_{\mathbf{k}}\varepsilon_m(\mathbf{k}) - \frac{e}{\hbar}\mathbf{E}\times\mathbf{\Omega}_m(\mathbf{k}), \tag{4.26}$$

where $\mathbf{\Omega}_m(\mathbf{k})$ is the Berry curvature of the m-th band. The second term in the above equation represents an additional contribution to the electron velocity known as the *anomalous velocity*, which originates entirely from the geometric properties of the Bloch wave functions.

4.0.4 Anomalous Hall effect

The anomalous velocity obtained in the previous section leads to a transverse charge current in the presence of an electric field. Since the anomalous velocity term is perpendicular to the applied electric field, it causes electrons to acquire a sideways motion in momentum space. Upon integrating the contributions from all occupied states over the Brillouin zone, the resulting transverse motion gives rise to a Hall current without requiring any external magnetic field. This effect is referred to as the intrinsic anomalous Hall effect.

Within the semiclassical framework, the electric current density is obtained by summing the velocity of all occupied Bloch states,

$$\mathbf{j} = -e\sum_n \int \frac{d^d\mathbf{k}}{(2\pi)^d} f_n(\mathbf{k})\,\mathbf{v}_n(\mathbf{k}), \tag{4.27}$$

where $f_n(\mathbf{k})$ is the Fermi–Dirac distribution function, n is the band index, and d presents the dimensionality of the system. Substituting the velocity derived in Eq. 4.26, the current density becomes

$$\mathbf{j} = -\frac{e}{\hbar}\sum_n \int \frac{d^d k}{(2\pi)^d} f_n(\mathbf{k})\,\nabla_{\mathbf{k}}\varepsilon_n(\mathbf{k}) + \frac{e^2}{\hbar}\sum_n \int \frac{d^d k}{(2\pi)^d} f_n(\mathbf{k})\,\mathbf{E}\times\mathbf{\Omega}_n(\mathbf{k}). \tag{4.28}$$

The first term corresponds to the conventional band current density, which vanishes in equilibrium and contributes to the longitudinal drift current under an applied electric field. The second term arises from the anomalous velocity associated with the Berry curvature, which is oriented perpendicular

to the applied electric field. Consequently, it leads to the intrinsic anomalous Hall current density,

$$\mathbf{j}_{\mathrm{AHE}} = \frac{e^2}{\hbar} \sum_n \int \frac{d^d\mathbf{k}}{(2\pi)^d} f_n(\mathbf{k})\, \mathbf{E} \times \mathbf{\Omega}_n(\mathbf{k}). \tag{4.29}$$

Here, the Berry curvature of the Bloch bands acts as an effective magnetic field that deflects the motion of electrons and produces this transverse current. The above expression shows that the anomalous velocity generates a current proportional to the applied electric field and can be expressed as $\mathbf{j} = \boldsymbol{\sigma}\mathbf{E}$, where the coefficient relating the current to the electric field defines the anomalous Hall conductivity and can be written in component form as

$$\sigma_{ab} = -\frac{e^2}{\hbar} \sum_n \int \frac{d^d\mathbf{k}}{(2\pi)^d} f_n(\mathbf{k})\, \Omega_n^c(\mathbf{k})\, \epsilon_{abc}, \tag{4.30}$$

where ϵ_{abc} is the Levi–Civita tensor and $(a, b, c) = (x, y, z)$.

An important situation arises in insulating systems where the Fermi level lies within an energy gap, and the Hall conductivity is determined entirely by the Berry curvature of the occupied bands. For instance, in two-dimensional systems, the electronic motion is confined to the xy plane, and only the out-of-plane component of the Berry curvature (Ω^Z) contributes to the Hall response. The corresponding Hall conductivity becomes

$$\sigma_{xy} = -\frac{e^2}{\hbar} \sum_n \int_{\mathrm{BZ}} \frac{d^2\mathbf{k}}{(2\pi)^2}\, \Omega_n^z(\mathbf{k}). \tag{4.31}$$

The integral of the Berry curvature over the Brillouin zone is quantized and defines an integer topological invariant known as the *Chern number*,

$$C = \frac{1}{2\pi} \sum_n \int_{\mathrm{BZ}} d^2\mathbf{k}\, \Omega_n^z(\mathbf{k}). \tag{4.32}$$

This quantized Hall response reflects the topological nature of the electronic band structure and leads to the quantum anomalous Hall effect.

The existence of a finite anomalous Hall response is strongly constrained by symmetry. Under

time-reversal symmetry, the Berry curvature satisfies $\mathbf{\Omega}_n(\mathbf{k}) = -\mathbf{\Omega}_n(-\mathbf{k})$, whereas under spatial inversion symmetry, it transforms as $\mathbf{\Omega}_n(\mathbf{k}) = \mathbf{\Omega}_n(-\mathbf{k})$. Therefore, in the presence of time reversal symmetry, the integration of Berry curvature weighted by the equilibrium Fermi distribution function is forced to vanish in the Brillouin zone. Hence, a nonzero intrinsic anomalous Hall effect requires the breaking of time-reversal symmetry, which commonly occurs in ferromagnetic systems.

4.0.5 Nonlinear Hall effect

Interestingly, even in systems that preserve time-reversal symmetry, a transverse Hall response can still arise when the electron distribution is driven out of equilibrium by an external electric field. In this case, the electric field correction to the distribution function contributes to the Berry-curvature integral and produces a Hall current beyond the linear response regime. To describe this effect, it is necessary to consider the semiclassical Boltzmann transport theory. In the next section, we discuss this framework and show how it leads to the nonlinear Hall response in time-reversal symmetric systems.

4.0.5.1 Boltzmann transport theory

In this theoretical framework, the electronic system can be described by a distribution function $f_{\mathbf{k}}(\mathbf{r}, t)$, which characterizes the evolution of electrons in phase space and specifies the particle distribution within an infinitesimal volume element $d\mathbf{r}\, d\mathbf{k}$ around the point $(\mathbf{r}, \mathbf{k})$ at a given time.

After a small time interval dt, the electrons evolve to a different region of phase space $d\mathbf{r}'\, d\mathbf{k}'$, centered at the point $(\mathbf{r}', \mathbf{k}')$. If dissipative processes are neglected, the total number of particles must remain unchanged during this evolution. This requirement can be written as

$$f_{\mathbf{k}}(\mathbf{r}, t)\, d\mathbf{r}\, d\mathbf{k} = f_{\mathbf{k}'}(\mathbf{r}', t + dt)\, d\mathbf{r}'\, d\mathbf{k}'. \tag{4.33}$$

Liouville's theorem states that the phase-space volume is conserved during the time evolution of the system. Therefore the phase-space elements satisfy $d\mathbf{r}\, d\mathbf{k} = d\mathbf{r}'\, d\mathbf{k}'$, which implies that the value

of the distribution function remains constant along the trajectory of a particle in phase space,

$$f_{\mathbf{k}}(\mathbf{r}, t) = f_{\mathbf{k}'}(\mathbf{r}', t + dt). \tag{4.34}$$

Taking the time derivative of this condition leads to the continuity equation in phase space,

$$\frac{df_{\mathbf{k}}(\mathbf{r}, t)}{dt} \equiv \frac{\partial f_{\mathbf{k}}(\mathbf{r}, t)}{\partial t} + \dot{\mathbf{r}} \cdot \frac{\partial f_{\mathbf{k}}(\mathbf{r}, t)}{\partial \mathbf{r}} + \dot{\mathbf{k}} \cdot \frac{\partial f_{\mathbf{k}}(\mathbf{r}, t)}{\partial \mathbf{k}} = 0. \tag{4.35}$$

When the system is in thermal equilibrium, the carrier distribution is determined by the Fermi–Dirac function,

$$f_{\mathbf{k}}(\mathbf{r}, t)_{\text{eq}} = \frac{1}{e^{(\varepsilon_{\mathbf{k}} - \mu)/k_B T} + 1}. \tag{4.36}$$

However, in realistic materials, electrons undergo scattering processes due to impurities, phonons, or other interactions. These processes modify the distribution function and introduce an additional time dependence. Thus the rate of change of the distribution caused by scattering can be written as

$$\frac{df_{\mathbf{k}}(\mathbf{r}, t)}{dt} = \left(\frac{\partial f_{\mathbf{k}}(\mathbf{r}, t)}{\partial t} \right)_{\text{scatt}}. \tag{4.37}$$

By combining the phase-space continuity equation with the scattering term, we obtain the Boltzmann transport equation [7, 153],

$$\frac{\partial f_{\mathbf{k}}(\mathbf{r}, t)}{\partial t} + \dot{\mathbf{r}} \cdot \frac{\partial f_{\mathbf{k}}(\mathbf{r}, t)}{\partial \mathbf{r}} + \dot{\mathbf{k}} \cdot \frac{\partial f_{\mathbf{k}}(\mathbf{r}, t)}{\partial \mathbf{k}} = \left(\frac{\partial f_{\mathbf{k}}(\mathbf{r}, t)}{\partial t} \right)_{\text{scatt}}. \tag{4.38}$$

4.0.5.2 Berry curvature dipole and second-order Hall effect

Using the semiclassical Boltzmann framework discussed in the previous section, we now describe how a nonlinear Hall response can arise in systems that preserve time-reversal symmetry. For simplicity, we consider a single band and set $\hbar = 1$. With these assumptions, the expression for the

electric current density given in Eq. 4.27 can be written as

$$j_a = -e \int_k f(\mathbf{k}) v_a, \tag{4.39}$$

where $\int_k = d^d\mathbf{k}/(\mathbf{2}\pi)^{\mathbf{d}}$ and the velocity component v_a is given by anomalous velocity in eq. 4.26. Under the influence of an oscillating electric field $\boldsymbol{E}(t) = \mathrm{Re}\{\mathbf{E}e^{i\omega t}\}$ with frequency ω, the momentum shift become $\dot{\mathbf{k}} = -e\mathbf{E}(t)$ and the resulting change in the electron distribution can be described using the semiclassical Boltzmann equation. Since the characteristic length scale of the system is much larger than the average distance between scattering centers, the system can be treated as spatially uniform ($\partial f_{\mathbf{k}}(\mathbf{r}, t)/\partial \mathbf{r} = 0$). Furthermore, in the relaxation time approximation, which assumes that scattering drives the system toward the equilibrium distribution f_{eq}, the scattering term in Eq. 4.38 takes the form [7]

$$\left(\frac{\partial f}{\partial t}\right)_{\text{scatt}} = -\frac{(f - f_{eq})}{\tau}, \tag{4.40}$$

where τ is the relaxation time. Therefore, the Boltzmann equation in Eq. 4.38 reduces to

$$-e\tau E_a \partial_a f + \tau \partial_t f = f_{eq} - f, \tag{4.41}$$

where $\partial_a = \partial/\partial k_a$ and $\partial_t = \partial/\partial t$. To solve this equation and obtain the nonlinear response, we expand the distribution function up to second order in the electric field, $f = \mathrm{Re}(f_{eq} + f_1 + f_2)$. Substituting this function into Eq. 4.41, we find a recursive structure as follows (see appendix C for detaild derivation) [39]

$$\begin{aligned} f_1 &= f_1^{\omega} e^{i\omega t}, & f_1^{\omega} &= \frac{e\tau E_a \partial_a f_{eq}}{1 + i\omega\tau}, \\ f_2 &= f_2^0 + f_2^{2\omega} e^{2i\omega t} & f_2^0 &= \frac{(e\tau)^2 E_a^* E_b \partial_{ab} f_{eq}}{2(1 + i\omega\tau)}, \\ f_2^{2\omega} &= \frac{(e\tau)^2 E_a^* E_b^* \partial_{ab} f_{eq}}{2(1 + 2i\omega\tau)(1 + i\omega\tau)}. \end{aligned} \tag{4.42}$$

Using these expressions, the current density can be written as $j_a = \mathrm{Re}\left(j_a^0 + j_a^{2\omega} e^{2i\omega t}\right)$, with

$$\begin{aligned} j_a^0 &= \frac{e^2}{2}\int_k \epsilon_{abc}\Omega_b E_c^* f_1^\omega - e\int_k f_2^0 \partial_a E(\mathbf{k}), \\ j_a^{2\omega} &= \frac{e^2}{2}\int_k \epsilon_{abc}\Omega_b E_c f_1^\omega - e\int_k f_2^{2\omega} \partial_a E(\mathbf{k}). \end{aligned} \tag{4.43}$$

The first term in each expression originates from the anomalous velocity induced by the Berry curvature, whereas the second term arises from the conventional band velocity. For a constant relaxation time, the latter contributions vanish due to TRS. The remaining terms therefore describe a second-order Hall current governed by the Berry curvature. Therefore, the current density can be written in terms of a second-order Hall conductivity tensor ζ_{abc} as

$$j_a^0 = \zeta_{abc} E_b E_c^*, \qquad j_a^{2\omega} = \zeta_{abc} E_b E_c, \tag{4.44}$$

where

$$\zeta_{abc} = \epsilon_{abc}\frac{e^3\tau}{2(1+i\omega\tau)}\int_k (\partial_b f_{eq})\Omega_d. \tag{4.45}$$

Here the factor $\partial_b f_{eq}$ ensures that only electronic states near the Fermi surface contribute at low temperature. Furthermore, by integrating by parts, the conductivity can be rewritten as

$$\zeta_{abc} = -\epsilon_{abc}\frac{e^3\tau}{2(1+i\omega\tau)}\int_k f_{eq}(\partial_b \Omega_d). \tag{4.46}$$

This relation indicates that the second-order Hall conductivity is governed by the dipole moment of the Berry curvature in momentum space. This quantity is commonly known as the *Berry curvature dipole* and is defined as

$$D_{ab} = \int_k f_{eq}(\partial_a \Omega_b) = -\int_k \frac{\partial f_{eq}}{\partial \varepsilon} v_a \Omega_b. \tag{4.47}$$

Therefore, even when the Berry curvature itself integrates to zero due to time-reversal symmetry, its first order moment can remain finite in systems without inversion symmetry.

4.0.5.3 Berry connection polarizability and third-order Hall effect

In addition to the mechanisms discussed above, nonlinear Hall transport can also originate from other intrinsic geometric quantities. In this context, we introduce the Berry connection polarizability (BCP), a distinct geometric quantity that gives rise to a third-order Hall response. Notably, unlike the responses arising from the Berry curvature and the BCD, this BCP induced third-order Hall response is not constrained by either inversion or time-reversal symmetry.

Under the influence of an oscillating electric field, the perturbation to the system is described by $H' = e\mathbf{E}.\mathbf{r}$, which induces a position shift in the wave packet [45]. In the preceding discussion, only the field-induced correction to the distribution function was taken into account. Here, we additionally incorporate the field-induced modifications to both the band energy and the Berry curvature. Consequently, the semiclassical equations of motion (Eq. 4.26) can be written as (setting $e = \hbar = 1$) [154].

$$\dot{\mathbf{r}}(\mathbf{k}) = \nabla_{\mathbf{k}}\varepsilon^{c}(\mathbf{k}) - \mathbf{E} \times \mathbf{\Omega}^{c}(\mathbf{k}), \tag{4.48}$$

where ε^{c} and $\mathbf{\Omega}^{c}$ are the higher-order corrections to band energy and Berry curvature, respectively. They can be expressed as

$$\varepsilon^{c}(\mathbf{k}) = \sum_{i=0}^{2} \varepsilon^{(i)}(\mathbf{k}), \qquad \mathbf{\Omega}^{c}(\mathbf{k}) = \nabla_{\mathbf{k}} \times \sum_{i=0}^{1} \mathbf{A}^{(i)}(\mathbf{k}), \tag{4.49}$$

where $\mathbf{A}^{(i)}$ is the $i-$th order correction to the Berry connection. For the zeroth-order correction in energy and Berry curvature, the Hall current density derived from Eq. 4.39 is given by [155, 156]

$$j_{\alpha} = \sigma_{\alpha\beta}E_{\beta} + \zeta_{\alpha\beta\gamma}E_{\beta}E_{\gamma}, \tag{4.50}$$

where $(\alpha, \beta, \gamma, \delta) \in (x, y, z)$ are applied field directions, and the linear order ($\sigma_{\alpha\beta}$) and the second order ($\zeta_{\alpha\beta\gamma}$) Hall conductivity are already derived in Eq. 4.30 and 4.46 respectively.

To capture the third-order Hall effect, we include the second-order correction to the band energy because the first-order term is gauge-dependent and vanishes in the wave packet picture [45, 46]. We also incorporate the first-order correction to the Berry curvature. In the presence of the perturbation

H′, the first-order correction to the Bloch wavefunction is

$$|u_m^{(1)}(\mathbf{k})\rangle = \sum_{n\neq m} \frac{e\mathbf{E}.\mathbf{A}_{nm}^{(0)}(\mathbf{k})\,|u_n^{(0)}(\mathbf{k})\rangle}{\varepsilon_m^{(0)}(\mathbf{k}) - \varepsilon_n^{(0)}(\mathbf{k})}, \tag{4.51}$$

where $\mathbf{A}_{nm}^{(0)}(\mathbf{k}) = \langle u_m^{(0)}(\mathbf{k})|\, i\nabla_{\mathbf{k}}\, |u_n^{(0)}(\mathbf{k})\rangle$ is the zeroth-order interband Berry connection and m, n are the band indices. Then the first order correction in Berry curvature is $\mathbf{\Omega}^{(1)}(\mathbf{k}) = \nabla_{\mathbf{k}} \times \mathbf{A}^{(1)}(\mathbf{k})$, where the corresponding correction to the Berry connection $\mathbf{A}^{(1)}$ can be expressed as

$$A_{m,\alpha}^{(1)}(\mathbf{k}) = 2\,\mathrm{Re}\sum_{n\neq m} \frac{A_{mn,\alpha}^{(0)}(\mathbf{k})A_{nm,\beta}^{(0)}(\mathbf{k})}{\varepsilon_m^{(0)}(\mathbf{k}) - \varepsilon_n^{(0)}(\mathbf{k})} E_b = G_{m,\alpha\beta}E_\beta. \tag{4.52}$$

Here, we have introduced the second-rank tensor

$$G_{m,\alpha\beta} = 2\,\mathrm{Re}\sum_{n\neq m} \frac{A_{mn,\alpha}^{(0)}(\mathbf{k})A_{nm,\beta}^{(0)}(\mathbf{k})}{\varepsilon_m^{(0)}(\mathbf{k}) - \varepsilon_n^{(0)}(\mathbf{k})}, \tag{4.53}$$

referred to as the *Berry connection polarizability* tensor, also known as the band-normalised quantum metric. Moreover, the second-order correction to the band energy can be expressed in terms of this BCP tensor as follows:

$$\varepsilon_m^{(2)}(\mathbf{k}) = \sum_{n\neq m} \frac{|\,\langle u_m^{(0)}(\mathbf{k})|\, H'\, |u_n^{(0)}(\mathbf{k})\rangle\,|^2}{\varepsilon_m^{(0)}(\mathbf{k}) - \varepsilon_n^{(0)}(\mathbf{k})} = \frac{1}{2}G_{\alpha\beta}E_\alpha E_\beta. \tag{4.54}$$

Next, we proceed to determine the non-equilibrium distribution function by solving the semiclassical Boltzmann equation in a steady state situation under relaxation time approximation [7], which yields

$$\mathbf{k}.\nabla_{\mathbf{k}} f(\mathbf{k}) = \frac{f_{eq}(\mathbf{k}) - f(\mathbf{k})}{\tau}. \tag{4.55}$$

For the solution of equation (4.55), we consider the following ansatz:

$$f(\mathbf{k}) = \sum_{i=0}^{\infty} (\tau\mathbf{E}.\nabla_{\mathbf{k}})^i f_{eq}(\varepsilon^c(\mathbf{k})). \tag{4.56}$$

By substituting Eqs. (4.48) and (4.56) into the current density expression in Eq. (4.39), we obtain

the third-order current density as [44, 46, 157]

$$
\begin{aligned}
j^{(3)} = & \int_k (\mathbf{E}\times\mathbf{\Omega}^{(0)}(\mathbf{k}))\varepsilon^{(2)}(\mathbf{k})f'_{eq}(\mathbf{k}) - \tau\int_k \nabla_{\mathbf{k}}\varepsilon^{(0)}(\mathbf{k})(\mathbf{E}.\nabla_{\mathbf{k}})\varepsilon^{(2)}(\mathbf{k})f'_{eq}(\mathbf{k}) \\
& - \tau\int_k \nabla_{\mathbf{k}}\varepsilon^{(2)}(\mathbf{k})(\mathbf{E}.\nabla_{\mathbf{k}})f_{eq}(\mathbf{k}) + \tau\int_k (\mathbf{E}\times\mathbf{\Omega}^{(1)}(\mathbf{k}))(\mathbf{E}.\nabla_{\mathbf{k}})f_{eq}(\mathbf{k}) \\
& + \tau^2\int_k (\mathbf{E}\times\mathbf{\Omega}^{(0)}(\mathbf{k}))(\mathbf{E}.\nabla_{\mathbf{k}})^2 f_{eq}(\mathbf{k}) - \tau^3\int_k \nabla_{\mathbf{k}}\varepsilon^{(0)}(\mathbf{k})(\mathbf{E}.\nabla_{\mathbf{k}})^3 f_{eq}(\mathbf{k}).
\end{aligned} \tag{4.57}
$$

Since both the τ-independent and τ^2 terms in the right-hand side of equation 4.57 are odd under time-reversal symmetry, neither contributes to the current density. Therefore, only the τ and τ^3 terms contribute to the third-order current, with each term having a distinct physical origin. Specifically, the second term arises due to the second-order correction to the energy entering the distribution function. The third term is associated with the modification of the band velocity at second order in the applied field. The fourth contribution is linked to the anomalous velocity generated by the first-order field-induced correction to the Berry curvature. Finally, the term proportional to τ^3 originates from the combined effect of the band velocity and the gradient of the distribution function. Since we are interested in the Berry connection polarizability induced TOH current, we will only consider the terms proportional to τ. Finally, we can write the TOH current density as $j^{(3)}_\alpha = \chi_{\alpha\beta\gamma\delta}E_\beta E_\gamma E_\delta$, where the third-order Hall conductivity linear in τ upon simplification is given by

$$
\chi_{\alpha\beta\gamma\delta} = \tau\int_k (\partial_{k_\alpha}\partial_{k_\beta}G_{\gamma\delta} - \partial_{k_\alpha}\partial_{k_\delta}G_{\beta\gamma} + \partial_{k_\beta}\partial_{k_\delta}G_{\alpha\gamma})f_{eq}(\mathbf{k}) - \frac{\tau}{2}\int_k v_\alpha(\mathbf{k})v_\beta(\mathbf{k})G_{\gamma\delta}f''_{eq}(\mathbf{k}). \tag{4.58}
$$

Note that, the BCP tensor $G_{\alpha\beta}(\mathbf{k})$ is an even function in momentum under both time-reversal and inversion symmetries. As a result, unlike the Berry curvature and the BCD, it is not constrained by these symmetries and can yield a finite third-order Hall response even in systems that preserve both inversion and time-reversal symmetry.

Chapter 5

Persistent spin texture and nonlinear Hall responses

Following the theoretical framework for quantum-geometry-induced nonlinear Hall effects discussed in the previous chapter, we now investigate these phenomena in the Rashba–Dresselhaus system, particularly in the persistent spin texture (PST) regime introduced in chapter 3. In this regime, the system realizes special spin–orbit–coupled states in which the Bloch spinors become independent of momentum, resulting in a unidirectional spin configuration and a complete suppression of conventional field-induced spin responses. This motivates an examination of how charge transport behaves in this regime.

We begin by analyzing the Rashba–Dresselhaus system in detail, with particular emphasis on the PST regime, and discuss how the underlying symmetry constraints influence the electronic properties in this regime. We then introduce the relevant quantum geometric quantities and identify the Berry connection polarizability as the only non-vanishing conventional geometric quantity in this context, and examine its behavior both at the PST condition and in its vicinity. At the PST point, symmetry enforces its exact cancellation, resulting in the absence of the corresponding nonlinear Hall response. However, when the system is tuned close to this regime, the response becomes significantly enhanced. We show that this behavior is closely connected to the evolution of the band structure near the PST point, where nearly degenerate region appear and strongly influence the

nonlinear Hall response.

5.1 Introduction

The Rashba–Dresselhaus system has been widely studied as a prototypical platform for exploring spin–orbit–driven transport phenomena [121, 144, 158]. In chapter 3, we have shown that the interplay between these two linear in momentum SOC leads to rich spin textures and tunable spin dynamics in momentum space. Since the relative strengths of the Rashba and Dresselhaus interactions can be controlled experimentally through various techniques such as strain engineering [159], electrically controlled gate voltages [160], and asymmetric doping in quantum wells [161], this system provides an ideal platform for investigating electrically driven spin and charge transport phenomena.

A particularly intriguing regime emerges when the Rashba and Dresselhaus SOC strengths become equal. In this limit, the system hosts a special spin configuration known as the persistent spin texture [121, 122], which we have introduced in Sec. 3.3.1.2 of chapter 3. At this point, the system exhibits an emergent SU(2) symmetry, which renders the spinor part of the Bloch states independent of momentum and results in a unidirectional spin alignment in momentum space. As a consequence, spin relaxation is strongly suppressed, giving rise to long-lived spin states. Owing to these unusual properties, the PST regime has attracted considerable interest for potential spintronic applications [74, 162, 163].

While most of the previous studies on the Rashba–Dresselhaus system have focused on spin-related transport properties, much less attention has been paid to how the electronic band geometry in this system influences nonlinear charge transport. This aspect becomes particularly interesting in light of the complete suppression of current-induced spin polarization in the PST regime. In recent years, nonlinear electrical responses have become an important tool for probing the geometric properties of electronic bands in quantum materials. Particularly, the nonlinear Hall effect has attracted considerable interest because it can appear even in time-reversal-symmetric systems without requiring an external magnetic field. For instance, it has been theoretically shown that the second-order

nonlinear Hall response originates from the Berry curvature dipole (BCD) of Bloch electrons [164] in time-reversal-symmetric systems with broken IS. This prediction has been confirmed experimentally in several noncentrosymmetric materials such as WTe_2 [165, 166], demonstrating the important role of band geometry in nonlinear transport. Beyond the BCD mechanism, nonlinear responses can also arise from another important quantum-geometric quantity, known as the band-normalized quantum metric or Berry connection polarizability (BCP) [167]. Recent theoretical studies have shown that BCP can generate a third-order Hall response even in systems where the Berry curvature vanishes and it is not constrained by TRS and IS [44, 157, 168]. Such effects have also been experimentally observed in materials like the Weyl semimetal $TaIrTe_4$ [48].

Motivated by these developments, in this chapter we study the quantum-geometry-induced nonlinear Hall response in the Rashba–Dresselhaus system. By analyzing the band structure across different regimes of spin–orbit coupling strengths, we demonstrate that tuning the Rashba and Dresselhaus parameters modifies the nodal geometry of the bands, which in turn leads to qualitatively different momentum-space distributions of quantum geometric quantities. In particular, as the system approaches the PST regime, a nearly degenerate region with a single node emerges in the band structure, and at the exact PST point, it becomes a nodal line.

In the absence of an out-of-plane spin component (i.e., without a σ_z term), the electronic states remain confined to the plane, which leads to a vanishing Berry curvature and, consequently, a zero BCD. As a result, lower-order Hall responses are suppressed, and the BCP becomes the leading non-vanishing geometric contribution. Correspondingly, the nearly degenerate band structure strongly influences the distribution of the BCP tensor and results in a pronounced enhancement of the transverse third-order Hall conductivity near the PST regime, even though the response vanishes exactly at the PST point itself. Our results thus reveal a connection between nodal band geometry and nonlinear transport responses. Although a similar study was reported in Ref. [157], the origin of the differences in the geometric quantities and their connection to the underlying nodal band structure were not clearly addressed.

The rest of the chapter is organised as follows: In Sec. 5.2, we begin by introducing the Rashba–Dresselhaus system and discuss the emergence of the PST regime. In particular, we analyze

how varying the relative strengths of the Rashba and Dresselhaus SOC modifies the band structure and leads to distinct nodal geometries in momentum space. Building on this understanding, in Sec. 5.3 we evaluate the relevant quantum geometric quantities and compute the corresponding nonlinear Hall conductivity, highlighting how the evolution of the band structure influences the transport response. Finally, we summarize the main findings of this chapter in Sec. 5.4.

5.2 Rashba-Dresselhaus system and persistent spin texture

In this section, we present a detailed analysis of the linear Rashba -Dresselhaus system, especially the PST. The Hamiltonian of a two-dimensional electron gas with linear-in-momentum Rashba and Dresselhaus SOC can be written as

$$H = \frac{\hbar^2 k^2}{2m} + \mathbf{d}.\boldsymbol{\sigma}, \tag{5.1}$$

where the $\mathbf{d}$ vector components are given by $(d_x, d_y, d_z) = (\beta k_x - \alpha k_y, \alpha k_x - \beta k_y, 0)$, and $\boldsymbol{\sigma}$ denotes the Pauli spin matrices. Here, α and β represent the strengths of the Rashba and Dresselhaus SOC, respectively. The system preserves TRS ($\mathcal{T}$), while IS ($\mathcal{P}$) is broken. In this system, the effective spin-orbit field can be written as $\mathbf{B}_{\text{eff}} = [\beta k_x - \alpha k_y, \alpha k_x - \beta k_y]$ that depends on the direction of the momentum. This in turn produces anisotropic spin textures on the Fermi contours as depicted in the previous chapter in Sec. 3.3.1.2. The corresponding energy dispersion becomes

$$\varepsilon_{\pm} = \frac{k^2}{2m} \pm \sqrt{(\beta k_x - \alpha k_y)^2 + (\alpha k_x - \beta k_y)^2}, \tag{5.2}$$

where $\pm$ denotes the band indices. However, a completely different regime emerges when the Rashba and Dresselhaus SOC coupling strengths are equal in magnitude. While a generic spin–orbit–coupled system exhibits only a global $U(1)$ spin-rotation symmetry, at the PST point ($\alpha = \beta$) an exact $SU(2)$ symmetry emerges [121, 169]. This symmetry involves spin components at a finite wave vector and is fundamentally distinct from the conventional $U(1)$ symmetry of generic SOC systems [121, 170].

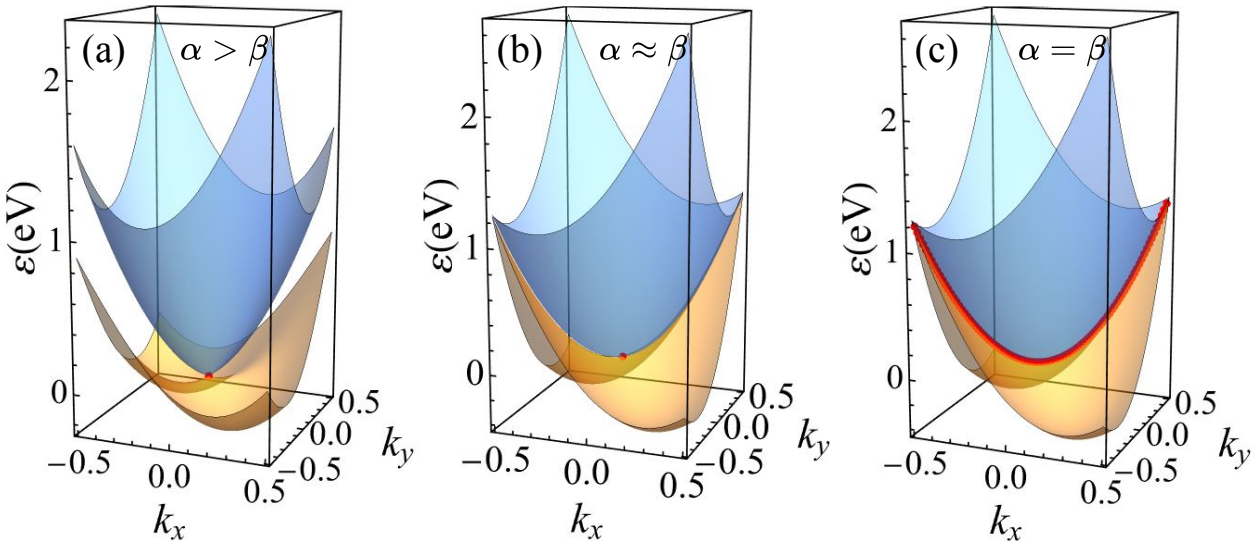

Figure 5.1: Energy dispersion of Rashba–Dresselhaus system for different SOC strengths. (a) to (c) presents the dispersion for the non-PST ($\alpha > \beta$), near PST ($\alpha \approx \beta$), and exact PST ($\alpha = \beta$) situation, respectively. Here, the red dots denote the number of band touching points for three situations, which depict their corresponding nodal geometry. Note that in the near-PST case (b), the two bands are nearly degenerate over a region of momentum space. The parameters used are (a) $\alpha = 1.0$ eV.Å, $\beta = 0.5$ eV.Å, (b) $\alpha = 1.0$ eV.Å, $\beta = 0.98$ eV.Å, and (c) $\alpha = \beta = 1.0$ eV.Å. Momentum k_x, k_y are in units of Å^{-1}.

At this point, the SOC term simplifies to

$$H_{\mathrm{SOC}}(\mathbf{k}) = \sqrt{2}\alpha(k_x - k_y)\Sigma, \tag{5.3}$$

where $\Sigma = (\sigma_x + \sigma_y)/\sqrt{2}$. Since Σ satisfies $[H(\mathbf{k}), \Sigma] = 0$, the Hamiltonian is diagonal in the eigenbasis of Σ [169]. Defining the eigenstates of Σ by $\Sigma\,|\chi_\zeta\rangle = \zeta\,|\chi_\zeta\rangle$, with $\zeta = \pm 1$, the Bloch eigenstates can be chosen to have a spinor part given by $|u^{\zeta}_{m\mathbf{k}}\rangle = |\chi_\zeta\rangle$, independent of $\mathbf{k}$. The corresponding eigenvalues are

$$E_\zeta(\mathbf{k}) = \frac{k^2}{2m} + \sqrt{2}\alpha\zeta|k_x - k_y|. \tag{5.4}$$

Consequently, the spin orientation on the Fermi contours becomes unidirectional, forming a PST.

In addition to exhibiting distinct spin textures, the system also displays interesting band geometries as the SOC parameters are tuned. In Fig. 5.1, we show the energy dispersion of the

Rashba–Dresselhaus system for three different parameter regimes following Eq. 5.2. In the non-PST regime ($\alpha > \beta$), the bands are touching at a single nodal point (marked by the red dot in Fig. 5.1 (a)) with a non-degenerate band structure. As the two coupling strengths approach each other ($\alpha \approx \beta$), nearly degenerate region appear (see Fig. 5.1 (b)). At the exact PST condition ($\alpha = \beta$), the bands become degenerate and makes a continuous nodal line along the symmetry direction $k_x = k_y$, as shown in Fig. 5.1 (c). This demonstrates that the Rashba–Dresselhaus system provides a versatile platform in which distinct nodal band geometries can be realized by tuning the SOC parameters.

5.3 Quantum geometric quantities and nonlinear Hall response

In this section, we evaluate the quantum geometric quantities of the Rashba–Dresselhaus system and analyze how they evolve across different regimes obtained by tuning the SOC parameters, which consequently modify the underlying nodal band geometry. Although the system exhibits a momentum-dependent winding of the in-plane spin–orbit field, the Berry curvature and BCD vanish identically in the absence of an out-of-plane (σ_z) component. In contrast, the in-plane spin–orbit field gives rise to a finite band-normalized quantum metric, also known as the Berry connection polarizability. Following Eq. 4.53 of the previous chapter, the BCP tensor for this system can be written as (see Eq. D.14 in the appendix D for detailed derivation)

$$\begin{aligned} G^{\pm}_{ab} &= \pm \frac{1}{4|\mathbf{d}(\mathbf{k})|}\, \partial_\alpha \hat{\mathbf{d}}(\mathbf{k}) \cdot \partial_\beta \hat{\mathbf{d}}(\mathbf{k}), \\ &= \pm \frac{(\alpha^2 - \beta^2)^2}{4\Lambda^5} \begin{pmatrix} -k_y^2 & k_y k_x \\ k_y k_x & -k_x^2 \end{pmatrix}. \end{aligned} \tag{5.5}$$

Where $(a, b) = (x, y)$ are spatial directions and $\Lambda = \sqrt{(\beta k_x - \alpha k_y)^2 + (\alpha k_x - \beta k_y)^2}$. In Fig. 5.2, we present density plots of the BCP tensor components. For non-PST ($\alpha > \beta$) regime, the diagonal components G_{xx} and G_{yy} exhibit a characteristic dumbbell-like pattern, as shown in Fig. 5.2(a) and (b), respectively. In contrast, the off-diagonal component G_{xy} displays a quadrupole-like structure, as illustrated in Fig. 5.2(c). However, near the PST condition ($\alpha \approx \beta$), the BCP components develop

a pronounced ridge along the symmetry line $k_x = k_y$, accompanied by an enhancement in their magnitude. This behavior reflects the evolution of the underlying band geometry. As the system evolves from a single-node non-degenerate structure in the non-PST regime to a nearly degenerate region for the near PST condition, the quantum geometric response becomes increasingly concentrated near the symmetry line where the band separation becomes small, leading to a suppression of the denominator in Eq. 5.5. Although the numerator also decreases as $\alpha \to \beta$, the stronger suppression of the denominator results in a pronounced enhancement of the BCP components. However, at the exact PST point ($\alpha = \beta$), the numerator in Eq. 5.5 vanishes identically, causing all BCP components to disappear despite the presence of a nodal line.

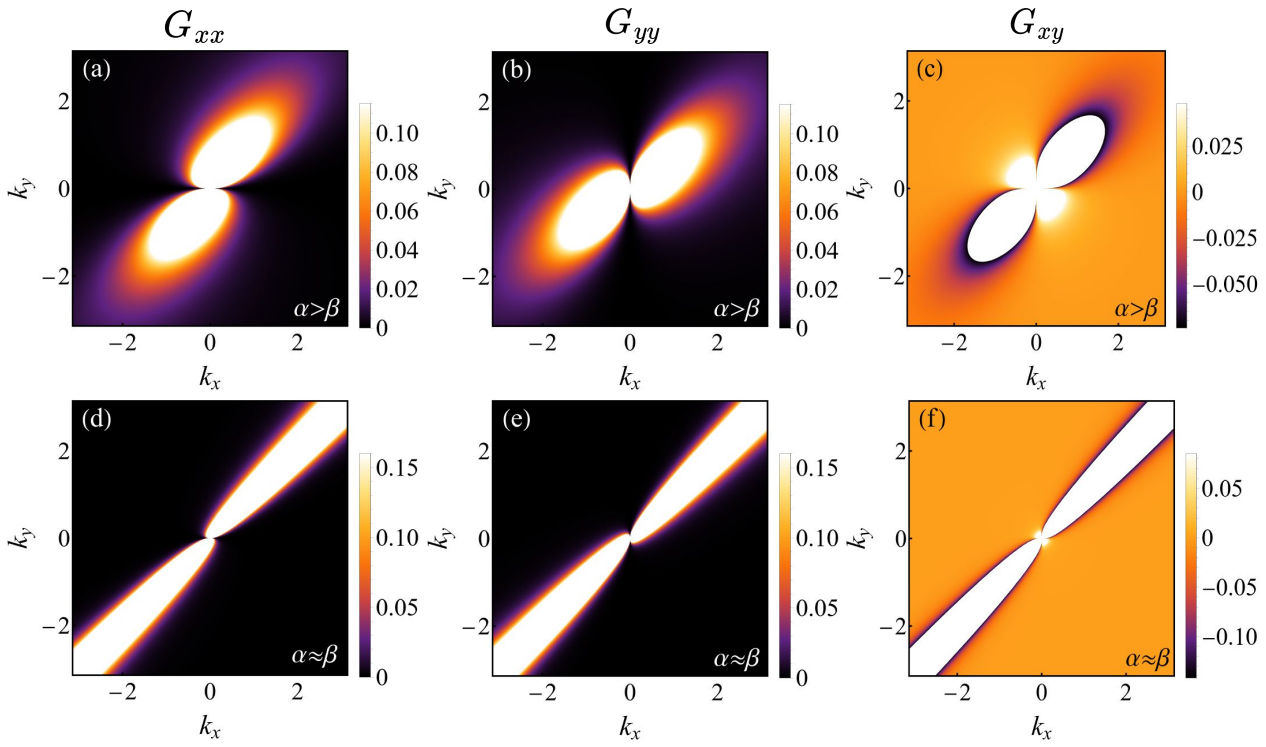

Figure 5.2: Distribution of BCP components G_{xx} (left column), G_{yy} (middle column), and G_{xy} (right column) in momentum space, obtained from the Eq. 5.5. The top row (a-c) corresponds to the non-PST regime ($\alpha > \beta$), while the bottom row (d–f) shows the nearly PST regime ($\alpha \approx \beta$). As we move from a non-PST regime to a nearly PST regime, a pronounced singular ridge develops along the symmetry line $k_x = k_y$, leading to a strong enhancement of the BCP components.

Since the system preserves TRS and the Berry curvature vanishes identically, the linear-order anomalous Hall response becomes suppressed. Moreover, because of the absence of Berry curvature, the BCD becomes zero, and the corresponding second-order Hall conductivity is also suppressed

in this system. Using the obtained BCP tensor components, we now numerically compute the corresponding third-order Hall conductivity tensor as defined in equation 4.58 of chapter 4. In nonlinear Hall experiments, one measures the transverse current response using an in-plane electric field $\mathbf{E} = (E\cos\theta, E\sin\theta)$ oriented at an angle θ to the x-axis. Focusing on the transverse third-order Hall conductivity $\chi_\perp(\theta) = j_\perp^{(3)}/E^3$, we derive its explicit dependence on the applied electric field direction θ and obtain

$$\begin{aligned}\chi_\perp(\theta) = (3\chi_{21} - \chi_{11})\sin\theta\cos^3\theta + 3(\chi_{31} - \chi_{13})\sin^2\theta\cos^2\theta + (\chi_{22} - 3\chi_{12})\sin^3\theta\cos\theta \\ - \chi_{14}\sin^4\theta + \chi_{41}\cos^4\theta,\end{aligned} \tag{5.6}$$

where $\chi_{11} = \chi_{xxxx}$, $\chi_{12} = (\chi_{xxyy} + \chi_{xyyx} + \chi_{xyyx})/3$, $\chi_{13} = (\chi_{xxxy} + \chi_{xxyx} + \chi_{xyxx})/3$, $\chi_{14} = \chi_{xyyy}$, $\chi_{22} = \chi_{yyyy}$, $\chi_{41} = \chi_{yxxx}$, $\chi_{31} = (\chi_{yyyx} + \chi_{yyxy} + \chi_{yxyy})/3$, and $\chi_{21} = (\chi_{yyxx} + \chi_{yxyx} + \chi_{yxxy})/3$.

In Fig. 5.3, we plot the transverse Hall conductivity for both the non-PST and nearly PST regimes. Since the system possesses a symmetry line along $k_x = k_y$, the transverse conductivity vanishes when the electric field is oriented along or perpendicular to this symmetry line, i.e., when $\theta = (\pi/4, 3\pi/4, 5\pi/4, 7\pi/4)$, independent of the choice of system parameters. We also observe from Fig. 5.3 that the transverse third-order Hall conductivity becomes significantly enhanced as the system approaches the nearly PST regime compared to the non-PST regime. In particular, the conductivity increases by approximately a factor of four when the system evolves from a single-node non-degenerate structure to the nearly degenerate structure near the PST condition. This enhancement is a direct consequence of the larger BCP tensor components in the nearly PST regime, as discussed earlier. Although the precise enhancement factor varies with the specific choice of system parameters, the overall trend remains the same. To further illustrate this behavior, we have also plotted the conductivity for another non-PST regime ($\alpha < \beta$), which confirms that the enhanced response occurs only near the PST regime where nearly degenrate region appear in the energy dispersion.

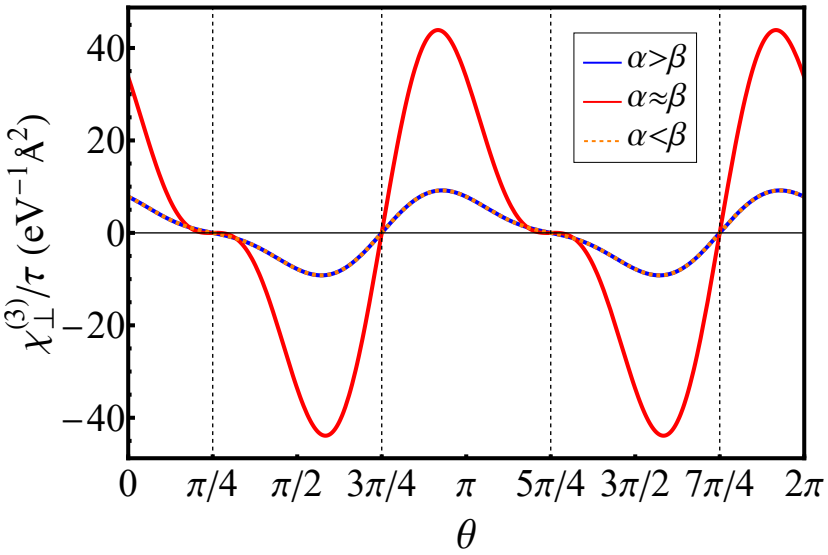

Figure 5.3: Third-order transverse Hall conductivity in different regimes of the Rashba-Dresselhaus system as a function of the electric field orientation θ relative to the x-axis. Black dotted vertical lines present the field directions at which the response vanishes due to symmetry constraints. The parameters are the same as used in Fig. 5.1, while the case ($\alpha < \beta$) is obtained by interchanging the values used for ($\alpha > \beta$). The conductivity is evaluated at a constant energy $\varepsilon_F = 0.2$ eV and temperature T = 50 K.

5.4 Summary

In this chapter, we have investigated the nonlinear Hall response in the Rashba–Dresselhaus system from the perspective of quantum geometry. Motivated by the suppression of current-induced spin polarization at the PST point, we have examined how charge transport responds to an external electric field in this system. Due to the presence of TRS and the purely in-plane nature of the spin–orbit field, both the Berry curvature and the BCD vanish, eliminating the linear and second-order Hall responses.

We have shown that the Berry connection polarizability is the only conventional geometric quantity contributing to the nonlinear Hall response in this system. By tuning the Rashba and Dresselhaus SOC parameters, the system exhibits different nodal band geometries, evolving from a single-node non-degenerate structure in the non-PST regime to a nearly degenerate structure for the near PST condition and eventually forming a nodal line at the exact PST point.

Our analysis reveals that the nonlinear Hall response is strongly influenced by this underlying nodal band geometry. In particular, when the system is tuned close to the PST regime, the BCP tensor

becomes enhanced, leading to a pronounced increase in the transverse third-order Hall conductivity. However, at the exact PST point ($\alpha = \beta$), the BCP vanishes identically, resulting in the disappearance of the nonlinear Hall response. In principle, a finite response can be obtained even at the PST point by introducing a small gap through an additional term $\Delta\sigma_z$ in the Hamiltonian, which can produce a nonzero third-order Hall response with maximum enhancement. However, such a term breaks the TRS of the system. This naturally raises the question of whether a large nonlinear Hall response can be achieved by tuning the nodal geometry of the band structure while preserving the symmetries of the system. In the next chapter, we address this question by exploring a semimetallic system where the nonlinear response is governed by the underlying band geometry.

Chapter 6

Nonlinear Hall responses in tunable nodal Dirac semimetals

In this chapter, we investigate how tuning the nodal geometry of the band structure enables a large nonlinear Hall response while preserving time-reversal symmetry. We analyze quantum geometry-driven second and third-order nonlinear Hall responses in a time-reversal symmetric two-dimensional Dirac semimetallic system that can host single, double, and nodal-ring band crossings by tuning the model parameters. We find that the second-order Hall (SOH) response, which originates from the Berry curvature dipole, is enhanced in the single-node semimetallic phase as compared to the double-node case when inversion symmetry is broken. In contrast, the SOH effect vanishes in the nodal-ring phase as the inversion symmetry is retained. Notably, the TOH response arises from Berry connection polarizability, becomes much larger in the nodal-ring phase than in the single and double-node phases, especially when the Fermi energy lies near the band edge. This contrasting behavior is attributed to the distinct distribution of the Berry connection polarizability in the Brillouin zone.

6.1 Introduction

In recent years, the geometry of quantum states has become crucial for understanding various unconventional electronic and optical phenomena such as photogalvanic effect, nonlinear magneto-optical responses, nonlinear Nernst effect, nonlinear Hall effect, and many more [171–176]. The Berry curvature (BC), introduced in Sec. 4.0.2, is a key quantity that captures the geometry of quantum states and is known to drive the anomalous Hall effect in systems that break time-reversal symmetry [32, 177]. Moreover, the higher-order moments of the BC, namely the Berry curvature dipole (BCD) and quadrupole [156, 171, 178–180] can generate nonlinear Hall effects under different symmetry conditions. Very recently, new geometric contributions to nonlinear transport have been identified, particularly those arising from interband coherence and higher-order geometric corrections. One such quantity is the Berry connection polarizability (BCP) [44, 167], which we have introduced in Sec. 4.0.5.3. The BCP measures how the interband Berry connection responds to changes in energy within the band structure, providing an intrinsic mechanism for nonlinear Hall effects beyond the conventional dipole picture [44, 45, 181]. In addition, BCP is shown to serve as a probe of the Néel vector orientation [181, 182] even in PT-symmetric antiferromagnetic systems.

Dirac semimetal (DSM) with symmetry-protected band crossings provide an excellent platform to study the effect of quantum geometry on various physical properties. Based on the dimensionality and nature of the band crossings, semimetals can be classified as Dirac [183–186], Weyl [187–191], and nodal-ring semimetal (NRSM) [192–199]. While DSM and Weyl semimetal (WSM) feature discrete band-touching points, NRSM exhibit one-dimensional crossings that form continuous loops in momentum space [200, 201]. Breaking certain symmetries can induce transitions between these phases. For example, a DSM can transform into a WSM when either time-reversal or inversion symmetry is broken [202, 203]. In some ferromagnetic materials such as $HgCr_2Se_4$, Co_2TiX (X = Si, Ge, Sn), and Fe_2MnX (X = P, As, Sb), tuning material parameters enables transitions between NRSM and WSM phases [203–206]. Beyond 3D systems, two-dimensional analogs of Dirac, Weyl, and nodal-ring semimetals have been realized in transition-metal dichalcogenides, graphene heterostructures, and mixed honeycomb–kagomé lattices [183, 207–209].

The presence of distinct nodal structures in materials is found to host distinct physical properties such as optical response[210, 211], magneto-optical transition[212], chiral anomaly induced negative magnetoresistance[213, 214], drumhead surface states, and unique electromagnetic responses[215]. Motivated by the distinct properties of distinct nodal structures, we aim to understand how the geometric quantities change across these nodal points and subsequently affect the nonlinear transport properties of nodal materials. To address this, we consider a low-energy model Hamiltonian of a Dirac semimetal that hosts distinct nodal structures depending on the model parameters. We then investigate how quantum geometric quantities evolve across distinct nodal phases. A family of two-dimensional semimetals, MX with M = Pd, Pt, and X =S, Se, Te [216, 217], provides a promising platform to explore these effects. We find that BCD is significantly enhanced in the gapped single-node phase as compared to the double-node phase. This behavior arises due to the distinct distribution of the Berry curvatures near the nodal structure. As a result, the second-order Hall (SOH) response is larger in the single-node phase than in the double-node phase. In contrast, the SOH response vanishes in the nodal-ring phase because the Berry curvature is identically zero. However, all three phases exhibit a non-zero third-order Hall (TOH) response due to the presence of a nonzero BCP. Interestingly, the nodal-ring phase shows a much stronger BCP along the ring compared to the other two phases. Consequently, we observe an enhanced TOH response near the band edge in the nodal-ring phase, compared to the band structures with single or double nodes. This behavior can be traced back to the way BCP tensors are distributed in the Brillouin zone for the different nodal configurations. Overall, these findings provide a useful pathway to identify materials with enhanced nonlinear responses among nodal systems.

The following sections are organised as follows: In Sec. 6.2, we introduce the model Hamiltonian and the underlying symmetries. By following the expressions for the electrically driven higher-order Hall conductivities in terms of quantum geometric quantities, which we have discussed in chapter 4, we present numerical results showing the evolution of second-order and third-order Hall responses across various nodal phases in Sec. 6.3.1 and 6.3.2. Finally, in Sec. 6.4, we summarize our main findings and discuss the future outlook.

6.2 Model Hamiltonian

We consider a low-energy model Hamiltonian for a two-dimensional semi-metallic system[215, 216, 218, 219] as

$$H = \mathbf{d}(\mathbf{k}).\boldsymbol{\sigma}, \tag{6.1}$$

where $\boldsymbol{\sigma} = (\sigma_x, \sigma_y, \sigma_z)$ are the Pauli matrices acting in the pseudospin space, $\mathbf{d}(\mathbf{k}) = (d_x, d_y, d_z) = (\lambda(k^2 - k_0^2), \gamma k_y, 0)$ with $\mathbf{k} = (k_x, k_y)$, denoting the crystal momentum. Here, λ represents the inverse of the band mass, γ characterizes the Fermi velocity along the y direction and k_0 is the parameter that determines the position of the nodal points. The corresponding energy dispersion is given by

$$\epsilon_{\pm} = \pm\sqrt{(\lambda(k^2 - k_0^2))^2 + (\gamma k_y)^2}, \tag{6.2}$$

where $\pm$ denote the conduction and valence bands, respectively. By tuning the parameters γ and k_0 with λ fixed, the system can be continuously driven through distinct gapless semimetallic phases, as illustrated in Fig. 6.1. For $k_0 = 0$ and $\gamma \neq 0$, the two energy bands touch at a single point at

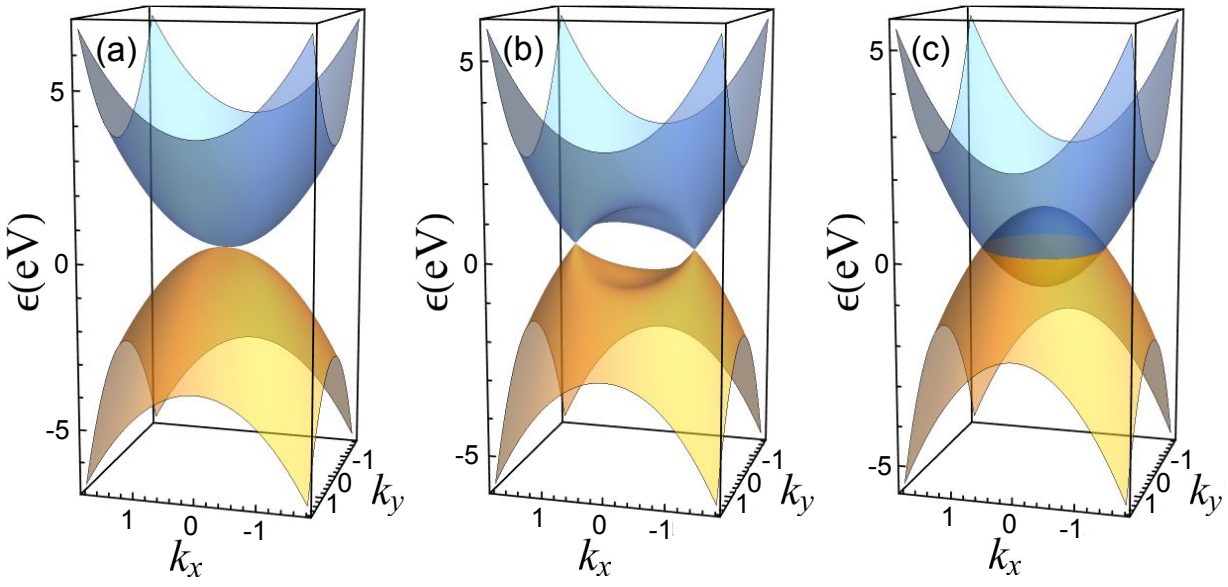

Figure 6.1: Energy spectrum of Eq. 6.1 for different values of parameters γ and k_0, keeping λ fixed. (a) SN phase with single nodal point at $\mathbf{k} = 0$ for $k_0 = 0$ and $\gamma = 1.0$ eV·Å, (b) DN phase with two nodal points located at $\mathbf{k} = (\pm k_0, 0)$ for $k_0 = 1.0$ Å^{-1} and $\gamma = 1$ eV·Å, and (c) NR phase with a nodal ring of radius $k_0 = 1.0$ Å^{-1} and $\gamma = 0$. Here we take $\lambda = 1.0$ eV·Å^2 and momentum k_x, k_y are in units of Å^{-1}.

$\mathbf{k} = 0$, corresponding to a single node (SN) semimetallic phase. For both $k_0 \neq 0$ and $\gamma \neq 0$, the node splits into two distinct band-touching points at $\mathbf{k} = (\pm k_0, 0)$, leading to a double node (DN) phase. Conversely, when $\gamma = 0$ and $k_0 \neq 0$, the discrete nodes expand into a continuous closed loop in momentum space, forming a nodal ring (NR) semimetal with a ring radius equal to k_0. When a finite gap parameter Δ is introduced ($d_z = \Delta$), the system no longer exhibits semimetallic behavior. Nevertheless, for small values of Δ, the energy dispersion continues to reflect the underlying nodal character, with the energy bands extrema occurring near $k = 0$ and $k = k_0$ [217]. Note that for SN and DN phases, the system is invariant under mirror symmetry M_x and the discrete nodal points are located on the mirror line along x direction. In contrast, in the NR phase, the system possesses rotational symmetry. Note that TRS with $\Theta = \mathcal{K}$, where $\mathcal{K}$ denotes the complex conjugation operator, is preserved in all three cases. However, the IS is broken only in SN and DN phases but remains preserved in NR phase.

Although Eq. 6.1 is introduced as a minimal effective model, its different nodal phases are relevant to several experimentally studied systems. The nodal-ring phase is closely related to two-dimensional nodal-line semimetals proposed in the MX family (M = Pd, Pt and X = S, Se, Te), while the single-node phase resembles the semi-Dirac dispersion reported in VO_2/TiO_2 heterostructures [220] and Si_2O [221]. Furthermore, transitions between the SN, DN, and NR phases may be realized by tuning parameters experimentally through various techniques such as strain [159], electrically controlled gate voltages [160], pressure, and chemical composition [222, 223].

6.3 Results

The transition between the gapped nodal phases leads to changes in the underlying geometric quantities, including the BC, BCD, and BCP. These changes directly influence the resulting nonlinear Hall responses. To illustrate these connections, we begin by analyzing the BCD and its role in the second-order Hall effect, followed by a discussion of the BCP and the resulting third-order Hall response.

6.3.1 BCD induced second order Hall effect

The generic form of the Hamiltonian in equation 6.1 allows us to easily evaluate the Berry curvature as (see Eq. D.9 in the appendix D for detailed derivation)

$$\begin{aligned}\Omega_z^{\pm} &= \frac{\mathbf{d}(\mathbf{k}) \cdot \left(\partial_{k_x}\mathbf{d}(\mathbf{k}) \times \partial_{k_y}\mathbf{d}(\mathbf{k})\right)}{2|\mathbf{d}(\mathbf{k})|^3} \\ &= \pm \frac{\lambda k_x \gamma \Delta}{\left[(k^2 - k_0^2)^2\lambda^2 + k_y^2\gamma^2 + \Delta^2\right]^{3/2}}.\end{aligned} \tag{6.3}$$

Evidently, Ω_z is an odd function of k_x. Consequently, following Eq. 4.30 of chapter 4, the total BC integrated over the Brillouin zone vanishes, ensuring that the linear Hall conductivity is zero in this time-reversal-invariant system. We therefore compute the second-order conductivity arising from the BCD.

The velocity components $v_x^{\pm} = 2k_x d_x/\epsilon_{\pm}$ and $v_y^{\pm} = k_y(2d_x + \gamma^2)/\epsilon_{\pm}$, both are odd function in k_x and k_y respectively. Thus following Eq. 4.47 of chapter 4, the integrand $v_x\Omega_z$ for the x component of BCD becomes an even function under momentum inversion and contributes a finite value of D_{xz}. In contrast, for the y component, the integrand $v_y\Omega_z$ becomes an odd function that integrates to zero, thereby suppressing the D_{yz}. This is consistent with the underlying mirror symmetry M_x, which forbids any BCD response along y-direction [156, 224]. Importantly, this finite BCD emerges even without any explicit *tilt* in the band structure. It arises inherently from the distribution of the Berry curvature in momentum space combined with the velocity anisotropy, demonstrating that nonlinear Hall responses can exist in untilted systems when the underlying band geometry lacks complete inversion symmetry in momentum space. The magnitude and profile of this response further depend on the nodal configuration of the system as will be discussed next.

For the NR phase with $\gamma = 0$, the BC vanishes, and therefore this phase possesses no second-order response. We therefore focus only on the finite responses that arise in the SN and DN phases. In the SN phase, Fig. 6.2(a) shows the density plot of the integrand $v_x\Omega_z$. Clearly, this quantity is strongly concentrated near the origin and displays two symmetric positive regions due to k_x^2 term in the numerator, leading to a large net dipole, as seen in Fig. 6.2c. In contrast, in the DN phase, the

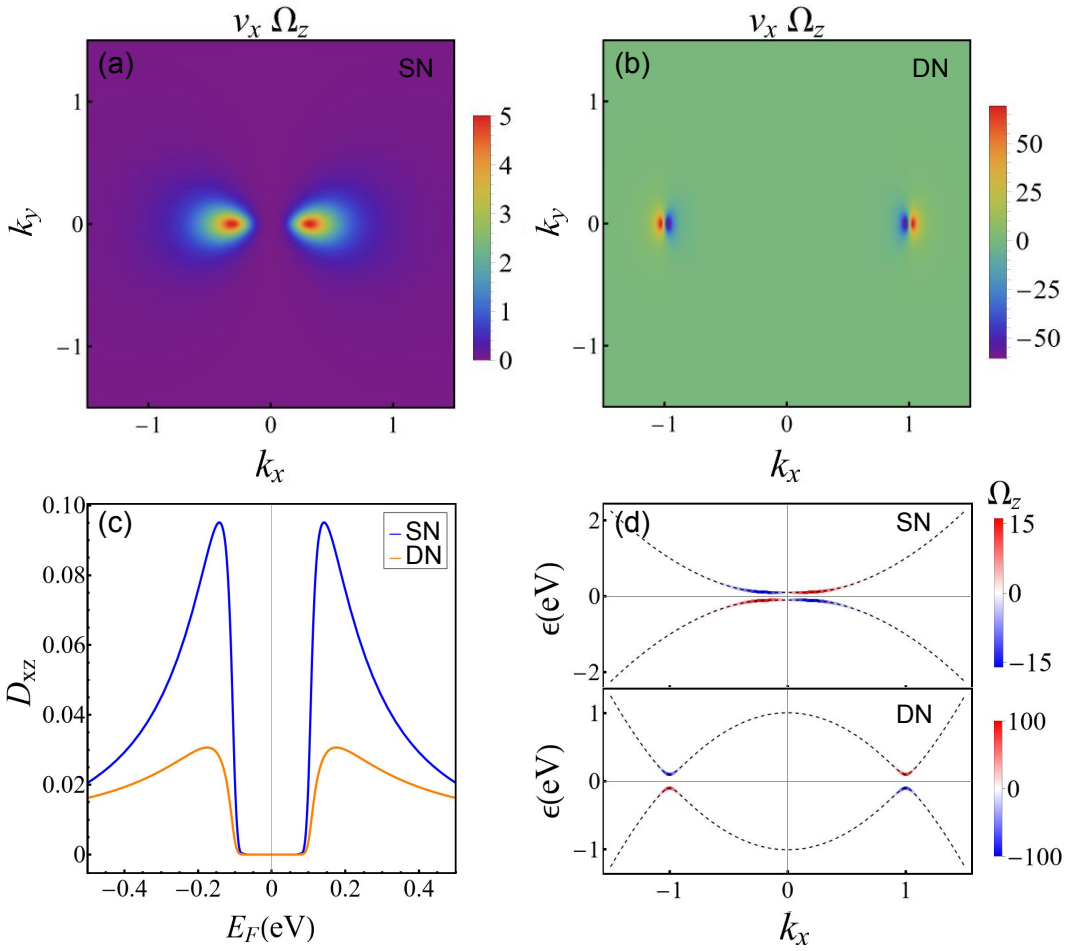

Figure 6.2: (a,b) Density plots showing the Berry curvature (Ω_z) multiplied by the velocity component for the single-node and double-node phases, respectively. (c) Plot of the Berry curvature dipole D_{xz} for both these phases. Here, we take the gap parameter $\Delta = 0.1$ eV. (d) Density plot of Berry curvature along the energy spectrum in the $k_y = 0$ plane for both the SN and DN phases. Here Ω_z and D_{xz} are in units of Å^2 and Å^3 respectively.

integrand shown in Fig. (6.2(b)) is concentrated around $k_x = \pm k_0$, forming a dipole-like structure with opposite signs. As a result, the net dipole contribution is significantly reduced as illustrated in Fig. 6.2(c). In both cases, the response vanishes in the gap region as the BCD is a Fermi surface property. Also, the response reaches to its maximum value near the band edge as BC becomes maximum at the band edges (see Fig. 6.2(d)). Note that as the Hamiltonian is TRS invariant, the BCP induced intrinsic second-order Hall response is absent [225] in all these cases.

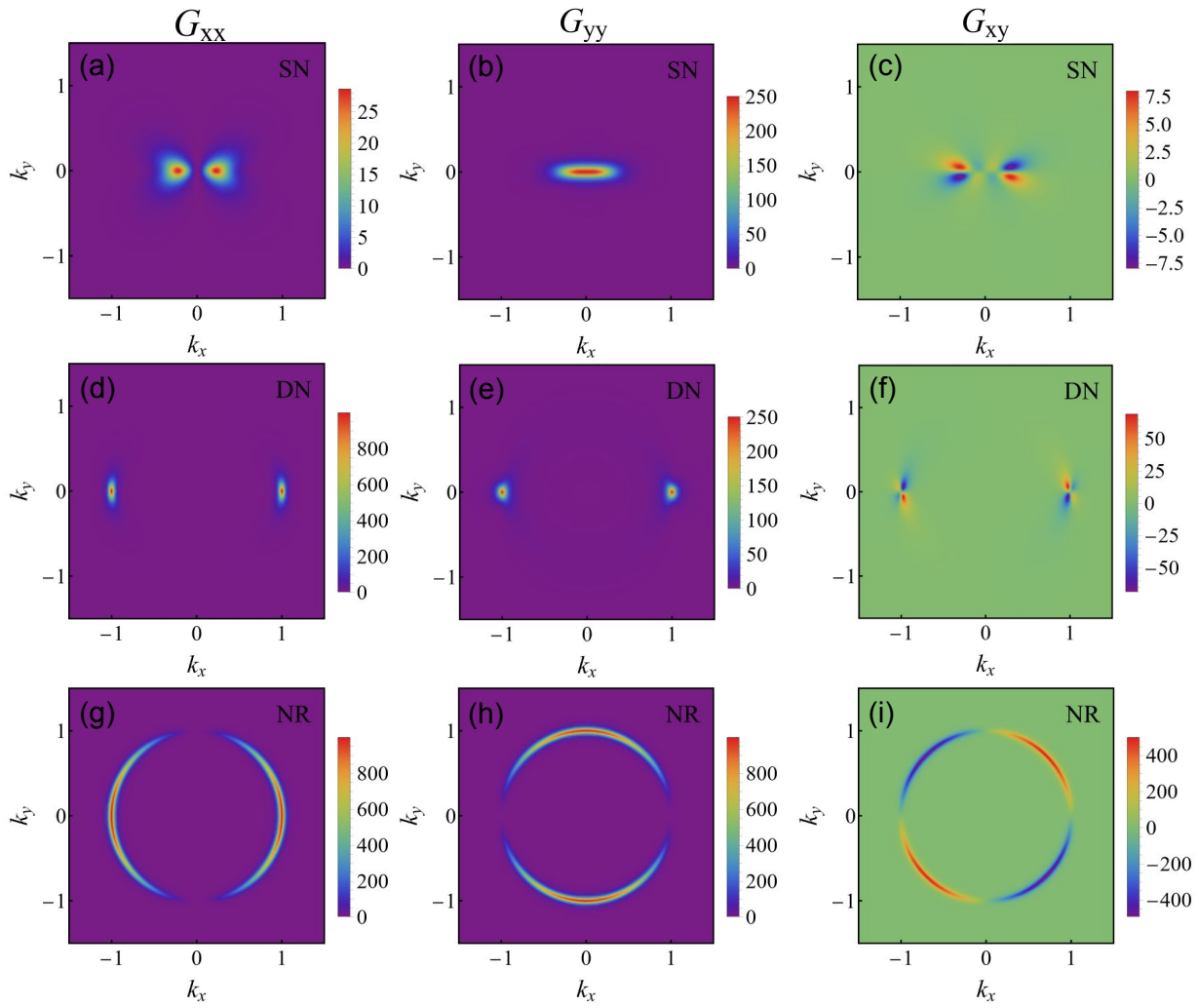

Figure 6.3: Density plots of the BCP tensor components G_{xx}(left column), G_{yy}(middle column) and G_{xy}(middle column) for all three phases, obtained from equation 6.4. The top row (a–c), middle row (d–f), and bottom row (g–i) correspond to the SN, DN, and NR phases, respectively. The plots are shown only for the conduction band. Here we consider the gap $\Delta = 0.1$ eV.

6.3.2 BCP induced third order Hall effect

Since the third-order Hall response is not restricted by TRS and IS [44, 46], we observe a finite BCP-induced TOH response in all three phases. Using Eq. D.14 in the appendix D, different components

of the BCP tensor for the Hamiltonian in equation 6.1 are found to be

$$
\begin{aligned}
G^{\pm}_{xx} &= \pm \frac{k_x^2 \left(k_y^2\gamma^2 + \Delta^2\right)\lambda^2}{\left[(k^2 - k_0^2)^2\lambda^2 + k_y^2\gamma^2 + \Delta^2\right]^{5/2}}, \\
G^{\pm}_{yy} &= \pm \frac{\gamma^2(\Delta^2 + \left(k_0^2 - k_x^2 + k_y^2\right)^2\lambda^2) + 4k_y^2\Delta^2\lambda^2}{4\left[(k^2 - k_0^2)^2\lambda^2 + k_y^2\gamma^2 + \Delta^2\right]^{5/2}}, \\
G^{\pm}_{xy} &= G^{\pm}_{yx} = \pm \frac{k_x k_y(\left(k_0^2 - k_x^2 + k_y^2\right)\gamma^2 + 2\Delta^2)\lambda^2}{2\left[(k^2 - k_0^2)^2\lambda^2 + k_y^2\gamma^2 + \Delta^2\right]^{5/2}}.
\end{aligned} \tag{6.4}
$$

In Fig. 6.3, we have shown the density plots of these BCP tensor components across different nodal phases. Each phase develops its own characteristic BCP structure, and these differences strongly influence the corresponding third-order Hall responses. In the SN phase, one might expect a monopole-like structure near $\boldsymbol{k} = 0$ for the diagonal components, similar to that of a single Dirac-point system [44]. However, in the present model, the G_{xx} component of the BCP displays two symmetric lobes along the k_x-axis, as shown in Fig. 6.3(a). As before, this feature originates from the k_x^2 factor appearing in the numerator of G_{xx} in equation 6.4. This in turn forces the contribution to vanish exactly at the origin. However, in the immediate vicinity of the origin, the denominator becomes small, enhancing the response, leading to two symmetric maxima near k_x=0. In contrast, the G_{yy} and G_{xy} exhibit a monopole and a quadrupole-like structure as illustrated in Fig. 6.3(b) and 6.3(c) respectively, similar to a single Dirac-point system. Note that G_{yy} is significantly larger than both G_{xx} and G_{xy} due to a constant numerator at the origin.

In the DN phase, both the diagonal components G_{xx}, G_{yy} exhibit two localized monopoles, as shown in Fig. 6.3(d) and 6.3(e) respectively. The off-diagonal term G_{xy} shows two quadrupole-like patterns located at $k_x = \pm k_0$, as illustrated in Fig. 6.3(f). Notably, following equation 6.4, the G_{xx} and G_{xy} components exhibit stronger peak intensities as compared to the SN phase. This is attributed to a finite numerator at nodes $k_x = \pm k_0$ as compared to the SN case with $k = 0$. In contrast, the G_{yy} component shows identical peak intensity proportional to $\gamma^2/4\Delta^3$ near ($k_y \approx 0$, $k_x \approx \pm k_0$) and ($\boldsymbol{k} \approx 0$) for DN and SN phase respectively.

In contrast to both the SN and DN phases, the NR phase shows a ring-like BCP pattern, reflecting

the underlying nodal ring geometry, as shown in Fig 6.3(g-i). The G_{xx} and G_{yy} components contain k_x^2 and k_y^2 in the numerator, which results in maximum density along k_x and k_y direction and forms two circular ridges following the ring, as illustrated in Fig 6.3(g) and Fig 6.3(h) respectively. Conversely, the G_{xy} component is proportional to $k_x k_y$, which leads to alternating density extrema in adjacent quadrants and vanishes along $k_x = 0$, $k_y = 0$ direction, shown in Fig 6.3(i). The overall magnitude of all components is larger in the NR phase because of the absence of $\gamma k_y \sigma_y$ term in the denominator, which effectively amplifies their intensity. For the G_{xx} component in both NR and DN phases, the dominant contribution arises near $k_y \approx 0$, and $k_x = \pm k_0$, where the peak magnitude is proportional to k_0^2/Δ^3. Hence, the G_{xx} component exhibits nearly identical peak intensities in both the NR and DN phases, even though the underlying geometric structures are different.

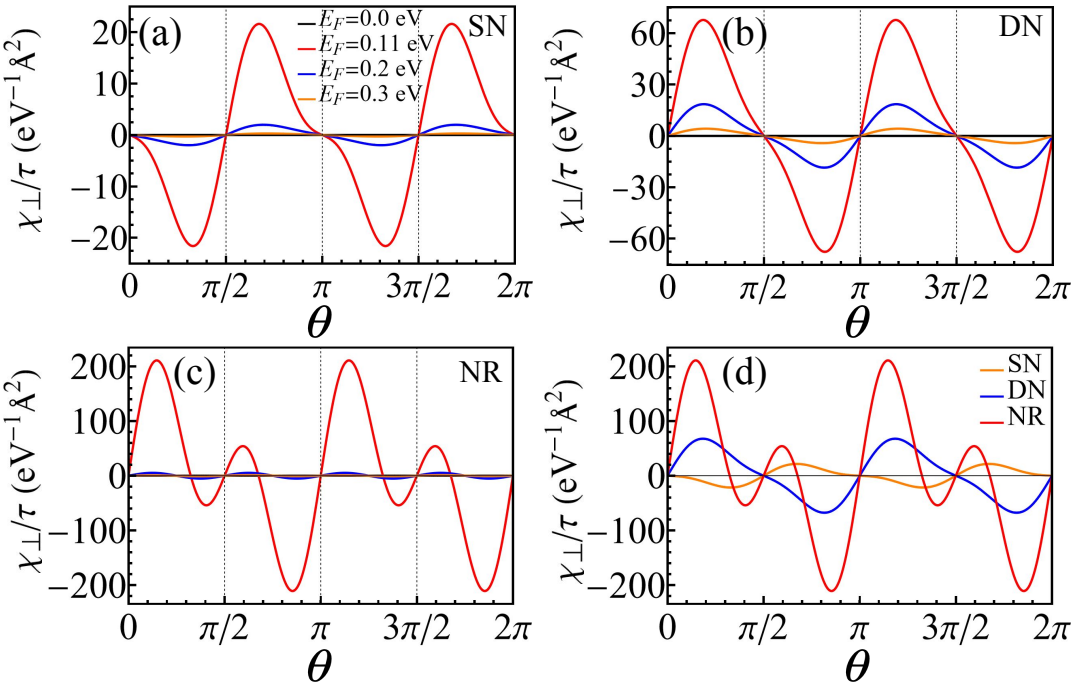

Figure 6.4: The transverse TOH conductivity for different nodal phases. (a-c) shows the variation of the transverse TOH response $\chi_\perp$ as a function of the applied electric field direction θ for different Fermi energies E_F in the SN, DN and NR phase respectively. (d) presents the maximum transverse TOH responses together in different phases near the band edge at $E_F = 0.11$ eV. We take temperature T=50K.

Next, we evaluate the transverse third-order Hall conductivity using the obtained BCP tensor components for the present system as we have done earlier for the Rahba Dresselhaus system in Sec. 5.3. For an in-plane electric field $\boldsymbol{E} = (E\cos\theta, E\sin\theta)$ applied at an angle θ with respect

to the x-axis, the transverse third-order Hall conductivity $\chi_\perp(\theta) = j_\perp^{(3)}/E^3$ is given by Eq. (5.6). Using this equation, we have computed and plotted $\chi_\perp(\theta)$ in Fig. 6.4 for all three nodal phases of the system.

Note that the SN and DN phases preserve the M_x mirror symmetry. This symmetry ensures that the tensor components involving an odd number of x and y in the index (like χ_{xyyy}, χ_{yxxx}) must vanish [44, 46]. As a result, following Eq. (5.6), the transverse TOH conductivity $\chi_\perp$ vanishes when θ becomes integer multiples of $\pi/2$, i.e., along and perpendicular to the mirror line in Fig. 6.4(a) and Fig. 6.4(b), respectively. For both SN and DN phases, the BCP components have maximum density concentrated near the gapped nodal points. Also, there is an anisotropy in the dispersion present through $\gamma k_y \sigma_y$ term which leads to a nonzero transverse TOH response [44, 46, 157]. As seen in Fig 6.3, the BCP components in DN phase are larger in magnitude than SN phase. Consequently, the TOH response becomes higher in DN phase at every value of the Fermi energy than the SN phase, as shown in Fig 6.4(a) and Fig 6.4 (b).

In the NR phase, the Fermi surface appears to be isotropic when $\gamma = 0$. But the system still shows the largest third-order transverse Hall response near the band edge, as illustrated in Fig. 6.4(d). This occurs because the BCP components in the NR phase contain strongly momentum-dependent anisotropic terms such as k_x^2, k_y^2, and $k_x k_y$ in the numerator, while the denominator has a ring-like factor $((k^2 - k_0^2)^2\lambda^2 + \Delta^2)^{5/2}$, which peaks sharply near $k \approx k_0$. As a result, the BCP distribution in momentum space becomes highly localized and anisotropic around the nodal ring. Accordingly, the individual $\chi_{\alpha\beta\gamma\delta}$ components in the transverse conductivity $\chi_\perp$ do not cancel each other and give a nonzero response. Also, in this phase, the system has rotational symmetry and ensures that the tensor components involving odd indices must vanish. As a result, the transverse TOH conductivity vanishes when the electric field is applied along the directions $\theta = n\pi/2$, where n is an integer. The finite TOH response at other field orientations remains physically allowed. The additional zeros appearing in the angular dependence for the NR phase (see Fig. 6.4 (c)) are not symmetry-enforced but arise from cancellations among different tensor components contributing to $\chi_\perp$. We also observe that as we move the Fermi energy far away from the band edge, the TOH responses in every phase start diminishing as the BCP tensor is concentrated near the nodal points. For the NR phase, the

BCP components are sharply localized along the nodal ring only, whereas for SN and DN phases, the BCP components are broadly localized near the nodal points. This explains why the TOH response sharply diminishes for NR phase than the other two phases if we move away from the band edges.

In experiments, the TOH signal may also receive contributions from Berry curvature quadrupole (BCQ) [180, 226], disorder, quantum metric dipole (QMD) [227], and quantum metric quadrupole (QMQ) [228] along with the BCP. Since our system is TRS invariant, BCQ, QMD, and the side-jump contributions are forbidden under symmetry consideration [180, 229]. However, skew-scattering can still generate a third-order Hall signal. This extrinsic mechanism shows a characteristic $\sin 2\theta$ angular dependency that differs from the BCP-induced transverse response [229]. Moreover, the QMQ produces only a longitudinal third-order signal and no transverse component, so it does not overlap with the BCP-induced transverse TOH response.

Here, we discuss a possible experimental prediction of the magnitudes of both SOH and TOH responses across different phases. To obtain realistic predictions, we consider experimentally relevant parameters for two-dimensional nodal Dirac semimetals with a thickness of $t \sim 1$ nm configured in the conventional Hall bar geometry with size $l \times w \sim 100 \times 20\ \mu\text{m}^2$ [46]. Considering a scattering time of $\tau \sim 1 \times 10^{-12}$ s and a resistivity of $\rho \sim 2\ \mu\Omega$ m, a driving current of magnitude $I_0 = 0.5$ mA can generate an electric field of approximately E = 500 V/cm. Using the BCD component D_{xz} values obtained from Fig. 6.2, at $E_F = 0.14$ eV the estimated SOH conductivities are found to be $\zeta^{\text{SN}}_{yxx} = 1.748 \times 10^{-12}$ A m V^{-2} and $\zeta^{\text{DN}}_{yxx} = 5.06 \times 10^{-13}$ A m V^{-2}, yielding SOH voltages ($\text{V}^{(2)}_{\text{H}} \propto \zeta\ E^2$) of approximately $\text{V}^{(2),\text{SN}}_{\text{H}} \sim 174.8\ \mu$V and $\text{V}^{(2),\text{DN}}_{\text{H}} \sim 50.6\ \mu$V for the SN and DN phases, respectively. Similarly, when the field angle is around $\theta = \pi/6$ (see Fig. 6.4 (d)), the estimated TOH conductivities are found to be $\chi^{\text{NR}}_{\perp} = 6.9 \times 10^{-19}$ A m^2/V^3, $\chi^{\text{DN}}_{\perp} = 2.46 \times 10^{-19}$ A m^2/V^3, and $\chi^{\text{SN}}_{\perp} = -3.18 \times 10^{-20}$ A m^2/V^3, corresponding to TOH voltages ($\text{V}^{(3)}_{\text{H}} \propto \chi_{\perp}\ E^3$) of approximately 3.45 μV, 1.23 μV, and $-0.16\ \mu$V for the NR, DN, and SN phases, respectively. Although based on a minimal low-energy model with representative parameters, the qualitative features are expected to persist in realistic nodal semimetals. Material-specific predictions for the MX (M = Pd, Pt; X = S, Se, Te) family require effective model parameters obtained from first-principles calculations.

6.4 Summary

We have studied the nonlinear Hall response in tunable nodal semimetals. By tuning the band parameters, we have traced the transition between single-node, double-node, and nodal-ring phases. Each phase shows a different pattern of quantum geometric quantities and a different hierarchy of nonlinear responses. As the system is TRS invariant and inversion asymmetric, both SN and DN phases exhibit the BCD-induced extrinsic second-order Hall responses. This response in the SN phase turns out to be larger than the DN phase as a manifestation of the distinct distribution of the Berry curvature in the DN phase. For the NR phase, this quantity vanishes as the inversion symmetry is restored. We further find that the BCP becomes finite for all these cases and contributes to a nonzero third-order Hall response. We find that in the NR phase, the BCP components have a larger magnitude and are sharply confined near the band edge along the nodal ring. This leads to an enhanced TOH response however it falls quickly as the Fermi level moves away from the band edge. It is worth pointing out that the system shows these nonlinear Hall responses inherently in all nodal phases without any tilt or warping of the Fermi surface [230]. In sum, our study highlights 2D semimetallic systems with tunable nodal phases that can be used to control quantum geometry-driven transport phenomena.

Chapter 7

Summary and discussion

In this thesis, we have investigated electric field-driven transport phenomena in low-dimensional time reversal symmetric systems, focusing on two important aspects: current-induced spin polarization and nonlinear Hall responses. Particular emphasis is placed on understanding how crystal symmetry, momentum-dependent spin–orbit coupling, nodal band geometry, and quantum geometric properties of electronic bands influence these transport phenomena.

In the first part of the thesis, we have studied current-induced spin polarization in two-dimensional electron gases with Rashba and Dresselhaus spin–orbit interactions. We have demonstrated that the nature of the induced spin polarization is strongly determined by the underlying point-group symmetry of the system. Surfaces with C_n symmetry can support both transverse and longitudinal spin polarization relative to the applied electric field, while systems possessing mirror symmetry (C_{nv}) allow only transverse spin polarization. We have further shown that higher-order SOC terms, particularly cubic in momentum terms, lead to qualitatively new spin-response behavior beyond the conventional linear Rashba–Dresselhaus model. In contrast to the linear case, the cubic terms introduce a strong Fermi-energy dependence, enhance the spin polarization at higher energies, and modify both the Fermi contours and spin textures. These effects result in the anisotropic spin polarization with tunable magnitude and orientation.

In this context, an interesting situation arises when the strengths of the Rashba and Dresselhaus couplings become equal. In this regime, the system can host a persistent spin texture. We find that

under the exact PST condition, the electrically induced spin polarization vanishes due to the emergent SU(2) symmetry of the Hamiltonian, which renders the eigenstates momentum-independent. Although the spin polarization is suppressed in this regime, the electronic band structure develops a distinctive nodal band geometry, which plays an important role in determining other transport responses, especially the nonlinear Hall response.

In view of this, in the second part of the thesis, we have discussed the nonlinear Hall transport arising from quantum geometric properties. In particular, we have examined two different quantities responsible for the nonlinear Hall response: the Berry curvature dipole and the Berry connection polarizability. These quantities originate from the geometric structure of the Bloch wave functions and can generate a nonlinear Hall response even in time-reversal symmetric systems.

Building on this framework, we have analyzed nonlinear Hall response in the Rashba–Dresselhaus system. In this system, the combined presence of time-reversal symmetry and the purely in-plane nature of the spin–orbit field ensures that both the Berry curvature and the Berry curvature dipole vanish identically. As a result, neither the linear anomalous Hall effect nor the second-order Hall response can arise. In this situation, nonlinear transport is governed entirely by the Berry connection polarizability, which provides the leading-order contribution, i.e., the third-order Hall response.

One of the central results of this part of the thesis is that the underlying nodal structure of the band dispersion strongly controls the nonlinear Hall response. By tuning the relative strengths of the Rashba and Dresselhaus couplings, the system undergoes a continuous evolution of its band geometry, ranging from a single nodal point non-degenerate band structure in the non-PST regime to multiple nodes a single nodal point nearly degenerate band structure for near the PST condition, and finally forming a nodal line at the exact PST point. This evolution has a direct impact on the distribution of quantum geometric quantities in momentum space. In particular, as the system approaches the PST regime, the Berry connection polarizability becomes significantly enhanced, leading to a strong increase in the transverse third-order Hall response. In contrast, at the exact PST point, the Berry connection polarizability vanishes identically, resulting in the complete suppression of the nonlinear Hall response.

However, a finite and enhanced nonlinear Hall response can still be realized at the PST point

through the introduction of a gap term, which necessarily breaks time-reversal symmetry. To avoid this, we extend our analysis to tunable nodal Dirac semimetals, where different nodal phases can be realized by varying the model parameters, and the nonlinear Hall response can be explored within symmetry-preserving conditions. In this system, we have systematically investigated the nonlinear Hall response across single-node, double-node, and nodal-ring phases. Owing to the presence of time-reversal symmetry and the absence of inversion symmetry, the single-node and double-node phases exhibit a finite Berry curvature dipole, giving rise to a second-order Hall response. We find that this response is stronger in the single-node phase, reflecting the more localized and asymmetric distribution of Berry curvature in momentum space. In contrast, in the nodal-ring phase, inversion symmetry is effectively restored, leading to a complete suppression of the Berry curvature dipole and hence the second-order Hall response.

At the same time, the Berry connection polarizability remains finite in all three nodal phases and generates a third-order Hall response. A particularly important finding is that the nodal-ring phase exhibits a strong enhancement of the Berry connection polarizability near the band edge, where it becomes sharply concentrated along the nodal ring. This leads to a pronounced third-order Hall response, which is maximized when the Fermi energy lies close to the band edge. Unlike many previously studied systems, these nonlinear responses arise in this tunable Dirac semimetal intrinsically from the band geometry and do not rely on additional mechanisms such as tilt or warping of the Fermi surface.

7.1 Future outlook

The results of this thesis suggest several promising directions for future research. One natural extension is to study the role of disorder and scattering mechanisms in transport phenomena [229, 231]. In realistic materials, impurity scattering and finite relaxation times can significantly influence the magnitude and behavior of electrically driven responses. A systematic understanding of these effects can help to bridge the gap between ideal theoretical predictions and experimental observations.

Another important direction is to explore how temperature affects electric-field-driven transport

phenomena [232, 233]. Thermal effects modify the distribution of carriers near the Fermi surface and can strongly affect the underlying quantum geometric quantities. Exploring this aspect may provide deeper insight into how thermal fluctuations interplay with band geometry in shaping nonlinear transport.

Furthermore, it would be interesting to explore these phenomena in more complex material platforms, including systems with strong correlations or multi-orbital character, where additional quantum geometric features may emerge. Advances in material engineering and device fabrication may also enable the realization of tunable systems with controllable spin–orbit coupling and nodal band structures. Such systems would allow direct experimental verification of the theoretical predictions presented in this thesis and could open pathways toward novel spintronic and nonlinear electronic applications. In addition, it would be interesting to explore current-induced orbital polarization (orbital Edelstein effect) [89, 151, 233], where orbital responses may become significant or even dominate over spin polarization, particularly in systems with higher-order or mixed spin–orbit coupling.

In summary, the interplay between symmetry, spin–orbit coupling, nodal band geometry, and quantum geometric properties provides a rich landscape of transport phenomena. The results presented in this thesis contribute to this broader understanding and offer useful guidance for future theoretical and experimental studies for designing next-generation spintronic and nonlinear electronic systems.

Appendices

Appendix A

Calculation of spin polarization

This appendix provides a detailed calculation of the different components of spin polarization (Eq. 3.4, 3.6 and 3.7 in chapter 3), resulting from applying an electric field in various directions using the Kubo linear response theory.

We begin with the Hamiltonian for a system that includes a linear k-dependent RSOC and a DSOC(+) term (for simplicity, we neglect the kinetic energy term, as it does not change the eigenfunctions):

$$H = \alpha(k_x\sigma_y - k_y\sigma_x) + \beta(k_x\sigma_x + k_y\sigma_y), \tag{A.1}$$

where (k_x, k_y) represents the $2D$ crystal momentum, (σ_x, σ_y) denotes the Pauli matrices, and α, β corresponds to the Rashba and Dresselhaus coupling parameters, respectively. The energy dispersion becomes,

$$\varepsilon_{\pm} = \pm|k|\sqrt{\alpha^2 + \beta^2}. \tag{A.2}$$

A.0.1 Electric field applied along y direction

For the electric field along y, i. e., $\mathbf{E} = (0, E_y, 0)$, the x component of the spin polarization (from Eq. 3.3 of chapter 3) can be expressed as,

$$\langle S_x \rangle = \frac{eE_y}{2\pi} \int \frac{d^2k}{(2\pi)^2} Tr(\hat{v_y} G_A(\varepsilon_F) \hat{S}_x G_R(\varepsilon_F)), \tag{A.3}$$

where the y component of the velocity operator $\hat{v_y}$ is given by

$$v_y = \begin{pmatrix} 0 & -\alpha - i\beta \\ -\alpha + i\beta & 0 \end{pmatrix}. \tag{A.4}$$

Here G_R and G_A are the retarded and advanced Green's functions, respectively. They are expressed as

$$G_{R/A} = \frac{1}{(\alpha^2+\beta^2)k^2 - (\varepsilon_F \pm i\eta)^2} \begin{pmatrix} -(\varepsilon_F \pm i\eta) & (\alpha + i\beta)(k_y + ik_x) \\ (\alpha - i\beta)(k_y - ik_x) & -(\varepsilon_F \pm i\eta) \end{pmatrix}, \tag{A.5}$$

where ε_{F} is Fermi energy and the broadening parameter η represents the inverse of the relaxation time τ. Finally, the $\langle S_x \rangle$ component in Eq. A.3 become

$$\begin{aligned} \langle S_x \rangle &= \frac{eE_y}{8\pi^3} \int_0^{\varepsilon_F/\sqrt{\alpha^2+\beta^2}} k\,dk \int_0^{2\pi} d\theta \frac{k^2(\alpha^2+\beta^2)(\alpha\cos 2\theta + \beta \sin 2\theta) - \alpha(\varepsilon_F^2 + \eta^2)}{\varepsilon_F^4 + 2\varepsilon_F^2(\eta^2 - (\alpha^2+\beta^2)k^2) + (k^2(\alpha^2+\beta^2) + \eta^2)^2} \\ &= -\frac{eE_y \alpha(\varepsilon_F^2 + \eta^2)}{16\pi^2 \varepsilon_F (\alpha^2+\beta^2)\eta} \times (\tan^{-1}[\frac{\eta^2 - \varepsilon_F^2 + (\alpha^2+\beta^2)k^2}{2\varepsilon_F \eta}]) \Big|_0^{(\varepsilon_F/\sqrt{\alpha^2+\beta^2})}. \end{aligned} \tag{A.6}$$

Similarly, the y and z components of spin polarization (using Eq. 3.3 of chapter 3) are found to be

$$\langle S_y\rangle = \frac{eE_y}{8\pi^3}\int_0^{\varepsilon_F/\sqrt{\alpha^2+\beta^2}} kdk \int_0^{2\pi} d\theta \frac{k^2(\alpha^2+\beta^2)(-\beta\cos 2\theta + \alpha\sin 2\theta) + \beta(\varepsilon_F^2+\eta^2)}{\varepsilon_F^4 + 2\varepsilon_F^2(\eta^2 - (\alpha^2+\beta^2)k^2)) + (k^2(\alpha^2+\beta^2)+\eta^2)^2}$$
$$= \frac{eE_y\beta(\varepsilon_F^2+\eta^2)}{16\pi^2\varepsilon_F(\alpha^2+\beta^2)\eta}(\tan^{-1}[\frac{\eta^2-\varepsilon_F^2+(\alpha^2+\beta^2)k^2}{2\varepsilon_F\eta}])\Big|_0^{(\varepsilon_F/\sqrt{\alpha^2+\beta^2})}, \tag{A.7}$$

$$\langle S_z\rangle = \frac{eE_y}{8\pi^3}\int_0^{\varepsilon_F/\sqrt{\alpha^2+\beta^2}} kdk \int_0^{2\pi} d\theta \frac{k(\alpha^2+\beta^2)\eta\cos\theta}{\varepsilon_F^4 + 2\varepsilon_F^2(\eta^2 - (\alpha^2+\beta^2)k^2)) + (k^2(\alpha^2+\beta^2)+\eta^2)^2}. \tag{A.8}$$

For $\eta \ll 2\varepsilon_F$, the simplified form can be expressed as,

$$\langle S_x\rangle \approx -\frac{eE_y\alpha\varepsilon_F}{32\pi(\alpha^2+\beta^2)\eta},$$
$$\langle S_y\rangle \approx \frac{eE_y\beta\varepsilon_F}{32\pi(\alpha^2+\beta^2)\eta},$$
$$\langle S_z\rangle = 0. \tag{A.9}$$

Thus, we derive the Eq. (3.6) of chapter 3, and the difference in the sign between x and y components is evident. Next, we discuss the effect of the different relative strengths of RSOC and DSOC(+) on spin polarization.

A.0.1.1 Case: $\alpha = \beta$

When the strengths of RSOC and DSOC(+) are equal, the components of the spin polarization become,

$$\langle S_x\rangle \approx -\frac{eE_y\varepsilon_F}{64\pi\alpha\eta}, \quad \langle S_y\rangle \approx \frac{eE_y\varepsilon_F}{64\pi\alpha\eta}$$
$$\langle S_z\rangle = 0. \tag{A.10}$$

A.0.1.2 Case: $\alpha \neq 0, \beta = 0$

For only RSOC to be present in the system, the components of spin polarization are obtained to be,

$$\langle S_x \rangle \approx -\frac{eE_y\varepsilon_F}{32\pi\alpha\eta}; \;\; \langle S_y \rangle = 0; \;\; \langle S_z \rangle = 0. \tag{A.11}$$

This corroborates the standard REE effect.

A.0.1.3 Case: $\alpha = 0, \beta \neq 0$

In the presence of only DSOC(+), the components of spin polarization can be written as,

$$\langle S_x \rangle = 0; \;\; \langle S_y \rangle \approx \frac{eE_y\varepsilon_F}{32\pi\beta\eta}; \;\; \langle S_z \rangle = 0. \tag{A.12}$$

A.0.2 Electric field applied along x direction

As discussed in the chapter 3, the sign of the spin components of the spin polarization depends on the direction of the applied field. To see, we now apply field along x, i. e., $\mathbf{E} = (E_x, 0, 0)$. With this, the components of the spin polarization are given by

$$\begin{aligned}\langle S_x \rangle &= \frac{eE_x}{8\pi^3}\int_0^{\varepsilon_F/\sqrt{\alpha^2+\beta^2}} k\,dk \int_0^{2\pi} d\theta \frac{k^2(\alpha^2+\beta^2)(\beta\cos 2\theta - \alpha\sin 2\theta) + \beta(\varepsilon_F^2+\eta^2)}{\varepsilon_F^4 + 2\varepsilon_F^2(\eta^2 - (\alpha^2+\beta^2)k^2) + (k^2(\alpha^2+\beta^2)+\eta^2)^2} \\ &= \frac{eE_x\beta(\varepsilon_F^2+\eta^2)}{16\pi^2\varepsilon_F\eta(\alpha^2+\beta^2)} \times (\tan^{-1}[\frac{\eta^2 - \varepsilon_F^2 + (\alpha^2+\beta^2)k^2}{2\eta\varepsilon_F}])\Big|_0^{(\varepsilon_F/\sqrt{\alpha^2+\beta^2})},\end{aligned} \tag{A.13}$$

$$\langle S_y\rangle = \frac{eE_x}{8\pi^3}\int_0^{\varepsilon_F/\sqrt{\alpha^2+\beta^2}} kdk \int_0^{2\pi} d\theta \frac{k^2(\alpha^2+\beta^2)(\alpha\cos 2\theta+\beta\sin 2\theta)+\alpha(\varepsilon_F^2+\eta^2)}{\varepsilon_F^4+2\varepsilon_F^2(\eta^2-(\alpha^2+\beta^2)k^2)+(k^2(\alpha^2+\beta^2)+\eta^2)^2}$$
$$= \frac{eE_x\alpha(\varepsilon_F^2+\eta^2)}{16\pi^2\varepsilon_F\eta(\alpha^2+\beta^2)} \times (\tan^{-1}[\frac{\eta^2-\varepsilon_F^2+(\alpha^2+\beta^2)k^2}{2\eta\varepsilon_F}])\Big|_0^{(\varepsilon_F/\sqrt{\alpha^2+\beta^2})}, \tag{A.14}$$

$$\langle S_z\rangle = -\frac{eE_x}{8\pi^3}\int_0^{\varepsilon_F/\sqrt{\alpha^2+\beta^2}} kdk \int_0^{2\pi} d\theta \frac{k\eta(\alpha^2+\beta^2)\sin\theta}{\varepsilon_F^4+2\varepsilon_F^2(\eta^2-(\alpha^2+\beta^2)k^2))+(k^2(\alpha^2+\beta^2)+\eta^2)^2}$$
$$= 0. \tag{A.15}$$

And for $\eta \ll 2\varepsilon_{\mathrm{F}}$, the components can be simplified as,

$$\langle S_x\rangle \approx \frac{eE_x\beta\varepsilon_F}{32\pi\eta(\alpha^2+\beta^2)},$$
$$\langle S_y\rangle \approx \frac{eE_x\alpha\varepsilon_F}{32\pi\eta(\alpha^2+\beta^2)},$$
$$\langle S_z\rangle = 0. \tag{A.16}$$

Thus recover the Eq. (3.7) of the chapter 3. Evidently, both the spin components have the same sign as opposed to the case discussed in the preceding section. For different respective strengths of RSOC and DSOC(+), the spin polarization can be obtained very easily as before. In the presence of only RSOC term ($\alpha \neq 0,\ \beta = 0$) Eq. A.16 become

$$\langle S_y\rangle \approx \frac{eE_x\varepsilon_{\mathrm{F}}}{32\pi\alpha\eta}, \langle S_x\rangle = \langle S_z\rangle = 0,$$

which is shown in Eq. 3.4 of chapter 3.

A.0.3 2DEG with only Dresselhaus terms

We now compute the spin polarization components for systems that feature only BIA, or in other words, systems with only linear DSOC terms in a 2DEG. We particularly focus on the DSOC(-) term and then compare it with the DSOC(+) term discussed in the preceding paragraph. As before,

neglecting the kinetic energy term, the Hamiltonian for DSOC(-) is

$$H_{-} = \beta(k_x\sigma_x - k_y\sigma_y). \tag{A.17}$$

Then we find

$$\begin{aligned}\langle S_y\rangle_{-} &= -\frac{eE_y\varepsilon_F}{32\pi\beta\eta},\\ \langle S_x\rangle_{-} &= \langle S_z\rangle_{-} = 0,\end{aligned} \tag{A.18}$$

for the field along the y direction. Here " $-$ " refers to the contribution from the DSOC(-). Clearly, we see longitudinal spin polarization with respect to the applied field similar to the DSOC(+) case (cf. Eq. (A.12)) but with an opposite sign.

Appendix B

Derivation of the modified velocity expression

In this appendix, we outline the intermediate steps leading from the corrected Bloch eigenstate to the modified expression for the electron velocity given in Eq 4.23 of the introduction chapter.

In the adiabatic limit, the instantaneous Bloch eigenstate acquires a correction due to coupling with other bands. Up to first order in the rate of change of the Hamiltonian, the eigenstate can be written as

$$|u_m(\mathbf{k},t)\rangle = |u_m(\mathbf{k})\rangle - i\hbar \sum_{n\neq m} \frac{|u_n(\mathbf{k})\rangle\langle u_n(\mathbf{k})|\partial_t u_m(\mathbf{k},t)\rangle}{\varepsilon_m - \varepsilon_n}. \tag{B.1}$$

The velocity operator in momentum space is defined as

$$\hat{v}(\mathbf{k}) = \frac{1}{\hbar}\frac{\partial H}{\partial \mathbf{k}}. \tag{B.2}$$

To obtain the electron velocity, we evaluate the expectation value of this operator with the corrected eigenstate in Eq. (B.1). Keeping terms up to first order in the time variation of the Hamiltonian yields

$$\mathbf{v}_m(\mathbf{k}) = \frac{1}{\hbar}\nabla_{\mathbf{k}}\varepsilon_m(\mathbf{k}) - i\sum_{n\neq m}\left[\frac{\langle u_m|\frac{\partial H}{\partial \mathbf{k}}|u_n\rangle\langle u_n|\partial_t u_m\rangle}{\varepsilon_m - \varepsilon_n} - \text{c.c.}\right]. \tag{B.3}$$

To simplify this expression, we use the identity

$$\langle u_m|\frac{\partial H}{\partial \mathbf{k}}|u_n\rangle = (\varepsilon_m - \varepsilon_n)\left\langle \frac{\partial u_m}{\partial \mathbf{k}}\middle| u_n\right\rangle, \tag{B.4}$$

which follows from differentiating the eigenvalue equation $H(\mathbf{k})|u_n(\mathbf{k})\rangle = \varepsilon_n(\mathbf{k})|u_n(\mathbf{k})\rangle$ with respect to $\mathbf{k}$ and projecting onto $\langle u_m(\mathbf{k})|$ for $m \neq n$.

Substituting Eq. (B.4) into Eq. (B.3) and using the completeness relation

$$\sum_{n\neq m} |u_n\rangle\langle u_n| = 1 - |u_m\rangle\langle u_m|, \tag{B.5}$$

we obtain

$$\mathbf{v}_m(\mathbf{k}) = \frac{1}{\hbar}\nabla_{\mathbf{k}}\varepsilon_m(\mathbf{k}) - i\left[\langle \nabla_{\mathbf{k}} u_m|\partial_t u_m\rangle - \langle \nabla_{\mathbf{k}} u_m|u_m\rangle\langle u_m|\partial_t u_m\rangle - \text{c.c.}\right]. \tag{B.6}$$

The second term inside the brackets can be simplified using the normalization condition of the Bloch states, $\langle u_m(\mathbf{k},t)|u_m(\mathbf{k},t)\rangle = 1$. Taking the derivative with respect to $\mathbf{k}$ and time t respectively gives

$$\begin{aligned}\langle \nabla_{\mathbf{k}} u_m|u_m\rangle + \langle u_m|\nabla_{\mathbf{k}} u_m\rangle &= 0\\ \langle \partial_t u_m|u_m\rangle + \langle u_m|\partial_t u_m\rangle &= 0.\end{aligned} \tag{B.7}$$

These relations imply that the quantities $\langle \nabla_{\mathbf{k}} u_m|u_m\rangle$ and $\langle u_m|\partial_t u_m\rangle$ are purely imaginary. Therefore their product is real. Since the velocity expression contains the difference between this term and its complex conjugate, the contribution cancels out. As a result, the velocity reduces to

$$\mathbf{v}_m(\mathbf{k}) = \frac{1}{\hbar}\nabla_{\mathbf{k}}\varepsilon_m(\mathbf{k}) - i\left[\langle \nabla_{\mathbf{k}} u_m|\partial_t u_m\rangle - \langle \partial_t u_m|\nabla_{\mathbf{k}} u_m\rangle\right]. \tag{B.8}$$

Appendix C

Derivation of the non-equilibrium distribution function

In this appendix, we present a detailed derivation of the non-equilibrium distribution function up to second order in the applied electric field within the semiclassical Boltzmann formalism, which we have shown in Eq. 4.42 of section 4.0.5.2.

We begin with the Boltzmann equation in the relaxation-time approximation as earlier mentioned in Eq. 4.41:

$$(1 + \tau\partial_t)f = f_{eq} + e\tau E_a(t)\,\partial_a f. \tag{C.1}$$

To solve this equation, we expand the distribution function in powers of the electric field as

$$f = f_{eq} + f_1 + f_2 + \cdots, \tag{C.2}$$

where f_1 and f_2 are the first- and second-order corrections, respectively. Substituting this expansion into the Boltzmann equation and collecting terms order by order, we first consider the zeroth-order term, which gives

$$(1 + \tau\partial_t)f_{eq} = f_{eq}. \tag{C.3}$$

This implies $\partial_t f_{eq} = 0$, confirming that the equilibrium distribution is time independent. At first

order in the electric field, we obtain

$$(1 + \tau\partial_t) f_1 = e\tau E_a(t)\, \partial_a f_{eq}. \tag{C.4}$$

We consider the oscillating applied electric field with driving frequency ω of the form

$$E_a(t) = Re\{E_a e^{i\omega t}\} = \frac{1}{2}(E_a e^{i\omega t} + E_a^* e^{-i\omega t}), \tag{C.5}$$

and look for a solution of the form $f_1(t) = f_1^\omega e^{i\omega t}$ (considering only positive frequency), where f_1^ω is time independent. Substituting into the left-hand side of Eq. C.4, we evaluate

$$(1 + \tau\partial_t) f_1(t) = f_1^\omega e^{i\omega t} + \tau \frac{\partial}{\partial t}\left(f_1^\omega e^{i\omega t}\right) \tag{C.6}$$

$$= f_1^\omega e^{i\omega t} + \tau\left(i\omega f_1^\omega e^{i\omega t}\right) \tag{C.7}$$

$$= (1 + i\omega\tau) f_1^\omega e^{i\omega t}. \tag{C.8}$$

The right-hand side of Eq. C.4 becomes

$$e\tau E_a(t)\, \partial_a f_{eq} = e\tau E_a \partial_a f_{eq}\, e^{i\omega t}. \tag{C.9}$$

Equating both sides of Eq. C.4 and canceling the common factor $e^{i\omega t}$, we obtain

$$(1 + i\omega\tau) f_1^\omega = e\tau E_a \partial_a f_{eq}, \tag{C.10}$$

which gives the first-order correction

$$f_1^\omega = \frac{e\tau E_a \partial_a f_{eq}}{1 + i\omega\tau}. \tag{C.11}$$

We now proceed to the second-order correction. At order E^2, the Boltzmann equation in Eq. C.1 gives

$$(1 + \tau\partial_t) f_2 = e\tau E_a(t)\, \partial_a f_1. \tag{C.12}$$

Using $f_1(t) = f_1^{\omega} e^{i\omega t}$ and the expression of f_1^{ω}, the right-hand side of the above equation become

$$e\tau E_a(t)\,\partial_a f_1 = e\tau \frac{1}{2}(E_a e^{i\omega t} + E_a^* e^{-i\omega t}) \cdot \frac{e\tau E_b \partial_{ab} f_{eq}}{1 + i\omega\tau} e^{i\omega t} \tag{C.13}$$

$$= \frac{(e\tau)^2 E_a^* E_b \partial_{ab} f_{eq}}{2(1 + i\omega\tau)} + \frac{(e\tau)^2 E_a E_b \partial_{ab} f_{eq}}{2(1 + i\omega\tau)} e^{2i\omega t}. \tag{C.14}$$

Since the right-hand side contains products of oscillating terms of the form $E(t) f_1(t)$, which generate contributions at both zero frequency (dc) and at 2ω. Therefore, the second-order correction in the distribution function contains two parts, which can be written as

$$f_2(t) = f_2^0 + f_2^{2\omega} e^{2i\omega t}. \tag{C.15}$$

Hence, the left-hand side of the Eq. C.12 becomes

$$\begin{aligned}(1 + \tau\partial_t) f_2(t) &= f_2^0 + f_2^{2\omega} e^{2i\omega t} + 2i\omega\tau f_2^{2\omega} e^{2i\omega t} \\ &= f_2^0 + (1 + 2i\omega\tau) f_2^{2\omega} e^{2i\omega t}.\end{aligned} \tag{C.16}$$

Equating both sides of the Eq. C.12, we can write

$$\begin{aligned}f_2^0 &= \frac{(e\tau)^2 E_a^* E_b \partial_{ab} f_{eq}}{2(1 + i\omega\tau)} \\ f_2^{2\omega} &= \frac{(e\tau)^2 E_a E_b \partial_{ab} f_{eq}}{2(1 + i\omega\tau)(1 + 2i\omega\tau)}.\end{aligned} \tag{C.17}$$

Finally, the distribution function up to second order can be written as

$$f = f_{eq} + f_1^{\omega} e^{i\omega t} + (f_2^0 + f_2^{2\omega} e^{2i\omega t}). \tag{C.18}$$

Appendix D

Berry curvature and Berry connection polarizability for two-band Hamiltonian

In this appendix, we derive the Berry curvature and the Berry connection polarizability for a generic two-band Hamiltonian in terms of the $\mathbf{d}(\mathbf{k})$ vector, which we have used in chapter 5 and chapter 6.

We consider a generic two-band Hamiltonian of the form

$$H(\mathbf{k}) = d_0(\mathbf{k}) + \mathbf{d}(\mathbf{k}) \cdot \boldsymbol{\sigma}, \tag{D.1}$$

where $\mathbf{d}(\mathbf{k}) = (d_x, d_y, d_z)$ and $\boldsymbol{\sigma}$ are the Pauli matrices. The corresponding eigenvalues are

$$\varepsilon_{\pm}(\mathbf{k}) = d_0(\mathbf{k}) \pm |\mathbf{d}(\mathbf{k})|. \tag{D.2}$$

Following the expression in Eq. 4.19, the Berry curvature for a two-band system with band indices $n = \pm$ can be written as

$$\Omega^{\pm}_{\alpha\beta} = i \frac{\langle \pm|\partial_\alpha H|\mp\rangle\langle\mp|\partial_\beta H|\pm\rangle - (\alpha \leftrightarrow \beta)}{(\epsilon_\pm - \epsilon_\mp)^2}, \tag{D.3}$$

where $(\alpha, \beta) = (x, y, z)$ are spatial directions, $\partial_\alpha = \partial/\partial k_\alpha$ and $(\epsilon_\pm - \epsilon_\mp) = \pm 2|\mathbf{d}|$. The derivative of

the Hamiltonian is given by

$$\partial_\alpha H = (\partial_\alpha d_0) + (\partial_\alpha d_i)\sigma_i. \tag{D.4}$$

The scalar term does not contribute between different bands due to orthogonality, so

$$\langle \pm|\partial_\alpha H|\mp\rangle = (\partial_\alpha d_i)\,\langle \pm|\sigma_i|\mp\rangle. \tag{D.5}$$

Substituting this into the Berry curvature, we obtain

$$\Omega^{\pm}_{\alpha\beta} = \frac{i}{4|\mathbf{d}|^2}(\partial_\alpha d_i)(\partial_\beta d_j)\left[\langle \pm|\sigma_i|\mp\rangle\langle\mp|\sigma_j|\pm\rangle - (\alpha \leftrightarrow \beta)\right]. \tag{D.6}$$

Using the identity $\sigma_i\sigma_j = \delta_{ij} + i\epsilon_{ijk}\sigma_k$, and the expectation value $\langle \pm|\sigma_k|\pm\rangle = \pm d_k/|\mathbf{d}|$, we can write

$$\langle \pm|\sigma_i|\mp\rangle\langle\mp|\sigma_j|\pm\rangle = \delta_{ij} \pm i\epsilon_{ijk}\left(\frac{d_k}{|\mathbf{d}|}\right) - \frac{d_i d_j}{|\mathbf{d}|^2}. \tag{D.7}$$

Upon substitution, the symmetric terms vanish under antisymmetrization in α, β, and only the antisymmetric contribution survives. This yields

$$\Omega^{\pm}_{\alpha\beta} = \pm\frac{1}{4|\mathbf{d}|^3}2\epsilon_{ijk}\,d_i\,(\partial_\alpha d_j)\,(\partial_\beta d_k). \tag{D.8}$$

Finally, we can write the Berry curvature for two-band systems in terms of $\mathbf{d}$ vector as

$$\Omega^{\pm}_{\alpha\beta}(\mathbf{k}) = \pm\frac{1}{2}\,\frac{\mathbf{d}(\mathbf{k})\cdot\left(\partial_\alpha\mathbf{d}(\mathbf{k})\times\partial_\beta\mathbf{d}(\mathbf{k})\right)}{|\mathbf{d}(\mathbf{k})|^3}. \tag{D.9}$$

Similarly, we derive the expression of the Berry connection polarisability, which is expressed in Eq. 4.53 as

$$G_{m,\alpha\beta} = 2\,\mathrm{Re}\sum_{n\neq m}\frac{A_{mn,\alpha}\,A_{nm,\beta}}{\epsilon_m - \epsilon_n}, \tag{D.10}$$

where the Berry connection, $A_{mn,\alpha} = i\langle m|\partial_\alpha n\rangle$. Using the identity $\langle m|\partial_\alpha n\rangle = \langle m|\partial_\alpha H|n\rangle/(\epsilon_n - \epsilon_m)$

for $(m \neq n)$, we can write the Eq. D.10 for two-band Hamiltonian as

$$G^{\pm}_{\alpha\beta} = 2\,\mathrm{Re}\left[\frac{\langle\pm|\partial_\alpha H|\mp\rangle\langle\mp|\partial_\beta H|\pm\rangle}{(\epsilon_\pm - \epsilon_\mp)^3}\right]. \tag{D.11}$$

This expression can be rewritten by using Eq. D.5 as

$$G^{\pm}_{\alpha\beta} = 2\,\mathrm{Re}\left[\frac{(\partial_\alpha d_i)(\partial_\beta d_j)\langle\pm|\sigma_i|\mp\rangle\langle\mp|\sigma_j|\pm\rangle}{8|\mathbf{d}|^3}\right]. \tag{D.12}$$

Substituting the matrix elements given in Eq. D.7 and taking the real part, we obtain

$$G^{\pm}_{\alpha\beta} = \pm\frac{1}{4|\mathbf{d}|^3}\left[(\partial_\alpha d_i)(\partial_\beta d_i) - \frac{d_i d_j(\partial_\alpha d_i)(\partial_\beta d_j)}{|\mathbf{d}|^2}\right]. \tag{D.13}$$

Finally, the Berry connection polarisability for a generic two-band system in terms of $\mathbf{d}$ vector can be written as

$$\begin{aligned} G^{\pm}_{\alpha\beta} &= \pm\frac{1}{4|\mathbf{d}|^3}\left[(\partial_\alpha \mathbf{d})\cdot(\partial_\beta \mathbf{d}) - \frac{(\mathbf{d}\cdot\partial_\alpha\mathbf{d})(\mathbf{d}\cdot\partial_\beta\mathbf{d})}{|\mathbf{d}|^2}\right] \\ &= \pm\frac{1}{4|\mathbf{d}(\mathbf{k})|}\,\partial_\alpha\hat{\mathbf{d}}(\mathbf{k})\cdot\partial_\beta\hat{\mathbf{d}}(\mathbf{k}). \end{aligned} \tag{D.14}$$

Bibliography

[1] J. J. Liou and F. Schwierz, Journal of Telecommunications and Information Technology , 99 (2004).

[2] A. Johansson, J. Henk, and I. Mertig, Phys. Rev. B **93**, 195440 (2016).

[3] S. Datta, *Electronic Transport in Mesoscopic Systems*, Cambridge Studies in Semiconductor Physics and Microelectronic Engineering (Cambridge University Press, 1995).

[4] J. Rammer, *Quantum transport theory* (cRc Press, 2018).

[5] R. K. Goyal, S. Maharaj, P. Kumar, and M. Chandrasekhar, Journal of Materials Science: Materials in Engineering **20**, 4 (2025).

[6] J. Ziman, *Electrons and Phonons: The Theory of Transport Phenomena in Solids* (Oxford University Press, 2001).

[7] N. W. Ashcroft and N. D. Mermin, Solid state physics, cornell university (1976).

[8] N. Nagaosa, J. Sinova, S. Onoda, A. H. MacDonald, and N. P. Ong, Rev. Mod. Phys. **82**, 1539 (2010).

[9] D. Xiao, M.-C. Chang, and Q. Niu, Rev. Mod. Phys. **82**, 1959 (2010).

[10] L. E. Bell, Science **321**, 1457 (2008), https://www.science.org/doi/pdf/10.1126/science.1158899 .

[11] P. Sun, B. Wei, J. Zhang, J. M. Tomczak, A. Strydom, M. Søndergaard, B. B. Iversen, and F. Steglich, Nature communications **6**, 7475 (2015).

[12] K. Behnia and H. Aubin, Reports on Progress in Physics **79**, 046502 (2016).

[13] J. Sinova, S. O. Valenzuela, J. Wunderlich, C. H. Back, and T. Jungwirth, Reviews of Modern Physics **87**, 1213 (2015).

[14] A. Manchon, H. C. Koo, J. Nitta, S. M. Frolov, and R. A. Duine, Nature Materials **14**, 871–882 (2015).

[15] I. Žutić, J. Fabian, and S. Das Sarma, Rev. Mod. Phys. **76**, 323 (2004).

[16] A. Hirohata, K. Yamada, Y. Nakatani, I.-L. Prejbeanu, B. Diény, P. Pirro, and B. Hillebrands, Journal of Magnetism and Magnetic Materials **509**, 166711 (2020).

[17] M. N. Baibich, J. M. Broto, A. Fert, F. N. Van Dau, F. Petroff, P. Etienne, G. Creuzet, A. Friederich, and J. Chazelas, Phys. Rev. Lett. **61**, 2472 (1988).

[18] G. Binasch, P. Grünberg, F. Saurenbach, and W. Zinn, Phys. Rev. B **39**, 4828 (1989).

[19] S. S. P. Parkin, N. More, and K. P. Roche, Phys. Rev. Lett. **64**, 2304 (1990).

[20] S. A. Wolf, D. D. Awschalom, R. A. Buhrman, J. M. Daughton, S. von Molnár, M. L. Roukes, A. Y. Chtchelkanova, and D. M. Treger, Science **294**, 1488 (2001), https://www.science.org/doi/pdf/10.1126/science.1065389 .

[21] G. Schmidt, D. Ferrand, L. W. Molenkamp, A. T. Filip, and B. J. van Wees, Phys. Rev. B **62**, R4790 (2000).

[22] A. G. Aronov and Y. B. Lyanda-Geller, Soviet Journal of Experimental and Theoretical Physics Letters **50**, 431 (1989).

[23] V. Edelstein, Solid State Communications **73**, 233 (1990).

[24] P. M. Haney, H.-W. Lee, K.-J. Lee, A. Manchon, and M. D. Stiles, Phys. Rev. B **87**, 174411 (2013).

[25] A. Manchon, J. Železný, I. M. Miron, T. Jungwirth, J. Sinova, A. Thiaville, K. Garello, and P. Gambardella, Rev. Mod. Phys. **91**, 035004 (2019).

[26] E. H. Hall, American Journal of Mathematics **2**, 287 (1879).

[27] R. Popović, Sensors and Actuators **17**, 39 (1989).

[28] M.-A. Paun, J.-M. Sallese, and M. Kayal, Journal of Sensor and Actuator Networks **2**, 85 (2013).

[29] E. H. Hall, Proceedings of the Physical Society of London **4**, 325 (1880).

[30] R. Karplus and J. M. Luttinger, Phys. Rev. **95**, 1154 (1954).

[31] M. V. Berry, Proceedings of the Royal Society of London. A. Mathematical and Physical Sciences **392**, 45 (1984), https://royalsocietypublishing.org/rspa/article-pdf/392/1802/45/65511/rspa.1984.0023.pdf .

[32] D. Xiao, M.-C. Chang, and Q. Niu, Rev. Mod. Phys. **82**, 1959 (2010).

[33] D. J. Thouless, M. Kohmoto, M. P. Nightingale, and M. den Nijs, Phys. Rev. Lett. **49**, 405 (1982).

[34] C.-Z. Chang, C.-X. Liu, and A. H. MacDonald, Rev. Mod. Phys. **95**, 011002 (2023).

[35] C.-Z. Chang, J. Zhang, X. Feng, J. Shen, Z. Zhang, M. Guo, K. Li, Y. Ou, P. Wei, L.-L. Wang, Z.-Q. Ji, Y. Feng, S. Ji, X. Chen, J. Jia, X. Dai, Z. Fang, S.-C. Zhang, K. He, Y. Wang, L. Lu, X.-C. Ma, and Q.-K. Xue, Science **340**, 167 (2013), https://www.science.org/doi/pdf/10.1126/science.1234414 .

[36] A. L. Sharpe, E. J. Fox, A. W. Barnard, J. Finney, K. Watanabe, T. Taniguchi, M. A. Kastner, and D. Goldhaber-Gordon, Science **365**, 605 (2019), https://www.science.org/doi/pdf/10.1126/science.aaw3780 .

[37] T. Li, S. Jiang, B. Shen, Y. Zhang, L. Li, Z. Tao, T. Devakul, K. Watanabe, T. Taniguchi, L. Fu, *et al.*, Nature **600**, 641 (2021).

[38] Y. Deng, Y. Yu, M. Z. Shi, Z. Guo, Z. Xu, J. Wang, X. H. Chen, and Y. Zhang, Science **367**, 895 (2020), https://www.science.org/doi/pdf/10.1126/science.aax8156 .

[39] I. Sodemann and L. Fu, Phys. Rev. Lett. **115**, 216806 (2015).

[40] Q. Ma, S.-Y. Xu, H. Shen, D. MacNeill, V. Fatemi, T.-R. Chang, A. M. Mier Valdivia, S. Wu, Z. Du, C.-H. Hsu, *et al.*, Nature **565**, 337 (2019).

[41] J.-X. Hu, C.-P. Zhang, Y.-M. Xie, and K. Law, Communications Physics **5**, 255 (2022).

[42] S. Sinha, P. C. Adak, A. Chakraborty, K. Das, K. Debnath, L. V. Sangani, K. Watanabe, T. Taniguchi, U. V. Waghmare, A. Agarwal, *et al.*, Nature Physics **18**, 765 (2022).

[43] A. Chakraborty, K. Das, S. Sinha, P. C. Adak, M. M. Deshmukh, and A. Agarwal, 2D Materials **9**, 045020 (2022).

[44] H. Liu, J. Zhao, Y.-X. Huang, X. Feng, C. Xiao, W. Wu, S. Lai, W.-b. Gao, and S. A. Yang, Phys. Rev. B **105**, 045118 (2022).

[45] Y. Gao, S. A. Yang, and Q. Niu, Phys. Rev. Lett. **112**, 166601 (2014).

[46] T. Nag, S. K. Das, C. Zeng, and S. Nandy, Phys. Rev. B **107**, 245141 (2023).

[47] S. Saha and A. Narayan, Journal of Physics: Condensed Matter **35**, 485301 (2023).

[48] C. Wang, R.-C. Xiao, H. Liu, Z. Zhang, S. Lai, C. Zhu, H. Cai, N. Wang, S. Chen, Y. Deng, Z. Liu, S. A. Yang, and W.-B. Gao, National Science Review **9**, nwac020 (2022), https://academic.oup.com/nsr/article-pdf/9/12/nwac020/48826293/nwac020.pdf .

[49] S. Lai, H. Liu, Z. Zhang, J. Zhao, X. Feng, N. Wang, C. Tang, Y. Liu, K. Novoselov, S. A. Yang, *et al.*, Nature Nanotechnology **16**, 869 (2021).

[50] J. Schliemann, Rev. Mod. Phys. **89**, 011001 (2017).

[51] J. E. Hirsch, Phys. Rev. Lett. **83**, 1834 (1999).

[52] J. Sinova, S. O. Valenzuela, J. Wunderlich, C. H. Back, and T. Jungwirth, Rev. Mod. Phys. **87**, 1213 (2015).

[53] R. Peierls, Zeitschrift für Physik **80**, 763 (1933).

[54] J. M. Luttinger, Phys. Rev. **84**, 814 (1951).

[55] P. A. M. Dirac, Proceedings of the Royal Society of London. Series A, Containing Papers of a Mathematical and Physical Character **117**, 610 (1928).

[56] R. M. Martin, *Electronic Structure: Basic Theory and Practical Methods* (Cambridge University Press, 2004).

[57] E. I. Rashba, Sov Phys Solid State **2**, 1109 (1960).

[58] Y. A. Bychkov and É. I. Rashba, JETP lett **39**, 78 (1984).

[59] E. Simon, A. Szilva, B. Ujfalussy, B. Lazarovits, G. Zarand, and L. Szunyogh, Phys. Rev. B **81**, 235438 (2010).

[60] K. Ishizaka, M. S. Bahramy, H. Murakawa, M. Sakano, T. Shimojima, T. Sonobe, K. Koizumi, S. Shin, H. Miyahara, A. Kimura, *et al.*, Nature materials **10**, 521 (2011).

[61] J. D. Koralek, C. P. Weber, J. Orenstein, B. A. Bernevig, S.-C. Zhang, S. Mack, and D. Awschalom, Nature **458**, 610 (2009).

[62] S.-J. Gong, C.-G. Duan, Y. Zhu, Z.-Q. Zhu, and J.-H. Chu, Phys. Rev. B **87**, 035403 (2013).

[63] H. J. Zhang, S. Yamamoto, B. Gu, H. Li, M. Maekawa, Y. Fukaya, and A. Kawasuso, Phys. Rev. Lett. **114**, 166602 (2015).

[64] C. R. Ast, D. Pacilé, L. Moreschini, M. C. Falub, M. Papagno, K. Kern, M. Grioni, J. Henk, A. Ernst, S. Ostanin, and P. Bruno, Phys. Rev. B **77**, 081407 (2008).

[65] G. Bihlmayer, P. Noël, D. V. Vyalikh, E. V. Chulkov, and A. Manchon, Nature Reviews Physics **4**, 642 (2022).

[66] G. Dresselhaus, Phys. Rev. **100**, 580 (1955).

[67] W. Roland, Springer Tracts in Modern Physiscs: Springer, Berlin, Heidelberg **191** (2003).

[68] J. J. Krich and B. I. Halperin, Phys. Rev. Lett. **98**, 226802 (2007).

[69] A. Johansson, J. Henk, and I. Mertig, Phys. Rev. B **97**, 085417 (2018).

[70] G. Vignale and I. V. Tokatly, Phys. Rev. B **93**, 035310 (2016).

[71] J. Q. Li and C. M. Wang, Phys. Rev. B **103**, 085401 (2021).

[72] H. Bruus and K. Flensberg, Oxford University Press **1**, 1 (2004).

[73] G. D. Mahan, *Many-particle physics* (Springer Science & Business Media, 2013).

[74] I. Žutić, J. Fabian, and S. Das Sarma, Rev. Mod. Phys. **76**, 323 (2004).

[75] A. Hirohata, K. Yamada, Y. Nakatani, I.-L. Prejbeanu, B. Diény, P. Pirro, and B. Hillebrands, Journal of Magnetism and Magnetic Materials **509**, 166711 (2020).

[76] M. Wu, J. Jiang, and M. Weng, Physics Reports **493**, 61 (2010).

[77] S. LaShell, B. A. McDougall, and E. Jensen, Phys. Rev. Lett. **77**, 3419 (1996).

[78] G. Nicolay, F. Reinert, S. Hüfner, and P. Blaha, Phys. Rev. B **65**, 033407 (2001).

[79] Y. A. Bychkov and E. I. Rashba, Journal of Physics C: Solid State Physics **17**, 6039 (1984).

[80] G. Bihlmayer, O. Rader, and R. Winkler, New Journal of Physics **17**, 050202 (2015).

[81] C. Mera Acosta, E. Ogoshi, A. Fazzio, G. M. Dalpian, and A. Zunger, Matter **3**, 145 (2020).

[82] A. N. Mihalyuk, L. V. Bondarenko, A. Y. Tupchaya, Y. E. Vekovshinin, T. V. Utas, D. V. Gruznev, J.-P. Chou, S. V. Eremeev, A. V. Zotov, and A. A. Saranin, Materials Today Advances **18**, 100372 (2023).

[83] S. Oyarzún, A. Kumar Nandy, F. Rortais, J. C. Rojas Sánchez, M.-T. Dau, P. Noël, P. Laczkowski, S. Pouget, H. Okuno, L. Vila, C. Vergnaud, C. Beigné, A. Marty, J.-P. Attané, S. Gambarelli, J.-M. George, H. Jaffrès, S. Blügel, and M. Jamet, Nature Communications **7**, 13857 (2016).

[84] A. Soumyanarayanan, N. Reyren, A. Fert, and C. Panagopoulos, Nature **539**, 509 (2016).

[85] A. K. Nandy, N. S. Kiselev, and S. Blügel, Phys. Rev. Lett. **116**, 177202 (2016).

[86] Y. Hayakawa, Y. Imai, and H. Kohno, Phys. Rev. B **108**, 064409 (2023).

[87] R. H. Silsbee, Phys. Rev. B **63**, 155305 (2001).

[88] D. T. Perkins and A. Ferreira, Spintronics in 2d graphene-based van der waals heterostructures, in *Encyclopedia of Condensed Matter Physics* (Elsevier, 2024) p. 205–222.

[89] A. Johansson, Journal of Physics: Condensed Matter **36**, 423002 (2024).

[90] Y. K. Kato, R. C. Myers, A. C. Gossard, and D. D. Awschalom, Phys. Rev. Lett. **93**, 176601 (2004).

[91] A. Y. Silov, P. Blajnov, J. Wolter, R. Hey, K. Ploog, and N. Averkiev, Applied physics letters **85**, 5929 (2004).

[92] H. J. Zhang, S. Yamamoto, B. Gu, H. Li, M. Maekawa, Y. Fukaya, and A. Kawasuso, Phys. Rev. Lett. **114**, 166602 (2015).

[93] B. Zhao, B. Karpiak, D. Khokhriakov, A. Johansson, A. M. Hoque, X. Xu, Y. Jiang, I. Mertig, and S. P. Dash, Advanced Materials **32**, 2000818 (2020).

[94] B. Zhao, D. Khokhriakov, Y. Zhang, H. Fu, B. Karpiak, A. M. Hoque, X. Xu, Y. Jiang, B. Yan, and S. P. Dash, Phys. Rev. Res. **2**, 013286 (2020).

[95] Y. Lv, J. Kally, D. Zhang, J. S. Lee, M. Jamali, N. Samarth, and J.-P. Wang, Nature communications **9**, 111 (2018).

[96] N. P. Stern, S. Ghosh, G. Xiang, M. Zhu, N. Samarth, and D. D. Awschalom, Phys. Rev. Lett. **97**, 126603 (2006).

[97] W. Chen, Journal of Physics: Condensed Matter **32**, 035809 (2019).

[98] L. Salemi, M. Berritta, A. Kumar Nandy, and P. Oppeneer, Nature Communications **10** (2019).

[99] P. Wadley, B. Howells, J. Ž elezný, C. Andrews, V. Hills, R. P. Campion, V. Novák, K. Olejník, F. Maccherozzi, S. S. Dhesi, S. Y. Martin, T. Wagner, J. Wunderlich, F. Freimuth, Y. Mokrousov, J. Kuneš, J. S. Chauhan, M. J. Grzybowski, A. W. Rushforth, K. W. Edmonds, B. L. Gallagher, and T. Jungwirth, Science **351**, 587 (2016).

[100] P. Gambardella and I. M. Miron, Philosophical Transactions of the Royal Society A: Mathematical, Physical and Engineering Sciences **369**, 3175 (2011).

[101] S. Vajna, E. Simon, A. Szilva, K. Palotas, B. Ujfalussy, and L. Szunyogh, Phys. Rev. B **85**, 075404 (2012).

[102] H. Nakamura, T. Koga, and T. Kimura, Phys. Rev. Lett. **108**, 206601 (2012).

[103] R. Winkler, H. Noh, E. Tutuc, and M. Shayegan, Phys. Rev. B **65**, 155303 (2002).

[104] R. Moriya, K. Sawano, Y. Hoshi, S. Masubuchi, Y. Shiraki, A. Wild, C. Neumann, G. Abstreiter, D. Bougeard, T. Koga, and T. Machida, Phys. Rev. Lett. **113**, 086601 (2014).

[105] S. Schulz, A. Y. Vyazovskaya, G. Poelchen, A. Generalov, M. Güttler, M. Mende, S. Danzenbächer, M. M. Otrokov, T. Balasubramanian, C. Polley, E. V. Chulkov, C. Laubschat, M. Peters, K. Kliemt, C. Krellner, D. Y. Usachov, and D. V. Vyalikh, Phys. Rev. B **103**, 035123 (2021).

[106] A. Maleki Sheikhabadi, I. Miatka, E. Y. Sherman, and R. Raimondi, Phys. Rev. B **97**, 235412 (2018).

[107] Y. M. Koroteev, G. Bihlmayer, J. E. Gayone, E. V. Chulkov, S. Blügel, P. M. Echenique, and P. Hofmann, Phys. Rev. Lett. **93**, 046403 (2004).

[108] K. Sugawara, T. Sato, S. Souma, T. Takahashi, M. Arai, and T. Sasaki, Phys. Rev. Lett. **96**, 046411 (2006).

[109] C. R. Ast, J. Henk, A. Ernst, L. Moreschini, M. C. Falub, D. Pacilé, P. Bruno, K. Kern, and M. Grioni, Phys. Rev. Lett. **98**, 186807 (2007).

[110] L. Moreschini, A. Bendounan, I. Gierz, C. R. Ast, H. Mirhosseini, H. Höchst, K. Kern, J. Henk, A. Ernst, S. Ostanin, F. Reinert, and M. Grioni, Phys. Rev. B **79**, 075424 (2009).

[111] I. Gierz, B. Stadtmüller, J. Vuorinen, M. Lindroos, F. Meier, J. H. Dil, K. Kern, and C. R. Ast, Phys. Rev. B **81**, 245430 (2010).

[112] H. Mirhosseini, I. V. Maznichenko, S. Abdelouahed, S. Ostanin, A. Ernst, I. Mertig, and J. Henk, Phys. Rev. B **81**, 073406 (2010).

[113] R. Winkler, Springer **85**, 5929 (2003).

[114] L. G. Gerchikov and A. V. Subashiev, Sov. Phys. Semicond. 26, 73. **26**, 73 (1992).

[115] E. Marcellina, A. R. Hamilton, R. Winkler, and D. Culcer, Phys. Rev. B **95**, 075305 (2017).

[116] W. Lin, L. Li, F. Doğan, C. Li, H. Rotella, X. Yu, B. Zhang, Y. Li, W. S. Lew, S. Wang, *et al.*, Nature communications **10**, 3052 (2019).

[117] D. Y. Usachov, I. A. Nechaev, G. Poelchen, M. Güttler, E. E. Krasovskii, S. Schulz, A. Generalov, K. Kliemt, A. Kraiker, C. Krellner, K. Kummer, S. Danzenbächer, C. Laubschat, A. P. Weber, J. Sánchez-Barriga, E. V. Chulkov, A. F. Santander-Syro, T. Imai, K. Miyamoto, T. Okuda, and D. V. Vyalikh, Phys. Rev. Lett. **124**, 237202 (2020).

[118] C.-X. Liu, B. Zhou, S.-Q. Shen, and B.-f. Zhu, Phys. Rev. B **77**, 125345 (2008).

[119] A. Mawrie, T. Biswas, and T. K. Ghosh, Journal of Physics: Condensed Matter **26**, 405301 (2014).

[120] M. Trushin and J. Schliemann, Phys. Rev. B **75**, 155323 (2007).

[121] J. Schliemann, J. C. Egues, and D. Loss, Physical Review Letters **90**, 146801 (2003).

[122] B. A. Bernevig, J. Orenstein, and S.-C. Zhang, Phys. Rev. Lett. **97**, 236601 (2006).

[123] L. L. Tao and E. Y. Tsymbal, Phys. Rev. B **104**, 085438 (2021).

[124] P. A. L. Sino, L.-Y. Feng, R. A. B. Villaos, H. N. Cruzado, Z.-Q. Huang, C.-H. Hsu, and F.-C. Chuang, Nanoscale Adv. **3**, 6608 (2021).

[125] J. Chen, K. Wu, H. Ma, W. Hu, and J. Yang, RSC Adv. **10**, 6388 (2020).

[126] W. Meevasana, P. D. C. King, R. H. He, S.-K. Mo, M. Hashimoto, A. Tamai, P. Songsiriritthigul, F. Baumberger, and Z.-X. Shen, Nature Materials **10**, 114–118 (2011).

[127] M. Michiardi, F. Boschini, H.-H. Kung, M. X. Na, S. K. Y. Dufresne, A. Currie, G. Levy, S. Zhdanovich, A. K. Mills, D. J. Jones, J. L. Mi, B. B. Iversen, P. Hofmann, and A. Damascelli, Nature Communications **13**, 10.1038/s41467-022-30742-5 (2022).

[128] J. Nitta, T. Akazaki, H. Takayanagi, and T. Enoki, Phys. Rev. Lett. **78**, 1335 (1997).

[129] J.-C. Rojas-Sánchez, S. Oyarzún, Y. Fu, A. Marty, C. Vergnaud, S. Gambarelli, L. Vila, M. Jamet, Y. Ohtsubo, A. Taleb-Ibrahimi, P. Le Fèvre, F. Bertran, N. Reyren, J.-M. George, and A. Fert, Phys. Rev. Lett. **116**, 096602 (2016).

[130] J. Könemann, R. J. Haug, D. K. Maude, V. I. Fal'ko, and B. L. Altshuler, Phys. Rev. Lett. **94**, 226404 (2005).

[131] C. P. Weber, J. Orenstein, B. A. Bernevig, S.-C. Zhang, J. Stephens, and D. D. Awschalom, Phys. Rev. Lett. **98**, 076604 (2007).

[132] Y. Feng, Q. Jiang, B. Feng, M. Yang, T. Xu, W. Liu, X. Yang, M. Arita, E. F. Schwier, K. Shimada, H. O. Jeschke, R. Thomale, Y. Shi, X. Wu, S. Xiao, S. Qiao, and S. He, Nature Communications **10**, 10.1038/s41467-019-12805-2 (2019).

[133] K. Hamamoto, M. Ezawa, K. W. Kim, T. Morimoto, and N. Nagaosa, Phys. Rev. B **95**, 224430 (2017).

[134] M. Michiardi, M. Bianchi, M. Dendzik, J. A. Miwa, M. Hoesch, T. K. Kim, P. Matzen, J. Mi, M. Bremholm, B. B. Iversen, and P. Hofmann, Phys. Rev. B **91**, 035445 (2015).

[135] H. Liu, E. Marcellina, A. R. Hamilton, and D. Culcer, Phys. Rev. Lett. **121**, 087701 (2018).

[136] H. Nakamura, T. Koga, and T. Kimura, Phys. Rev. Lett. **108**, 206601 (2012).

[137] P. D. C. King, S. McKeown Walker, A. Tamai, A. de la Torre, T. Eknapakul, P. Buaphet, S.-K. Mo, W. Meevasana, M. S. Bahramy, and F. Baumberger, Nature Communications **5**, 10.1038/ncomms4414 (2014).

[138] K. V. Shanavas, Phys. Rev. B **93**, 045108 (2016).

[139] H. Weyl, Zeitschrift für Physik **56**, 330 (1929).

[140] J. A. Krieger, S. Stolz, I. Robredo, K. Manna, E. C. McFarlane, M. Date, B. Pal, J. Yang, E. B. Guedes, J. H. Dil, *et al.*, Nature communications **15**, 3720 (2024).

[141] A. Veneri, D. T. S. Perkins, C. G. Péterfalvi, and A. Ferreira, Phys. Rev. B **106**, L081406 (2022).

[142] M. Sakano, M. Hirayama, T. Takahashi, S. Akebi, M. Nakayama, K. Kuroda, K. Taguchi, T. Yoshikawa, K. Miyamoto, T. Okuda, K. Ono, H. Kumigashira, T. Ideue, Y. Iwasa, N. Mitsuishi, K. Ishizaka, S. Shin, T. Miyake, S. Murakami, T. Sasagawa, and T. Kondo, Phys. Rev. Lett. **124**, 136404 (2020).

[143] G. Gatti, D. Gosálbez-Martínez, S. S. Tsirkin, M. Fanciulli, M. Puppin, S. Polishchuk, S. Moser, L. Testa, E. Martino, S. Roth, P. Bugnon, L. Moreschini, A. Bostwick, C. Jozwiak, E. Rotenberg, G. Di Santo, L. Petaccia, I. Vobornik, J. Fujii, J. Wong, D. Jariwala, H. A. Atwater, H. M. Rønnow, M. Chergui, O. V. Yazyev, M. Grioni, and A. Crepaldi, Phys. Rev. Lett. **125**, 216402 (2020).

[144] J. Schliemann and D. Loss, Phys. Rev. B **68**, 165311 (2003).

[145] X. Cartoixà, L.-W. Wang, D.-Y. Ting, and Y.-C. Chang, Phys. Rev. B **73**, 205341 (2006).

[146] M. Kohda, V. Lechner, Y. Kunihashi, T. Dollinger, P. Olbrich, C. Schönhuber, I. Caspers, V. V. Bel'kov, L. E. Golub, D. Weiss, K. Richter, J. Nitta, and S. D. Ganichev, Phys. Rev. B **86**, 081306 (2012).

[147] L. L. Tao and E. Y. Tsymbal, Nature Communications **9**, 10.1038/s41467-018-05137-0 (2018).

[148] H. Nakamura, T. Koga, and T. Kimura, Phys. Rev. Lett. **108**, 206601 (2012).

[149] H. J. Zhao, H. Nakamura, R. Arras, C. Paillard, P. Chen, J. Gosteau, X. Li, Y. Yang, and L. Bellaiche, Phys. Rev. Lett. **125**, 216405 (2020).

[150] O. V. Yazyev, J. E. Moore, and S. G. Louie, Phys. Rev. Lett. **105**, 266806 (2010).

[151] S. Leiva-Montecinos, J. Henk, I. Mertig, and A. Johansson, Phys. Rev. Res. **5**, 043294 (2023).

[152] B. A. Bernevig and T. L. Hughes, *Topological insulators and topological superconductors* (Princeton university press, 2013).

[153] P. B. Pal, *An introductory course of Statistical Mechanics* (Alpha Science International, 2008).

[154] Y. Gao, S. A. Yang, and Q. Niu, Phys. Rev. B **91**, 214405 (2015).

[155] A. Bandyopadhyay, N. B. Joseph, and A. Narayan, Materials Today Electronics **8**, 100101 (2024).

[156] I. Sodemann and L. Fu, Phys. Rev. Lett. **115**, 216806 (2015).

[157] O. Pal and T. K. Ghosh, Phys. Rev. B **109**, 035202 (2024).

[158] S. D. Ganichev and L. E. Golub, physica status solidi (b) **251**, 1801 (2014), https://onlinelibrary.wiley.com/doi/pdf/10.1002/pssb.201350261 .

[159] J. Su, X. Wang, C. Shao, Y. Guo, and L. Xian, Materials & Design **209**, 110005 (2021).

[160] W. Liu, F. Meng, J. Cheng, and W. Min, Physics Letters A **458**, 128588 (2023).

[161] T. Koga, J. Nitta, T. Akazaki, and H. Takayanagi, Phys. Rev. Lett. **89**, 046801 (2002).

[162] J. D. Koralek, C. P. Weber, J. Orenstein, B. A. Bernevig, S.-C. Zhang, S. Mack, and D. D. Awschalom, Nature **458**, 610 (2009).

[163] M. Walser, C. Reichl, W. Wegscheider, and G. Salis, Nature Physics **8**, 757 (2012).

[164] I. Sodemann and L. Fu, Phys. Rev. Lett. **115**, 216806 (2015).

[165] Q. Ma, S.-Y. Xu, H. Shen, D. MacNeill, V. Fatemi, T.-R. Chang, A. M. Mier Valdivia, S. Wu, Z. Du, C.-H. Hsu, *et al.*, Nature **565**, 337 (2019).

[166] J. Kang, J. Zou, K. Li, S.-L. Yu, and L.-B. Shao, Scientific Reports **9**, 2824 (2019).

[167] G. Sala, M. T. Mercaldo, K. Domi, S. Gariglio, M. Cuoco, C. Ortix, and A. D. Caviglia, Science **389**, 822 (2025).

[168] Y. Gao, S. A. Yang, and Q. Niu, Phys. Rev. Lett. **112**, 166601 (2014).

[169] B. A. Bernevig, J. Orenstein, and S.-C. Zhang, Phys. Rev. Lett. **97**, 236601 (2006).

[170] R. Winkler, *Spin–Orbit Coupling Effects in Two-Dimensional Electron and Hole Systems* (Springer, 2003).

[171] N. Nagaosa, J. Sinova, S. Onoda, A. H. MacDonald, and N. P. Ong, Rev. Mod. Phys. **82**, 1539 (2010).

[172] J. E. Moore and J. Orenstein, Phys. Rev. Lett. **105**, 026805 (2010).

[173] T. Morimoto, S. Zhong, J. Orenstein, and J. E. Moore, Phys. Rev. B **94**, 245121 (2016).

[174] P. Törmä, Phys. Rev. Lett. **131**, 240001 (2023).

[175] C. Zeng, S. Nandy, A. Taraphder, and S. Tewari, Phys. Rev. B **100**, 245102 (2019).

[176] D. C. Brody and L. P. Hughston, Journal of Geometry and Physics **38**, 19 (2001).

[177] F. D. M. Haldane, Phys. Rev. Lett. **93**, 206602 (2004).

[178] Z.-Y. Cao, A.-Q. Wang, X.-Y. Liu, T.-Y. Zhao, D. Yu, and Z.-M. Liao, Phys. Rev. B **111**, 125407 (2025).

[179] M. Huang, Z. Wu, J. Hu, X. Cai, E. Li, L. An, X. Feng, Z. Ye, N. Lin, K. T. Law, and N. Wang, National Science Review **10**, nwac232 (2022), https://academic.oup.com/nsr/article-pdf/10/4/nwac232/50268204/nwac232.pdf .

[180] S. Korrapati, S. Nandy, and S. Tewari, Phys. Rev. B **110**, 195119 (2024).

[181] H. Liu, J. Zhao, Y.-X. Huang, W. Wu, X.-L. Sheng, C. Xiao, and S. A. Yang, Phys. Rev. Lett. **127**, 277202 (2021).

[182] C. Wang, Y. Gao, and D. Xiao, Phys. Rev. Lett. **127**, 277201 (2021).

[183] S. M. Young and C. L. Kane, Phys. Rev. Lett. **115**, 126803 (2015).

[184] S. Borisenko, Q. Gibson, D. Evtushinsky, V. Zabolotnyy, B. Büchner, and R. J. Cava, Phys. Rev. Lett. **113**, 027603 (2014).

[185] L. Liu, C.-M. Miao, Q.-F. Sun, and Y.-T. Zhang, Phys. Rev. B **110**, 245413 (2024).

[186] D. Swain, A. Dey, A. Roy, K. Saha, and S. D. Das, Phys. Rev. B **111**, 035143 (2025).

[187] A. A. Soluyanov, D. Gresch, Z. Wang, Q. Wu, M. Troyer, X. Dai, and B. A. Bernevig, Nature **527**, 495 (2015).

[188] L. Lu, Z. Wang, D. Ye, L. Ran, L. Fu, J. D. Joannopoulos, and M. Soljačić, Science **349**, 622 (2015), https://www.science.org/doi/pdf/10.1126/science.aaa9273 .

[189] X. Wan, A. M. Turner, A. Vishwanath, and S. Y. Savrasov, Phys. Rev. B **83**, 205101 (2011).

[190] Q. Lu, P. S. Reddy, H. Jeon, A. R. Mazza, M. Brahlek, W. Wu, S. A. Yang, J. Cook, C. Conner, X. Zhang, *et al.*, Nature communications **15**, 6001 (2024).

[191] S. Roy and A. Narayan, Journal of Physics: Condensed Matter **34**, 385301 (2022).

[192] C. Fang, Y. Chen, H.-Y. Kee, and L. Fu, Phys. Rev. B **92**, 081201 (2015).

[193] S. Xue, M. Wang, Y. Li, S. Zhang, X. Jia, J. Zhou, Y. Shi, X. Zhu, Y. Yao, and J. Guo, Phys. Rev. Lett. **127**, 186802 (2021).

[194] P.-Y. Chang, Materials Today Quantum **8**, 100057 (2025).

[195] X. Hu, Europhysics Letters **149**, 56001 (2025).

[196] M.-J. Gao and J.-H. An, Phys. Rev. B **108**, L241402 (2023).

[197] L. Jin, X. Zhang, Y. Liu, X. Dai, X. Shen, L. Wang, and G. Liu, Phys. Rev. B **102**, 125118 (2020).

[198] V. Pandey, D. Joy, D. Culcer, and P. Bhalla, Phys. Rev. B **110**, 155108 (2024).

[199] V. Pandey and P. Bhalla, physica status solidi (RRL)–Rapid Research Letters , 2500108 (2025).

[200] N. P. Armitage, E. J. Mele, and A. Vishwanath, Rev. Mod. Phys. **90**, 015001 (2018).

[201] C.-K. Chiu, J. C. Y. Teo, A. P. Schnyder, and S. Ryu, Rev. Mod. Phys. **88**, 035005 (2016).

[202] S.-Y. Yang, H. Yang, E. Derunova, S. S. Parkin, B. Yan, and M. N. Ali, Advances in Physics: X **3**, 1414631 (2018).

[203] J. Li, H. Wang, and H. Pan, Phys. Rev. B **104**, 235136 (2021).

[204] G. Xu, H. Weng, Z. Wang, X. Dai, and Z. Fang, Phys. Rev. Lett. **107**, 186806 (2011).

[205] G. Chang, S.-Y. Xu, H. Zheng, B. Singh, C.-H. Hsu, G. Bian, N. Alidoust, I. Belopolski, D. S. Sanchez, S. Zhang, *et al.*, Scientific reports **6**, 38839 (2016).

[206] J. Noky, Q. Xu, C. Felser, and Y. Sun, Phys. Rev. B **99**, 165117 (2019).

[207] M. Ezawa, Scientific reports **9**, 5286 (2019).

[208] H. Chen, S. Zhang, W. Jiang, C. Zhang, H. Guo, Z. Liu, Z. Wang, F. Liu, and X. Niu, Journal of Materials Chemistry A **6**, 11252 (2018).

[209] J.-L. Lu, W. Luo, X.-Y. Li, S.-Q. Yang, J.-X. Cao, X.-G. Gong, and H.-J. Xiang, Chinese Physics Letters **34**, 057302 (2017).

[210] Y. Shao, Z. Sun, Y. Wang, C. Xu, R. Sankar, A. J. Breindel, C. Cao, M. M. Fogler, A. J. Millis, F. Chou, Z. Li, T. Timusk, M. B. Maple, and D. N. Basov, Proceedings of the National Academy of Sciences **116**, 1168 (2019), https://www.pnas.org/doi/pdf/10.1073/pnas.1809631115 .

[211] C. H. Lee, H. H. Yap, T. Tai, G. Xu, X. Zhang, and J. Gong, Phys. Rev. B **102**, 035138 (2020).

[212] J. Jeon, T. Kim, J. Jang, H. Kim, M. Ozerov, J. S. Kim, H. Min, and E. Choi, Phys. Rev. Lett. **135**, 086901 (2025).

[213] X. Huang, L. Zhao, Y. Long, P. Wang, D. Chen, Z. Yang, H. Liang, M. Xue, H. Weng, Z. Fang, X. Dai, and G. Chen, Phys. Rev. X **5**, 031023 (2015).

[214] F. Balduini, A. Molinari, L. Rocchino, V. Hasse, C. Felser, M. Sousa, C. Zota, H. Schmid, A. G. Grushin, and B. Gotsmann, Nature Communications **15**, 6526 (2024).

[215] P.-Y. Chang, Nodal-line semimetals and their variance (2025), arXiv:2507.02329 [cond-mat.str-el] .

[216] Y.-J. Jin, R. Wang, J.-Z. Zhao, Y.-P. Du, C.-D. Zheng, L.-Y. Gan, J.-F. Liu, H. Xu, and S. Y. Tong, Nanoscale **9**, 13112 (2017).

[217] S. Barati, H. Rahimpoor, and S. H. Abedinpour, Phys. Rev. B **111**, 075125 (2025).

[218] H. Rahimpoor and S. H. Abedinpour, Phys. Rev. B **109**, 045120 (2024).

[219] V. Pandey, D. Joy, D. Culcer, and P. Bhalla, Phys. Rev. B **110**, 155108 (2024).

[220] V. Pardo and W. E. Pickett, Phys. Rev. Lett. **102**, 166803 (2009).

[221] C. Zhong, Y. Chen, Y. Xie, Y.-Y. Sun, and S. Zhang, Phys. Chem. Chem. Phys. **19**, 3820 (2017).

[222] X. Li, J. Sun, P. Shahi, M. Gao, A. H. MacDonald, Y. Uwatoko, T. Xiang, J. B. Goodenough, J. Cheng, and J. Zhou, Proceedings of the National Academy of Sciences **115**, 9935 (2018).

[223] H. Peelaers and C. G. Van de Walle, Phys. Rev. B **86**, 241401(R) (2012).

[224] A. Bandyopadhyay, N. B. Joseph, and A. Narayan, Materials Today Electronics **6**, 100076 (2023).

[225] K. Das, S. Lahiri, R. B. Atencia, D. Culcer, and A. Agarwal, Phys. Rev. B **108**, L201405 (2023).

[226] H. Li, C. Zhang, C. Zhou, C. Ma, X. Lei, Z. Jin, H. He, B. Li, K. T. Law, and J. Wang, Nature Communications **15**, 7779 (2024).

[227] H. Yu, X. Li, Y.-Q. Bie, L. Yan, L. Zhou, P. Yu, and G. Yang, Nature Communications **16**, 7698 (2025).

[228] X.-Y. Liu, A.-Q. Wang, D. Li, T.-Y. Zhao, X. Liao, and Z.-M. Liao, Phys. Rev. Lett. **134**, 026305 (2025).

[229] C. K. Barman, A. Chattopadhyay, S. Sarkar, J.-X. Zhu, and S. Nandy, Phys. Rev. B **111**, 235113 (2025).

[230] S. S. Samal, S. Nandy, and K. Saha, Phys. Rev. B **103**, L201202 (2021).

[231] A. V. Shumilin and V. V. Kabanov, Phys. Rev. Res. **5**, 033215 (2023).

[232] C. Cheng, Z. Yan, Y. Xing, J. Dong, Y. Zhang, C. Wan, G. Yu, Z. Xia, L. Li, and X. Han, Applied Physics Letters **122** (2023).

[233] A. Marmodoro, O. c. v. Šipr, I. Turek, A. Johansson, S. Mankovsky, and H. Ebert, Phys. Rev. B **113**, 075148 (2026).